2015

Development and applications of single particle orientation and rotational tracking in dynamic systems

Kuangcai Chen
Iowa State University

Development and applications of single particle orientation and rotational tracking in dynamic systems

by

Kuangcai Chen

A dissertation submitted to the graduate faculty

in partial fulfillment of the requirements for the degree of

DOCTOR OF PHILOSOPHY

Major: Analytical Chemistry

Program of Study Committee:
Javier Vela, Major Professor
Robert S. Houk
Emily Smith
Wenyu Huang
Sanjeevi Sivasankar

Iowa State University

Ames, Iowa

2015

To my family and friends

To my mentor, Professor Ning Fang

TABLE OF CONTENTS

ACKNOWLEDGMENTS

I would like to thank my committee chair, Dr. Javier Vela, and my program of study committee members, Dr. Robert S. Houk, Dr. Emily Smith, Dr. Wenyu Huang, and Dr. Sanjeevi Sivasankar, for their guidance and advice on my research and for accommodating their schedules for all the meetings throughout the years at Iowa State University. I really appreciate Dr. Vela's kindness for taking me into his group and temporarily serving as my major advisor for the last several months. I also want to thank the nice working environment provided by Dr. Vela's group during my dissertation writing.

I also want to thank Dr. Ning Fang, my former major advisor, for serving as my major advisor during my entire graduate research, without whom, this dissertation would not have been possible. I really enjoyed the days pursuing knowledge under his guidance. It was my fortune to have such an amazing advisor.

I'm grateful for all the supports that chemistry department offered. I want to thank Dr. Curtis Mosher for allowing me to use the Roy J. Carver Laboratory facility these years.

I appreciate the opportunities to collaborate with Dr. Vela's former student, Dr. Chia-Cheng Lin and Dr. Tian Xia's former student, Xinxin Fan on the research projects.

In addition, I would also like to thank my friends, the department faculties and staffs for making my time at Iowa State University a memorable experience. I want to thank all

former group members, Dr. Anthony Stender, Dr. Yan Gu, Dr. Kyle Marchuk, Dr. Rui Han, Dr. Ji Won Ha, Dr. Ashley Augspurger, Bin Dong, Amanda Nguy, and Fei Zhao, former Postdoc, Dr. Shaobin Zhu, former visiting students, Xinxin Fan, Tian Tian, Jiaheng Yin, and Ling Ma.

In the end, I want to thank my family. They always make me feel beloved no matter where I am. They are always being supportive no matter what path I choose in my life. They are always being there for me.

The work in this dissertation was supported by the Ames Laboratory, U.S. Department of Energy. Ames Laboratory is operated by Iowa State University under contract number DE-AC02- 07CH11358. The document number assigned to this thesis/dissertation is IS-T 3147.

CHAPTER 1

GENERAL INTRODUCTION

Dissertation Organization

This dissertation is comprised of five chapters. Chapter 1 (this chapter) is the general introduction of the dissertation. It includes the overview of the dissertation's structure and its organization. It also gives an introduction to single particle tracking (SPT), SPT probes, and their applications in optical imaging studies. Several optical microscopic techniques developed for single particle orientation and rotational tracking (SPORT), together with their basic light microscopy working principles, are briefly introduced. The development and applications of differential interference contrast (DIC) microscopy and DIC-based SPORT techniques are also discussed. Chapter 2 is modified from a manuscript published in *Analytical Chemistry*, reporting the synthesis of multishell Au/Ag/SiO_2 nanorods and their application of these optically tunable probes in DIC based SPORT studies. The addition of a silver shell provides improved sensitivity and silica coating provides enhanced stability and biocompatibility. This new rotational probe is a promising imaging probe for single plasmonic particle tracking experiments in biological systems. Chapter 3 introduces a novel five-dimensional SPT (5D-SPT) technique based on the subtle modification of the standard DIC microscope with the addition of a wedge prism. The modification produces parallax-DIC patterns while an objective scanner enables the auto-focusing capability. With the implementation of an automatic feedback loop algorithm in the tracking program, the nanoparticles of interest are kept in focus to provide the highest possible S/N for 2D localization and orientation determination, while their *z* positions are recorded from the vertical movement of a high-precision objective scanner. This 5D-SPT technique is used to

study endocytosis and intracellular transport of different cargo in live cell environment. Chapter 4 demonstrates the application of autocorrelation function analysis on the interpretation of gold nanorod rotational dynamics. This study investigates the rotations of surface modified gold nanorods on synthetic lipid bilayers. This chapter provides details on how experimental parameters, such as trajectory length of the SPT tracking and frame rate (exposure time), affect the extraction of rotational correlation information with the aid of computer simulations. This work presents efforts on data analysis and experiment design in the field of rotational dynamics studies.

Introduction to Single Particle Tracking

Single particle tracking

SPT is of great importance in the study of chemical and biological dynamic systems, aided by the advance of light microscope techniques[1,2] and the development of particle tracking methods.[3-6] The term 'particle' can be a single molecule, a quantum dot, a nanoparticle, a macromolecular complex, an organelle, a virus or a microsphere.[6] SPT experiments record the motions of individual particles in a time series and extract a wealth of information on individual dynamics that is cancelled out in ensemble experiments by image analysis. Many efforts have been devoted to SPT image analysis.[4,7-9] Image processing usually involves three steps.[6,10] The first step is the detection or localization of the particles. Base on some certain set criteria and signal-to-noise (S/N) ratio, an image of particles at a given time is processed to distinguish the particles from the background. The particles' spatial positions are localized in this step. Repeating this process for every image of the sequence provides the localization information of the particles as a function of time. The second step involves the linking of particles throughout all the frames in a series of images.

The particle positions in the time series are linked frame by frame into trajectories. Numerous methods have been developed for diverse experimental needs.[9] Due to the large diversity in SPT research, there is no universal best particle tracking method for all SPT experiments. Details on different methods and their comparison can be found in many publications.[10-14] The last step is the interpretation of trajectories. After the trajectories are obtained, the mean-square displacement can be extracted and fitted into standard motions, such as random walk, directed motion, confined motion, or immobile. This provides further information of the particle's motions and its interactions with the surroundings. This method provides insight knowledge of different biological processes, which cannot be obtained by ensemble experiments. Because of its advantages, SPT has been used in a wide range of biological fields, such as the study of membrane dynamics,[15,16] intracellular transport,[17,18] cellular uptakes.[19,20]

Two-dimensional (2D) SPT techniques are well established because the lateral positions of probes can be easily detected from the recorded images with high precision and accuracy. In contrast, three-dimensional (3D) SPT techniques are more challenging, as they usually require more sophisticated microscope designs. Recently, Deschout *et al.* reviewed eight different groups of microscope designs for unambiguous 3D SPT localization with various precisions.[21] These methods are based on the multiple image-detection of the same probe at different image planes or the manipulation of a 3D point spread function (PSF) profile. Erdal Toprak *et al.* introduced a bifocal imaging method for 3D SPT of both fluorescent and nonfluorescent probes.[22] In this study, lateral position (x,y) was localized in a focused image and axial z position was determined from a defocused image simultaneously using a single CCD camera. This 3D SPT technique was further applied to *in vitro* bead

tracking and *in vivo* 3D organelle and bead tracking with 2-5 nm accuracy. One should note that increasing the image planes extends the axial localization range but sacrifices the localization precision.

By inserting a cylindrical lens in the microscope light path, the axial positions of probes can be encoded into 2D images.[23,24] This PSF engineering method introduces astigmatism that produces elliptically shaped images. The ellipticity and orientation of PSF depend on the axial z position of the probe. The axial positions of tracking probes can be calculated by calibrating the 2D image shapes with certain axial distance. PSF can also be manipulated by introducing a phase ramp over one-half of the detection light path with a wedge prism.[25,26] In this technique, known as parallax, the axial localization is determined by the separation distance of the two split images. The application of this technique is further discussed in chapter 3 on 5D-SPT studies. Parallax imaging can also be implemented by a set of mirrors.[27] In other works, spatial light modulator or manufactured phase plate were used to generate more complex PSFs such as single helix (corkscrew),[28] double helix,[29,30] and tetrapod[31] for 3D SPT applications.

SPT probes

Fluorescent optical probes and nonfluorescent nanoparticle probes are the two main categories of SPT probes. Biological fluorophores, organic dyes, and nanocrystals, such as semiconductor quantum dots (QDs) are the three main classes of fluorescent probes. Fluorophores obtained from natural products were first utilized as optical probes in biological studies. More stable fluorophores fuorescein isothiocyanate (FITC) and its many derivatives were later used in a broad range of fluorescence microscopy experiments.[32] The discovery of

green fluorescent protein (GFP) and its variants allows labelling a whole cell or organism by expressing a fluorescent tag of interest, which greatly increases the specificity of labelling techniques. Roger Y. Tsien, Martin Chalfie, and Osamu Shimomura were awarded the Noble Prize in Chemistry in 2008 for the discovery and development of the GFP. The use of photoswitchable dyes lead to the development of three superresolution fluorescence imaging techniques: Stochastic optical reconstruction microscopy (STORM),[24,33] photoactivated localization microscopy (PALM),[34] and fluorescence photo-activation localization microscopy (fPALM).[35] Fluorophores were usually switched on and off sequentially and their positions were localized with nanometer accuracy in each image cycle. With the help of these photoswitchable fluorescence probes, far-field fluorescence microscopy techniques break the diffraction limit of light, which otherwise restricts the spatial resolution of wide-field optical microscopy techniques. The 2014 Chemistry Nobel Prize was awarded jointly to Eric Betzig, Stefan W. Hell and William E. Moerner for the development of super-resolved fluorescence microscopy. New fluorescence probes are still being discovered and developed for light microscopy applications.[36] Traditional organic dyes that are small in size, with relatively large photon emission and the possibility of live cell labelling provide the ability to target specific biological structures. QDs are brighter and more photostable fluorescent probes than conventional organic dyes;[37,38] however, QDs suffer from cytotoxicity, self-aggregation and blinking.[39-41] The synthesis and SPT applications of non-blinking QDs are reported elsewhere.[42,43] Although photobleaching is a disadvantage of fluorescent probes, it was exploited in other techniques, such as fluorescence recovery after photobleaching (FRAP) and fluorescence loss in photobleaching (FLIP), for example to study the diffusion of molecules.[44,45] Oxygen scavenging systems were usually used in single-molecule

fluorescence experiments to improve dye stability by removing O_2 species.[46] In addition, the blinking of QDs was exploited to allow superresolution imaging.[47]

Nonfluorescent nanoparticle probes have become an increasingly popular alternative to traditional fluorescent probes in biological SPT applications because most nonfluorescent nanoparticle probes display excellent photostability, ease of synthesis and unique optical properties.[48-50] Generally speaking, nonfluorescent nanoparticles include single component nanoparticles, hybrid nanoparticles, metallic alloys, silica, *etc*. Good photostability allows these nanoparticles to be dynamically tracked for indefinitely long periods without suffering photobleaching or blinking. Their large cross-sections allow them to be localized with high temporal and spatial resolution.[49-51] Nonfluorescent probes are usually relatively nontoxic compared to most QDs. Noble metal nanoparticles, especially gold and silver, have gained much attention due to their localized surface plasmon resonance (SPR) and related properties,[52] and are thus highly popular for nonfluorescent imaging techniques. Great success has been achieved for gold nanocrystal synthesis with wet chemistry methods. Various methods have been successfully developed to synthesize gold nanoparticles in a great variety of shapes and structures, such as spheres, rods, stars, and nanowires.[53-55] Among these shapes, gold nanorods (AuNRs) are the most widely studied.[52,56] The presence of longitudinal SPR and transverse SPR in AuNRs give rise to the anisotropic absorption and scattering properties of AuNRs, which makes AuNRs ideal orientation probes for SPORT applications.[57-59] Hybrid nanoparticles can be made of multiple components to enable the multi-wavelength or multi-mode detection.[60] Various types of hybrid nanoparticles have been synthesized with different optical properties.[61] Most of them have not been used in SPT or

live cell imaging except in a few cases.[62-64] In chapter 2, an attempt of using multishell Au/Ag/SiO2 core-shell hybrid nanorods for DIC-based SPORT techniques is presented.

Introduction to SPORT Techniques

While the conventional SPT techniques focus on translational movement of optical probes, SPORT research targets the rotational behavior of the imaging probes as well as their spatial movement. Compared to well-established translational tracking, resolving the orientation of optical probes in real time is more challenging. On the other hand, orientation and rotational information are crucial to understand many biological processes, such as self-rotation of ATP synthase,[65] the stepping of molecular motors[66,67] and DNA polymerization.[68] Recent developments in optical imaging techniques have greatly expanded our ability to overcome the challenges associated with obtaining the translational dynamics as well as the rotational dynamics of optical probes. The Fang group originally used the acronym SPORT to describe a platform based on DIC microscopy for tracking the rotational dynamics of plasmonic gold nanorods in live cells.[59,69] SPORT includes all imaging techniques in an effort to design and determine the orientation and rotational motions of any optical imaging probe.[49,70] A short introduction to different SPORT techniques including some basic optical microscopy concepts and the working principles of these techniques are presented below. The use of fluorescent probes is discussed in the **Fluorescence-based SPORT Techniques** section. Discussion of SPORT techniques in all other sections is mainly focused on AuNRs, as these are some of the most widely and frequently used nonfluorescent rotational probes. Other techniques such as Raman spectroscopy and non-linear optical microscopy methods

were also used for orientation and rotational applications,[71,72] but they are not included in this dissertation.

Fluorescence-based SPORT techniques

Fluorescence microscopy is one of the most widely used techniques for SPT and single molecule detection. Epi-fluorescence microscopy, as shown in **Figure 1**, is the simplest design among wide-field fluorescence microscopy imaging techniques. The excitation light, after passing through a proper excitation filter, illuminates all individual fluorophores in a relatively large area simultaneously. The illumination light passes through the whole depth of the sample, and the fluorescence emitted by the sample is collected by the microscope objective onto a complementary metal–oxide–semiconductor (COMS) or charge-coupled device (CCD) camera. This allows simultaneous detection of all fluorescence probes in the field of view. However, this technique yields poor image resolution and contrast compared to other sophisticated fluorescence microscopy techniques.

Total internal reflection fluorescence (TIRF) microscopy, another commonly used wide-field fluorescence microscopy imaging technique, was developed by Daniel Axelrod in early 1980s.[73] There are two common TIRF microscope configurations, prism-based and objective-based.[74] Both configurations are used for different kinds of specimens and applications. **Figure 2** shows the schematic diagram of the prism-based TIRF microscopy. Prism-based TIRF has advantages over objective-based TIRF due to its lower cost and ease of controlling the incident light angle. Fundamentally, both configurations obey the same principle. When excitation light illuminates the interface between two media, coming from a higher refractive index medium (η_1) to a lower refractive index medium (η_2), at an incident angle larger than the critical angle, the incident light undergoes total internal reflection (TIR)

in the high refractive index medium. An evanescent field (EF) is generated and its intensity decreases exponentially along the z-axis into the low refractive index side. This EF depth depends on the excitation light wavelength, the incident angle, and the refractive indices (η_1 and η_2). EF depth can extend up to a few hundred nanometers from the interface and allows the excitation of fluorescence probes at the interface. Fluorescence probes beyond the EF depth do not produce fluorescent photons, which translates into lower interference from other regions. TIRF microscopy has been extensively used in single-molecule detection of membrane-associated processes (cell receptors, cell-substrate interactions, exocytosis or endocytosis).[75]

Fluorescence-based SPORT techniques utilize the fluorescence microscopy configuration to detect the transition dipole orientation of the fluorescence probes in different polarization channels.[76-80] Fluorescence polarization anisotropy or polarization-dependent absorption measurements were used to resolve the dipole orientation of the fluorescence probes. **Figure 3** shows a general schematic diagram of fluorescence polarization microscopy. A polarizing beam splitter is usually used to split the emitted fluorescence into two orthogonal polarization directions. Signals obtained in these two channels are used to calculate fluorescence anisotropy and relative fluorescence intensity in order to determine the orientation of the probes and their rotational dynamics.

Various applications of fluorescence-based SPORT techniques have been reported in the literature.[76,79] Joseph Forkey *et al.* reported the use of a single molecule fluorescence polarization technique in determining the orientation of Calmodulin (a calcium-modulated protein) on the light chain domain of myosin V in 3D with 20–40 ms temporal resolution.[76] Bisiodoacetamidorhodamine, a divalently reactive fluorophore, was used to label Calmodulin

at a known orientation. TIRF microscopy was used to image the actin and rhodamine-labelled myosin V at two wavelengths with four different polarization states switched (time-multiplexed). Their data confirmed the hand-over-hand model of individual double-headed myosin V moving along actin filaments, and provided evidence for lever arm hypothesis based on the calmodulin-binding domain rotation. Another work done by Toprak *et al.* used QDs as orientation probes to investigate the same biological system.[79] They combined defocused orientation and position imaging (DOPI) techniques and fluorescence imaging with one-nanometer accuracy (FIONA)[5] to observe the lever arm rotational dynamic and translocation of myosin V using TIRF microscope. In this work, focused images were used to localize QD-labelled myosin V with 1.5 nm accuracy by FIONA for tracking the translocation, and out-of-focused images (about 500 nm away from best focus position) were used to detect the orientation of the probes through a pattern-match analysis technique. The stepping behavior of the myosin V and the rotational dynamics of the lever arm were determined in detail.

The limitations of the fluorescence-based SPORT techniques arise from the intrinsic photobleaching and/or blinking properties of the fluorescent probes. High autofluorescence background in cellular environment also limits applications to many biological problems. Defocused images give low signal-to-noise ratios. Pattern matching technique can be arbitrary and time-consuming. The technique requires switching between focused imaging and defocused imaging which can be an inconvenience.

Scattering-based SPORT techniques

Bright field (BF) and dark field (DF) microscopy are the two simplest optical microscopy designs with their own sets of advantages and limitations. In BF microscopy, transmitted light illuminates the light-absorbing sample and the sample is seen as a dark spot on the bright background. This simplicity made BF microscopy a popular technique in the early years of light microscopy history. On the other hand, its limitations include very low contrast for most biological samples and non-light absorbing samples, and low optical resolution. In DF microscopy, the image contrast is enhanced due to the collection of only Rayleigh scattering light from the sample that is spatially separated from the illumination light. This produces images of bright samples on a dark background. The numerical aperture (NA) of the objective used in DF microscopy is smaller than that of the condenser. A light stop in the DF condenser is used to block the zeroth order illumination light from entering the objective. Despite being one of the oldest light microscopy techniques, DF microscopy was revitalized with new fast-growing nanotechnologies. DF microscopy was reported to be able to detect 5 nm particles under optimum conditions. It became a very useful SPT tool with nanometer spatial precision and microsecond temporal resolution. The technique, however, has its own limitations, such as the possibility of sample damage due to strong light illumination, and scattering interference from cellular components.[81]

DF microscopy is the first light microscopy technique used in the orientation study of nonfluorescent probes. The configuration of DF microscopy used for SPORT applications is illustrated in **Figure 4**. Sönnichsen *et al.* demonstrated that nonfluorescent rotational tracking probes, in this case AuNRs (25 nm × 60 nm), can be used to observe the 2D rotational diffusion when the probes are attached to a glass surface.[82] A birefringent crystal

was used to split the scattered light into two orthogonal polarization directions for each AuNR. Each AuNR formed two spots in the detector and the intensities for the two spots were recorded simultaneously. Under the assumption of homogeneous illumination, the scattering intensity of a AuNRs in a particular polarization direction is proportional to $(\cos(\theta))^2$, where θ is the angle between the AuNR and the polarization direction. Thus, the orientation of the AuNR can be resolved. Also the autocorrelation of the intensity traces was used to estimate the rotational diffusion time. Their results indicated that the rotational motion of the AuNRs was dominated by the particle-surface interactions. This method allowed 2D rotational tracking but was incapable of 3D orientation determinations.

A defocused DF imaging technique was successfully used by Lehui Xiao *et al.* to determine the 3D orientation of AuNRs through deconvolution of the field distribution pattern in defocused DF images.[83] Their technique can resolve the orientation of AuNRs in 3D space without degeneracy. One should note that the aspect ratio of AuNR, the NA of the objective, the defocusing distance, and the polarization direction of the incident radiation will all affect the resulted images. Observed images are interpreted by comparing them with a series of simulated images with different parameters.

Beside DF scattering methods, total internal reflection scattering (TIRS) methods were developed for the determination of the full 360 degree orientation of AuNRs.[84,85] TIRS has the same configuration as TIRF. In TIRS, instead of collecting the emitted fluorescence, scattered light is recorded by the detector. Jiwon Ha *et al.* reported a TIRS method called focused orientation and position imaging (FOPI). [84] FOPI utilizes the coupling between AuNRs and a 50 nm thick gold film under a p-polarized laser to determine the orientation of AuNRs in a single frame without angular degeneracy in full 360 degrees. The coupling

changes the AuNR scattering PSF from circularly symmetric shape into donut-shapes, and forms characteristic image patterns when the AuNRs rotate in different angles.

Another interesting work used resonance light scattering correlation spectroscopy (RLSCS) technique for rapid characterization of rotational and translational diffusion of GNPs and GNRs, which is also related to scattering,[86] It will be further discussed in the **Correlation Spectroscopy-base SPORT Techniques** section.

Any objects in the field of view can give scattering, thus, noise and interference often occur. For instance, the interference from other cellular components gives strong background scattering and greatly affects the detection of probes of interest in live cells. The presence of other larger objects or the aggregation of the probes can make the scattering signal predominant. Defocused DF imaging techniques suffer the same issues as mentioned in fluorescence-based SPORT technique discussion above.

Absorption-based SPORT techniques

Photothermal imaging technique is an optical microscopy method developed by David Boyer, based on the detection of nonfluorescent probe absorption.[87] In this work, the nonfluorescent probes were heated by a frequency-modulated absorption beam and the local heating caused a change in refractive index of the medium. This change in refractive index was determined by another probe beam. The signal was shown to depend on the nanoparticle size and the heating laser power. Photothermal imaging technique has been used in cancer therapy applications.[88] Wei-Shun Chang *et al.* applied the polarization-sensitive photothermal imaging technique to the observation of the 2D orientation of AuNRs.[57] Determination of the individual AuNR oritentation was based on the polarization anisotropy

of the transverse and longitudinal surface plasmonic absorptions. Quantitative orientation information of the AuNRs was obtained by fitting the photothermal polarization traces to an equation, thus allowing the accurate determination of individual AuNR orientation on a glass slide. A disadvantage of the absorption-based photothermal imaging technique is the possibility of biological sample damage due to the use of a high power laser.

Correlation spectroscopy-based SPORT techniques

The groups of Stephan Link and Jicun Ren independently adopted correlation spectroscopy methods for characterizing the rotational and translational dynamics of AuNRs based on the theory of fluorescence correlation spectroscopy (FCS).[86,89] **Figure 5** shows the schematic diagram of a typical FCS setup. FCS works on the principle of correlation analysis of fluorescence intensity fluctuation. In FCS, the sample is illuminated by the excitation laser beam through a microscope objective. The laser beam is directed by a dichroric mirror into the microscope objective. It is necessary to use a highly diluted sample (nM to pM) so that only a few objects of interest diffuse in and out of the focal volume. The signal fluctuation can be recorded by a detector, and the time-dependent intensity traces can be interpreted to obtain quantitative information, including diffusion coefficients, hydrodynamic radii, average concentrations, kinetic chemical reaction rates, singlet-triplet dynamics, *etc*. The interpretation process can also be done using an auto-correlator.

The group of Stephan Link reported the use of one-photon luminescence correlation spectroscopy in measuring the hydrodynamic sizes and investigating the rotational and translational dynamics of AuNRs.[89] Circularly polarized, 514 nm and 633 nm lasers were used to excite the transverse and longitudinal plasmon resonances of the AuNRs. The

interplay between hot electron-hole pairs and surface plasmons was observed, revealing that luminescence occurs via emission by a surface plasmon. One-photon luminescence correlation spectroscopy measurements were also confirmed to be less sensitive to the presence of larger nanoparticles or aggregates compared to scattering correlation spectroscopy measurements.

Jicun Ren group applied resonance light scattering correlation spectroscopy (RLSCS) in characterizing rapid rotational and translational diffusion of GNPs and AuNRs in solution.[86] Wavelength dependent resonance light scattering fluctuations were measured analogously to fluorescence fluctuations in FCS in order to obtain the translational and rotational diffusion coefficients and aspect ratios of AuNRs. Compared to the FCS setup, the emission filter was removed in the RLSCS setup. It is worth noting that a high NA objective was used to reduce the rotational component. By monitoring the change of the translational time, detection of DNA hybridization and the homogeneous immunoassay were demonstrated.

DIC-based SPORT techniques

DIC microscopy was initially introduced by Nomarski in the 1950s. Compared to BF, DF, and phase contrast microscopy, DIC provides higher contrast, better resolution, and shallow depth of field images on cellular visualization without sample staining. Thus, DIC microscopy has been used as complementary technique to other fluorescence-based techniques in biological imaging. Various DIC configurations were developed based on the difference in coherence of the illumination, such as Nomarski-DIC, Köhler-DIC, and Plas-DIC configurations.[90] The Nomarski-DIC microscope uses full objective and condenser

apertures for higher lateral resolution and better depth discrimination. This makes Nomarski-DIC configuration one of the most popular DIC image formation models. DIC work done in this dissertation was performed with a Nikon Eclipse i80, which adopts the Nomarski DIC configuration for image formation. Thus, the DIC microscopy in the content that follows refer to Nomarski DIC microscopy. The Nikon Eclipse i80 microscope can be easily switched between epi-fluorescence mode and DF mode by simply changing some optical components.

Figure 6 illustrates the light path of the Nomarski DIC microscope setup. The red and blue lines in the schematic stand for the light paths of two orthogonal beams split by the first Nomarski prism. The Nikon Eclipse i80 microscope is equipped with a tungsten lamp (maximum output power of 100 Watts) as a light source. This relatively low illumination light power causes minimal cell disruption and fluorescence photobleaching. DIC mode employs a quarter-wave plate, two polarizers, two Nomarski prisms, a high NA condenser (1.4) and a high NA objective (1.4). Unpolarized light passes through the first polarizer and the polarized light is split into two orthogonal polarized beams. The beams are directed onto the sample by the condenser. The separation distance of these two beams is shear distance. The beams experience different optical paths due to varying sample thicknesses. They are collected by the objective and focused onto the second Nomarski prism where they recombine. The beams interfere with each other after their vibrations are brought into same plane and axis by the second polarizer. An appropriate band pass filter is usually added into the light path for wavelength dependent plasmonic nanoparticle detection. The interference pattern of the final DIC image is recorded using a CCD or COMS camera. In short, DIC

microscope is a two-beam interferometer that determines the optical path length gradients of the sample.

The DIC-based SPORT technique was initiated by Gufeng Wang for dynamic rotational tracking of anisotropic AuNRs (nonfluoresent plasmonic probes) in live cells.[59] The DIC images of AuNRs appear as disproportionate bright and dark spots. The DIC bright and dark intensities of an AuNR display periodic changes when the particle is rotated under a DIC microscope. The relative brightness (or relative darkness) is used to resolve the orientation of the AuNRs. The capacity of resolving rotational motions of AuNRs transported by motor proteins in 3D space was demonstrated both in an *in vitro* gliding assay experiment and in live cells. A later report in the group showed the use of this DIC-based SPORT technique to investigate the interactions of AuNRs with various surface modifiers and live cell membranes.[69]

A modified DIC microscope with the addition of a dual-view filter cube at the exit port of the microscope was used to obtain the signal for both DIC and fluorescence imaging at two wavelengths.[91] This dual-modality DIC/fluorescence SPORT technique allows the simultaneous imaging of fluorescently tagged biomolecules and plasmonic nanoprobes in living cells. Jiwon Ha *et al.* suggested the use of DIC polarization anisotropy in DIC-based SPORT technique in determining the orientation angle of AuNRs.[92] Data proved that DIC polarization anisotropy is less sensitive to intensity fluctuations and capable of providing more reliable measurements in dynamic studies compared to the conventional DIC-based SPORT technique based on the absolute bright and dark intensity measurements. Defocused DIC microscopy was also demonstrated for the direct determination of the spatial orientation based on the scattering intensity distribution of a AuNR when the particle is close to the

polarization directions.[93] Beside AuNRs, micrometer-long gold nanowires[94] and multishell Au/Ag/SiO2 core-shell nanorods[62] were also explored as novel orientation probes for the development and applications of DIC-based SPORT technique.

The PSF of a nanoparticle in DIC microscopy shows bright and dark intensity centers with gradients caused by the nature of the interference image formation. Simple Gaussian fitting of image profile as in DF and fluorescence microscopy does not work for DIC particle localizations.[21] Gelles *et al.* demonstrated a cross-correlation method for plastic beads localization in DIC microscopy with nanometer pricision[95] and this method was adopted by Yan Gu *et al.* for the 3D superlocalization of gold nanospheres.[96] It is challenging to localize anisotropic AuNRs in DIC microscopy as the AuNR DIC image patterns change when the particle rotates. This correlation mapping localization method is applicable with decent localization precision. The correlation mapping method is employed in 5D tracking algorithm as presented in chapter 3. Further discussions on the rotational data interpretation in DIC-based SPORT technique are included in chapter 4.

FIGURES

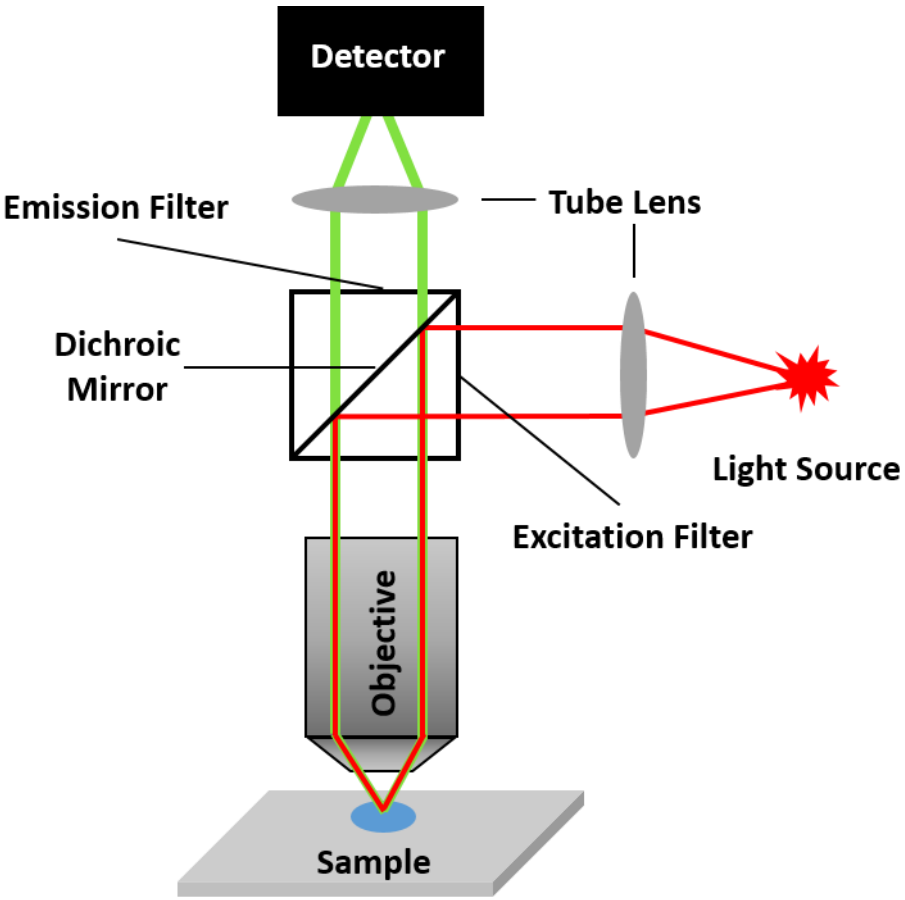

Figure 1. Schematic diagram of epi-fluorescence microscopy setup.

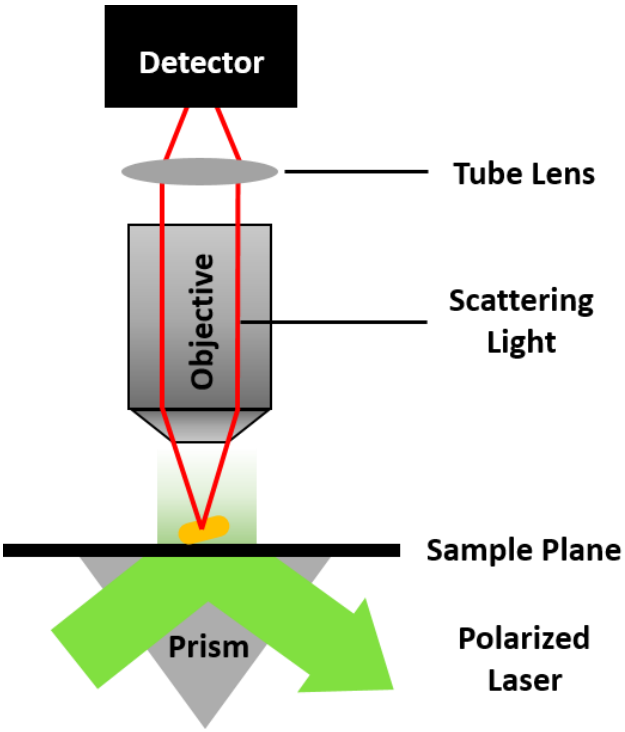

Figure 2. Schematic diagram of total internal reflection fluorescence microscopy setup. (It is not drawn to scale)

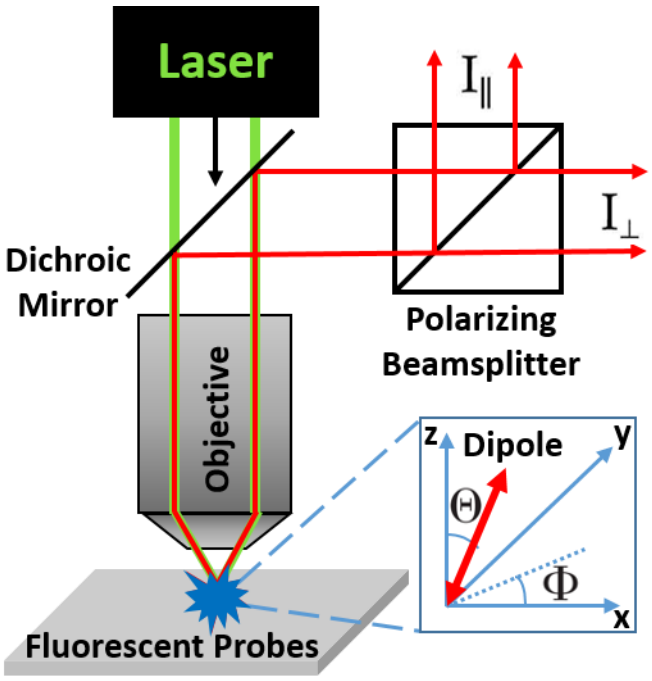

Figure 3. Schematic diagram of fluorescence polarization microscopy setup for SPORT applications.

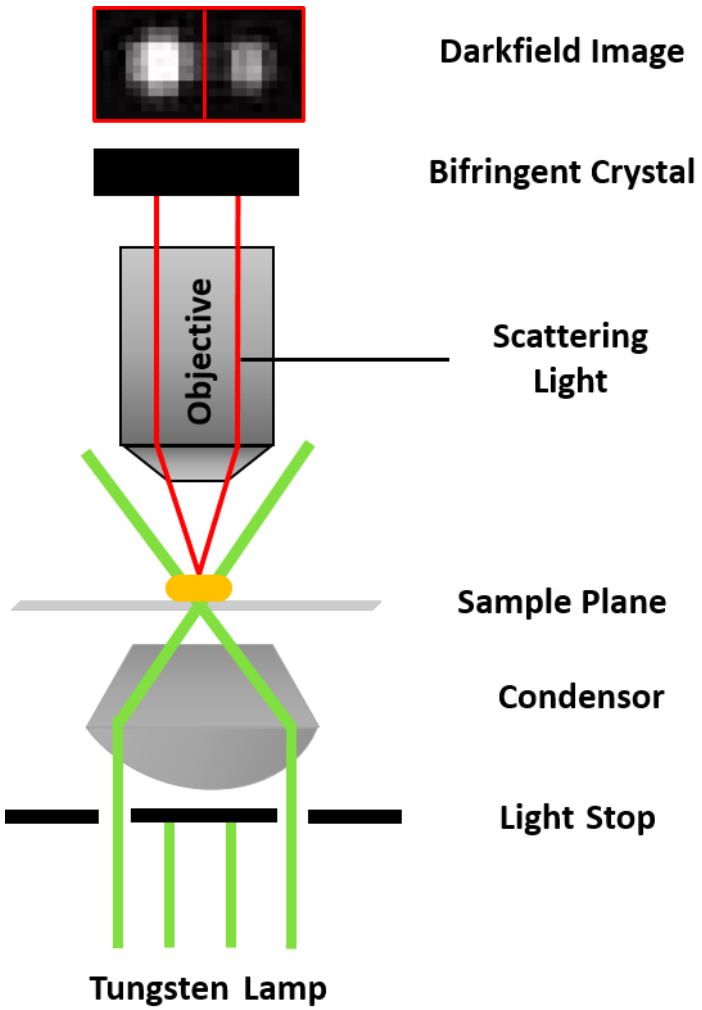

Figure 4. Schematic diagram of dark field microscopy setup for SPORT applications. (Adapted with permission from ref 58. Copyright © 2005 American Chemical Society.)

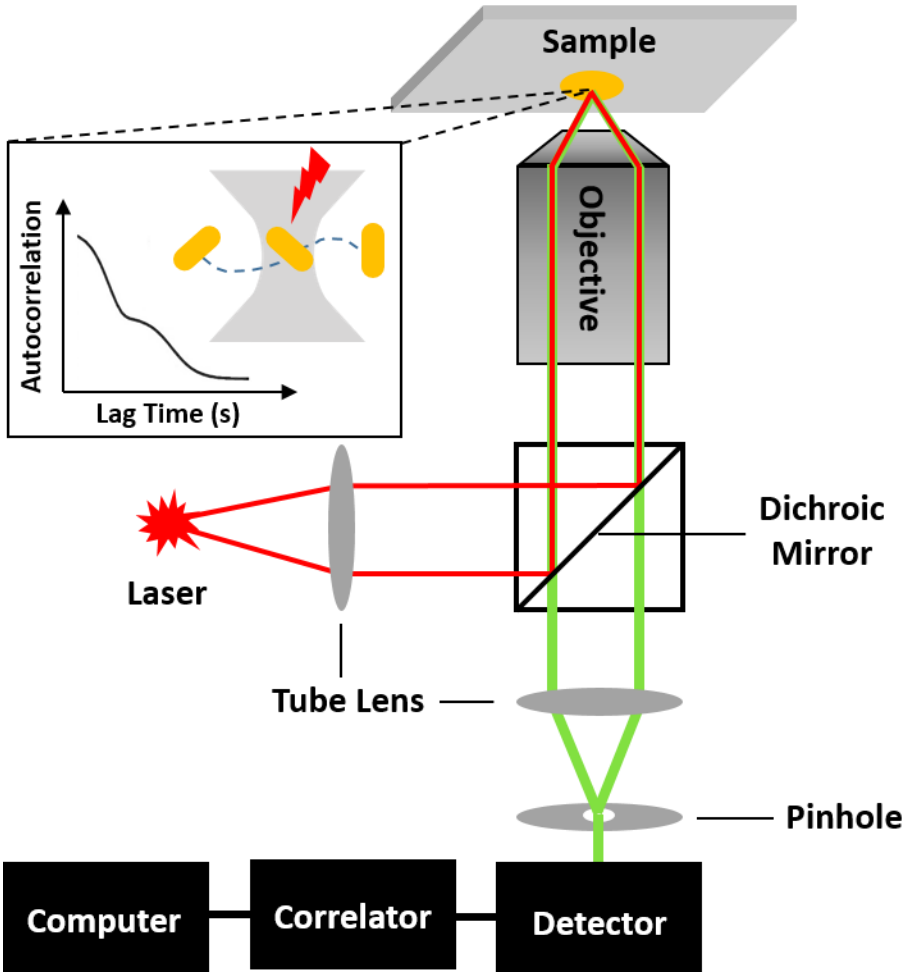

Figure 5. Schematic diagram of the typical FCS setup.

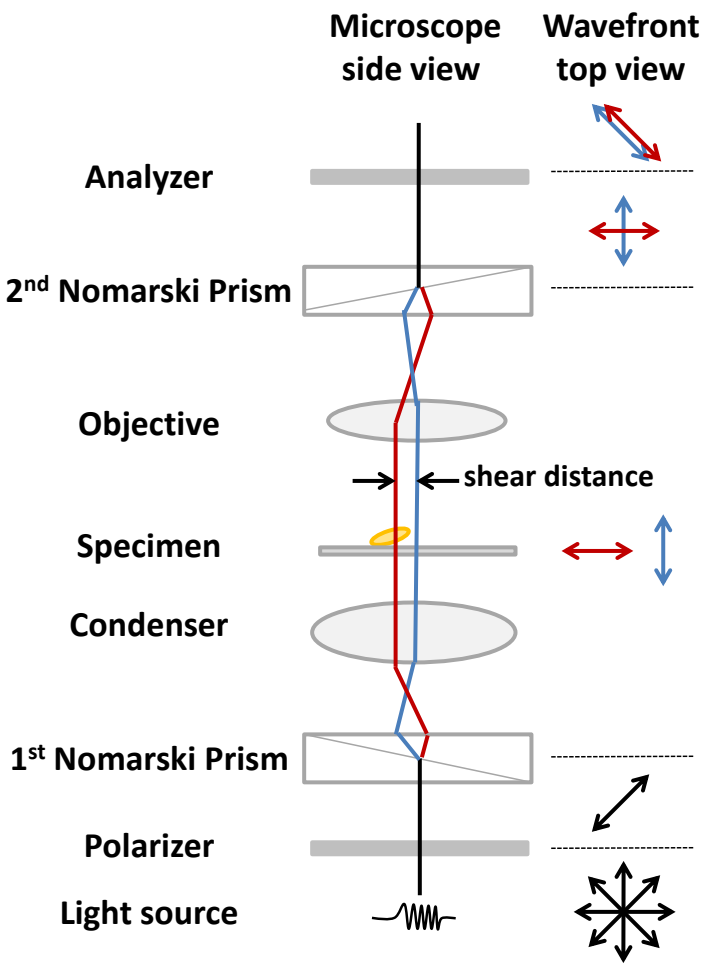

Figure 6. The light path of the Nomarski DIC microscope setup and wavefront of the light beams. (Adapted with permission from ref 49. Copyright © 2013 American Chemical Society.)

References

(1) Stephens, D. J.; Allan, V. J. *Science* **2003**, *300*, 82.

(2) Ji, N.; Shroff, H.; Zhong, H.; Betzig, E. *Curr. Opin. Neurobiol.* **2008**, *18*, 605.

(3) Jaqaman, K.; Loerke, D.; Mettlen, M.; Kuwata, H.; Grinstein, S.; Schmid, S. L.; Danuser, G. *Nat. Methods* **2008**, *5*, 695.

(4) Dorn, J. F.; Danuser, G.; Yang, G. *Methods Cell Biol.* **2008**, *85*, 497.

(5) Yildiz, A.; Forkey, J. N.; McKinney, S. A.; Ha, T.; Goldman, Y. E.; Selvin, P. R. *Science* **2003**, *300*, 2061.

(6) Saxton, M. J. *Nat. Methods* **2008**, *5*, 671.

(7) Jaqaman, K.; Danuser, G. *Cold Spring Harb. Protoc.* **2009**, pdb. top65.

(8) Rohr, K.; Godinez, W. J.; Harder, N.; Worz, S.; Mattes, J.; Tvarusko, W.; Eils, R. *Cold Spring Harb. Protoc.* **2010**, pdb. top80.

(9) Meijering, E.; Dzyubachyk, O.; Smal, I. *Methods Enzymol.* **2012**, *504*, 183.

(10) Chenouard, N.; Smal, I.; de Chaumont, F.; Maska, M.; Sbalzarini, I. F.; Gong, Y.; Cardinale, J.; Carthel, C.; Coraluppi, S.; Winter, M.; Cohen, A. R.; Godinez, W. J.; Rohr, K.; Kalaidzidis, Y.; Liang, L.; Duncan, J.; Shen, H.; Xu, Y.; Magnusson, K. E.; Jalden, J.; Blau, H. M.; Paul-Gilloteaux, P.; Roudot, P.; Kervrann, C.; Waharte, F.; Tinevez, J. Y.; Shorte, S. L.; Willemse, J.; Celler, K.; van Wezel, G. P.; Dan, H. W.; Tsai, Y. S.; Ortiz de Solorzano, C.; Olivo-Marin, J. C.; Meijering, E. *Nat. Methods* **2014**, *11*, 281.

(11) Carter, B. C.; Shubeita, G. T.; Gross, S. P. *Phys. Biol.* **2005**, *2*, 60.

(12) Godinez, W. J.; Lampe, M.; Worz, S.; Muller, B.; Eils, R.; Rohr, K. *Med. Image. Anal.* **2009**, *13*, 325.

(13) Ruusuvuori, P.; Aijo, T.; Chowdhury, S.; Garmendia-Torres, C.; Selinummi, J.; Birbaumer, M.; Dudley, A. M.; Pelkmans, L.; Yli-Harja, O. *BMC Bioinf.* **2010**, *11*, 248.

(14) Sage, D.; Kirshner, H.; Pengo, T.; Stuurman, N.; Min, J.; Manley, S.; Unser, M. *Nat. Methods* **2015**.

(15) Saxton, M. J.; Jacobson, K. *Annu. Rev. Biophys. Biomol. Struct.* **1997**, *26*, 373.

(16) Fujiwara, T.; Ritchie, K.; Murakoshi, H.; Jacobson, K.; Kusumi, A. *J Cell Biol.* **2002**, *157*, 1071.

(17) Yezhelyev, M. V.; Qi, L.; O'Regan, R. M.; Nie, S.; Gao, X. *J. Am. Chem. Soc.* **2008**, *130*, 9006.

(18) Gu, Y.; Sun, W.; Wang, G.; Jeftinija, K.; Jeftinija, S.; Fang, N. *Nat. Commun.* **2012**, *3*, 1030.

(19) Lakadamyali, M.; Rust, M. J.; Babcock, H. P.; Zhuang, X. *Proc. Natl. Acad. Sci. U. S. A.* **2003**, *100*, 9280.

(20) Gang, R.; Amit, A.; Adam, I.; Shuming, N. *J. Am. Chem. Soc.* **2007**, *129*, 14759

(21) Deschout, H.; Cella Zanacchi, F.; Mlodzianoski, M.; Diaspro, A.; Bewersdorf, J.; Hess, S. T.; Braeckmans, K. *Nat. Methods* **2014**, *11*, 253.

(22) Toprak, E.; Balci, H.; Blehm, B. H.; Selvin, P. R. *Nano Lett.* **2007**, *7*, 2043.

(23) Kao, H. P.; Verkman, A. S. *Biophys. J.* **1994**, *67*, 1291.

(24) Huang, B.; Wang, W.; Bates, M.; Zhuang, X. *Science* **2008**, *319*, 810.

(25) Yajima, J.; Mizutani, K.; Nishizaka, T. *Nat. Struct. Mol. Biol.* **2008**, *15*, 1119.

(26) Baddeley, D.; Cannell, M.; Soeller, C. *Nano Res.* **2011**, *4*, 589.

(27) Sun, Y.; McKenna, J. D.; Murray, J. M.; Ostap, E. M.; Goldman, Y. E. *Nano Lett.* **2009**, *9*, 2676.

(28) Lew, M. D.; Lee, S. F.; Badieirostami, M.; Moerner, W. E. *Opt. Lett.* **2011**, *36*, 202.

(29) Pavani, S. R. P.; Piestun, R. *Opt. Express* **2008**, *16*, 22048.

(30) Thompson, M. A.; Lew, M. D.; Badieirostami, M.; Moerner, W. E. *Nano Lett.* **2010**, *10*, 211.

(31) Shechtman, Y.; Weiss, L. E.; Backer, A. S.; Sahl, S. J.; Moerner, W. E. *Nano Lett.* **2015**. *15*, 4194.

(32) de Belder, A. N.; Granath, K. *Carbohydr. Res.* **1973**, *30*, 375.

(33) Rust, M. J.; Bates, M.; Zhuang, X. *Nat. Methods* **2006**, *3*, 793.

(34) Betzig, E.; Patterson, G. H.; Sougrat, R.; Lindwasser, O. W.; Olenych, S.; Bonifacino, J. S.; Davidson, M. W.; Lippincott-Schwartz, J.; Hess, H. F. *Science* **2006**, *313*, 1642.

(35) Hess, S. T.; Girirajan, T. P.; Mason, M. D. *Biophys. J.* **2006**, *91*, 4258.

(36) Viswanathan, S.; Williams, M. E.; Bloss, E. B.; Stasevich, T. J.; Speer, C. M.; Nern, A.; Pfeiffer, B. D.; Hooks, B. M.; Li, W. P.; English, B. P.; Tian, T.; Henry, G. L.; Macklin, J. J.; Patel, R.; Gerfen, C. R.; Zhuang, X.; Wang, Y.; Rubin, G. M.; Looger, L. L. *Nat. Methods* **2015**, *12*, 568.

(37) Chan, W. C.; Nie, S. *Science* **1998**, *281*, 2016.

(38) Resch-Genger, U.; Grabolle, M.; Cavaliere-Jaricot, S.; Nitschke, R.; Nann, T. *Nat. Methods* **2008**, *5*, 763.

(39) Rochira, J. A.; Gudheti, M. V.; Gould, T. J.; Laughlin, R. R.; Nadeau, J. L.; Hess, S. T. *J. Phys. Chem. C* **2007**, *111*, 1695.

(40) Kuno, M.; Fromm, D. P.; Hamann, H. F.; Gallagher, A.; Nesbitt, D. J. *J. Chem. Phys.* **2000**, *112*, 3117.

(41) Bradburne, C. E.; Delehanty, J. B.; Boeneman Gemmill, K.; Mei, B. C.; Mattoussi, H.; Susumu, K.; Blanco-Canosa, J. B.; Dawson, P. E.; Medintz, I. L. *Bioconjugate Chem.* **2013**, *24*, 1570.

(42) Marchuk, K.; Guo, Y.; Sun, W.; Vela, J.; Fang, N. *J. Am. Chem. Soc.* **2012**, *134*, 6108.

(43) Keller, A. M.; Ghosh, Y.; DeVore, M. S.; Phipps, M. E.; Stewart, M. H.; Wilson, B. S.; Lidke, D. S.; Hollingsworth, J. A.; Werner, J. H. *Adv. Funct. Mater.* **2014**, *24*, 4796.

(44) Wustner, D.; Solanko, L. M.; Lund, F. W.; Sage, D.; Schroll, H. J.; Lomholt, M. A. *BMC Bioinf.* **2012**, *13*, 296.

(45) Axelrod, D.; Koppel, D. E.; Schlessinger, J.; Elson, E.; Webb, W. W. *Biophys. J.* **1976**, *16*, 1055.

(46) Aitken, C. E.; Marshall, R. A.; Puglisi, J. D. *Biophys. J.* **2008**, *94*, 1826.

(47) Lidke, K.; Rieger, B.; Jovin, T.; Heintzmann, R. *Opt. Express* **2005**, *13*, 7052.

(48) Sun, W.; Xiao, L.; Fang, N. In *Cell Imaging Techniques*; Taatjes, D. J., Roth, J., Eds.; Humana Press: **2013**; *931*, 169.

(49) Stender, A. S.; Marchuk, K.; Liu, C.; Sander, S.; Meyer, M. W.; Smith, E. A.; Neupane, B.; Wang, G.; Li, J.; Cheng, J.-X.; Huang, B.; Fang, N. *Chem. Rev.* **2013**, *113*, 2469.

(50) Wang, G.; Stender, A. S.; Sun, W.; Fang, N. *Analyst* **2010**, *135*, 215.

(51) Olson, J.; Dominguez-Medina, S.; Hoggard, A.; Wang, L.-Y.; Chang, W.-S.; Link, S. *Chem. Soc. Rev.* **2015**, *44*, 40.

(52) Jain, P. K.; Huang, X.; El-Sayed, I. H.; El-Sayed, M. A. *Acc. Chem. Res.* **2008**, *41*, 1578.

(53) Xu, Z.; Kong, W.; Cheng, L.; Ma, A.; Lu, X.; Wang, Y.; Zhang, X.; Zhang, X. *Plasmonics* **2015**.

(54) Nikoobakht, B.; El-Sayed, M. A. *Chem. Mater.* **2003**, *15*, 1957.

(55) Murphy, C. J.; Jana, N. R. *Adv. Mater.* **2002**, *14*, 80.

(56) Chen, H.; Shao, L.; Li, Q.; Wang, J. *Chem. Soc. Rev.* **2013**, *42*, 2679.

(57) Chang, W.-S.; Ha, J. W.; Slaughter, L. S.; Link, S. *Proc. Natl. Acad. Sci. U. S. A.* **2010**, *107*, 2781.

(58) Sonnichsen, C.; Alivisatos, A. P. *Nano Lett.* **2005**, *5*, 301.

(59) Wang, G.; Sun, W.; Luo, Y.; Fang, N. *J. Am. Chem. Soc.* **2010**, *132*, 16417.

(60) Song, E. Q.; Hu, J.; Wen, C. Y.; Tian, Z. Q.; Yu, X.; Zhang, Z. L.; Shi, Y. B.; Pang, D. W. *ACS Nano* **2011**, *5*, 761.

(61) Cortie, M. B.; McDonagh, A. M. *Chem. Rev.* **2011**, *111*, 3713.

(62) Encai, H.; George, C. S.; Joseph, T. H. *J. Fluoresc.* **2004**, *14*, 331341.

(63) Chen, K.; Lin, C.-C.; Vela, J.; Fang, N. *Anal. Chem.* **2015**, *87*, 4096.

(64) Saha, A.; Basiruddin, S. K.; Sarkar, R.; Pradhan, N.; Jana, N. R. *J. Phys. Chem. C* **2009**, *113*, 18492.

(65) Basiruddin, S. K.; Saha, A.; Pradhan, N.; Jana, N. R. *J. Phys. Chem. C* **2010**, *114*, 11009.

(66) Ryohei, Y.; Hiroyuki, N.; Masasuke, Y.; Kazuhiko, K.; Hiroyasu, I. *Nature* **2001**, *410*, 898.

(67) Kural, C.; Kim, H.; Syed, S.; Goshima, G.; Gelfand, V. I.; Selvin, P. R. *Science* **2005**, *308*, 1469.

(68) Joseph, N. F.; Margot, E. Q.; Shaw, M. A.; John, E. T. C.; Yale, E. G. *Nature* **2003**, *422*, 399.

(69) Shou, W.; Bruce, S. *Annu. Rev. Biochem.* **1998**, *67*, 721.

(70) Gu, Y.; Sun, W.; Wang, G.; Fang, N. *J. Am. Chem. Soc.* **2011**, *133*, 5720.

(71) Gu, Y.; Ha, J. W.; Augspurger, A. E.; Chen, K.; Zhu, S.; Fang, N. *Nanoscale* **2013**, *5*, 10753.

(72) Hoskins, L. C. *J. Chem. Educ.* **1975**, *52*, 568.

(73) Hustedt, E. J.; Cobb, C. E.; Beth, A. H.; Beechem, J. M. *Biophys. J.* **1993**, *64*, 614.

(74) Axelrod, D. *J. Cell Biol.* **1981**, *89*, 141.

(75) Schneckenburger, H. *Curr. Opin. Biotechnol.* **2005**, *16*, 13.

(76) Mattheyses, A. L.; Simon, S. M.; Rappoport, J. Z. *J Cell Sci.* **2010**, *123*, 3621.

(77) Forkey, J. N.; Quinlan, M. E.; Shaw, M. A.; Corrie, J. E.; Goldman, Y. E. *Nature* **2003**, *422*, 399.

(78) Ha, T.; Laurence, T. A.; Chemla, D. S.; Weiss, S. *J. Phys. Chem. B* **1999**, *103*, 6839.

(79) Sase, I.; Miyata, H.; Ishiwata, S.; Kinosita, K., Jr. *Proc. Natl. Acad. Sci. U. S. A.* **1997**, *94*, 5646.

(80) Toprak, E.; Enderlein, J.; Syed, S.; McKinney, S. A.; Petschek, R. G.; Ha, T.; Goldman, Y. E.; Selvin, P. R. *Proc. Natl. Acad. Sci. U. S. A.* **2006**, *103*, 6495.

(81) Beausang, J. F.; Sun, Y.; Quinlan, M. E.; Forkey, J. N.; Goldman, Y. E. *Cold Spring Harb. Protoc.* **2012**, 535.

(82) Ueno, H.; Nishikawa, S.; Iino, R.; Tabata, K. V.; Sakakihara, S.; Yanagida, T.; Noji, H. *Biophys. J.* **2010**, *98*, 2014.

(83) Sönnichsen, C.; Alivisatos, A. P. *Nano Lett.* **2005**, *5*, 301.

(84) Xiao, L.; Qiao, Y.; He, Y.; Yeung, E. S. *Anal. Chem.* **2010**, *82*, 5268.

(85) Ha, J. W.; Marchuk, K.; Fang, N. *Nano Lett.* **2012**, *12*, 4282.

(86) Marchuk, K.; Fang, N. *Nano Lett.* **2013**, *13*, 5414.

(87) Zhang, B.; Lan, T.; Huang, X.; Dong, C.; Ren, J. *Anal. Chem.* **2013**, *85*, 9433.

(88) Boyer, D.; Tamarat, P.; Maali, A.; Lounis, B.; Orrit, M. *Science* **2002**, *297*, 1160.

(89) Huang, X.; El-Sayed, I. H.; Qian, W.; El-Sayed, M. A. *J. Am. Chem. Soc.* **2006**, *128*, 2115.

(90) Tcherniak, A.; Dominguez-Medina, S.; Chang, W.-S.; Swanglap, P.; Slaughter, L. S.; Landes, C. F.; Link, S. *J. Phys. Chem. C* **2011**, *115*, 15938.

(91) Mehta, S. B.; Sheppard, C. J. *Opt. Express* **2008**, *16*, 19462.

(92) Sun, W.; Gu, Y.; Wang, G.; Fang, N. *Anal. Chem.* **2012**, *84*, 1134.

(93) Won Ha, J.; Sun, W.; Wang, G.; Fang, N. *Chem. Commun.* **2011**, *47*, 7743.

(94) Ha, J. W.; Fang, N. *Chem. Commun.* **2014**, *50*, 5500.

(95) Ha, J. W.; Chen, K.; Fang, N. *Chem. Commun.* **2013**, *49*, 11038.

(96) Gelles, J.; Schnapp, B. J.; Sheetz, M. P. *Nature* **1988**, *331*, 450.

(97) Gu, Y.; Di, X.; Sun, W.; Wang, G.; Fang, N. *Anal. Chem.* **2012**, *84*, 4111.

CHAPTER 2

MULTISHELL Au/Ag/SiO_2 NANORODS WITH TUNABLE OPTICAL PROPERTIES AS SINGLE PARTICLE ORIENTATION AND ROTATIONAL TRACKING PROBES

Modified from the paper published in Analytical Chemistry, 2015, 87, 4096–4099.

Kuangcai Chen,[†] *Chia-Cheng Lin,*[†] *Javier Vela,** and *Ning Fang**

Ames Laboratory, U.S. Department of Energy, and Department of Chemistry, Iowa State University, Ames, Iowa 50011, United States

* To whom correspondence should be addressed.
Email: vela@iastate.edu; nfang@iastate.edu

Abstract

Three-layer core-shell plasmonic nanorods (Au/Ag/SiO_2-NRs), consisting of a gold nanorod core, a thin silver shell, and third, thin silica layer were synthesized and used as optical imaging probes under a differential interference contrast microscope for single particle orientation and rotational tracking. The localized surface plasmon resonance modes were enhanced upon the addition of the silver shell, and the anisotropic optical properties of gold nanorods were maintained. The silica coating enables surface functionalization with silane coupling agents and provides enhanced stability and biocompatibility. Taking advantage of the longitudinal LSPR enhancement, the orientation and rotational information of the hybrid nanorods on synthetic lipid bilayers and on live cell membranes were obtained

with millisecond temporal resolution using a scientific complementary metal-oxide-semiconductor camera. The results demonstrate that the as-synthesized hybrid nanorods are promising imaging probes with improved sensitivity and good biocompatibility for single plasmonic particle tracking experiments in biological systems.

Introduction

Single particle tracking (SPT) is a powerful tool to study the dynamics of cellular and molecular processes, such as membrane dynamics,[1,2] viral infection,[3] and intracellular transport.[4,5] A large collection of imaging probes, including fluorescent molecules,[6,7] quantum dots,[8,9] and plasmonic nanoparticles,[5,10-16] have been visualized with the aid of various optical microscopy techniques. While it has become a routine practice in SPT experiments to identify the trajectory of an imaging probe, it is more difficult to resolve the dipole orientation of the probe in real time, which may be essential in understanding the underlying biological functions. Recently, considerable efforts have been made to overcome this challenge. Techniques such as fluorescence polarization microscopy,[6-8] dark field polarization scattering,[10] defocused orientation and position imaging,[9,13] photothermal imaging,[11] correlation spectroscopy,[12,14] total internal reflection scattering microscopy,[15,17] and differential interference contrast (DIC) microscopy[18,19] have been developed for *single particle orientation and rotational tracking*, which was coined as SPORT.[19,20]

Gold nanorods (AuNRs) have been used extensively in SPORT experiments because of their high photostability, good biocompatibility, and most importantly, anisotropic optical properties arising from their localized surface plasmon resonance (LSPR). Great success has been achieved on the AuNR synthesis using seed-mediated methods to fabricate a variety of

AuNRs with different sizes, aspect ratios, and thus the resulting tunable extinction spectra across a wide spectral range.[21,22] Compared with gold nanocrystals of similar size, silver nanocrystals exhibit stronger LSPR responses with more intense electric field enhancement and stronger absorption and scattering. However, the synthesis of anisotropic silver nanorods (AgNRs), especially for the smaller sizes (< 100 nm in length) that are better suited for biological studies, is more difficult than that of AuNRs in terms of size and shape uniformity control.[23,24] Since silver shares the same face centered cubic crystal structure with gold and their lattice mismatch is as small as 0.27%, AuNRs are suitable templates for epitaxial silver growth to form Au/Ag core-shell nanorods (Au/AgNRs).[25-30] The optical properties of Au/AgNRs can be finely tuned by controlling the aspect ratio of the AuNR cores and the amount of silver grown on the gold surface.[29] Moreover, the formation of Au/AgNRs induces multiple plasmonic bands that differ from single-component nanocrystals.

In view of the intrinsic cytotoxicity and instable nature of the silver shells in aqueous solution,[23,31,32] encapsulation of Au/AgNRs within a thin silica layer to form a three-layer core-shell nanorod structure, which will be referred to as Au/Ag/SiO_2-NR in this letter, can provide the necessary protection in biological imaging applications. The silica coating also improves the colloidal stability of Au/AgNRs, maintains the rod shape, and enables further surface functionalization with silane coupling agents for potential bioconjugation.[33-35] Surface modification of the silica shell usually involves covalent attachment; therefore, this avoids cysteine residue replacement of thiol ligands, which is often used in gold or silver surface functionalization.[36]

In the present study, Au/Ag/SiO_2-NRs were synthesized and tested for SPORT experiments. Millisecond/sub-millisecond temporal resolution was achieved in imaging the

fast dynamics of Au/Ag/SiO_2-NRs rotating on synthetic lipid membranes and live cell membranes. To the best of our knowledge, this study demonstrates for the first time the development and application of hybrid core-shell nanorods as a new type of rotational probe.

Results and Discussion

The first step in synthesizing Au/Ag/SiO_2-NRs was to prepare AuNRs using a seed-mediated growth method in aqueous solution utilizing cetyltrimethylammonium bromide (CTAB) as capping agent to maintain colloidal stability.[21] The average diameter, length, and aspect ratio of the synthesized AuNRs obtained from the TEM images (**Figure S1** in the Supporting Information) were 22. 8 ± 3.2 nm, 52.6 ± 7.2 nm, and 2.3 ± 0.2, respectively. Their transverse and longitudinal LSPR wavelengths were centered at 517 nm and 632 nm, as shown in the UV-Vis extinction spectrum (Figure 1, green curve).

In the second step of synthesis, a thin silver layer (~7 nm thick) was deposited onto the AuNRs following a published procedure.[25,37] The thickness of the silver coating was controlled by adjusting the amount of $AgNO_3$ precursor. Upon the addition of silver onto the AuNR cores, the extinction peak at the lowest energy wavelength was blue-shifted and new plasmonic bands appeared at higher energies. **Figure S2** in the Supporting Information illustrates the UV-Vis extinction spectra of the Au/AgNRs with three Ag/Au molar ratios of 0.11, 0.22, and 0.34. As the Ag/Au molar ratio increases, the silver shell becomes thicker and the longitudinal LSPR wavelength is blue-shifted from 632 nm to 563, 537, and 503 nm, respectively. This blue shift is attributed to the reduced aspect ratio of the nanorods after the silver coating and the increased silver loading on gold dominates the optical properties. This plasmonic band shift can be used to estimate the Ag shell thickness as well as to direct

further syntheses.[26,28,30] The Au/AgNRs with the Ag/Au molar ratio of 0.11 maintained the original cylindrical rod shape. **Figure S2** curve b in the Supporting Information shows the four plasmonic bands at 339, 400, 506, and 563 nm. The rise of two higher energy bands at shorter wavelengths is believed to be due to the octupolar plasmonic modes, with the peaks at 506 nm and 563 nm corresponding to the transverse and longitudinal dipolar plasmonic modes.[25,27,28] At higher Ag/Au molar ratios, the rod shape was no longer maintained and a large fraction of irregular silver shells was observed (data not shown). Only the rod-shaped Au/AgNRs made with the Ag/Au molar ratio of 0.11 were used in the following synthesis and imaging experiments.

In order to improve the stability and reduce the intrinsic toxicity of silver, a dense silica layer was added as the last synthetic step. Figure 1 compares the normalized UV-Vis extinction spectra of AuNRs, Au/AgNRs, and Au/Ag/SiO_2-NRs. In these measurements, the colloidal solutions were kept at the same concentration to minimize the dilution effect. Figure 1 (inset) shows a representative TEM image of the core-shell structure with average dimensions of ~ 46 nm × 64 nm. Due to the relatively low lattice mismatch (0.27%) of the two metals, the Ag shells grow near perfectly upon the AuNRs through epitaxial deposition. We also found that the Ag shell thickness increases faster along the lateral direction than at the tips, which leads to the reduction of the aspect ratio of Au/AgNRs from the original AuNRs. In view of their relative extinction intensities, the longitudinal dipolar plasmonic mode increases by roughly a factor of 3 in Au/AgNRs compared to that of the original AuNRs. The baseline in the UV-Vis extinction spectrum of the Au/Ag/SiO_2-NR solution is elevated because of scattering caused by silica, as reported previously.[33]

Following the synthesis, the Au/Ag/SiO_2-NRs were imaged under a DIC microscope equipped with a Hamamatsu ORCA-Flash 2.8 scientific CMOS camera, which allows imaging at millisecond or sub-millisecond temporal resolution. In addition to the enhanced LSPR response from the silver coating, the blue shift of the LSPR wavelength from 632 nm (AuNRs) to 563 nm provides another noticeable gain in the camera's quantum efficiency and therefore sensitivity.

In our previous studies, the DIC contrasts, defined as the difference between the brightest and the darkest intensities divided by the average local background intensity, of nanoparticles were shown to be wavelength dependent and the longitudinal LSPR was more sensitive to the environment than the transverse LSPR.[18,38] Herein, the DIC contrast of an immobilized, randomly oriented Au/Ag/SiO_2-NR is plotted as a function of excitation wavelength (**Figure S3** in the Supporting Information). The highest DIC contrast for this particle was found when a 585 ± 29 nm filter was used for illumination, which corresponds to the longitudinal dipolar plasmonic band.

DIC images of two immobilized Au/Ag/SiO_2-NRs on glass slides were recorded at different exposure times and stitched together to make **Movie S1** in the Supporting Information, which is played at 30 frames per second (fps). These two particles in the movie were nearly perpendicular to each other as their DIC images showed the totally bright and totally dark patterns. During these measurements, the light source was kept at the maximum output power (100 Watts), and the overall intensity decreased linearly as expected when shorter exposure time was used (**Figure S4** in the Supporting Information). The relative bright and dark intensity measurement errors were increased from ~1% at 50 ms to ~5% at 0.5 ms for both nanorods (**Table S1** in the Supporting Information). Because of the LSPR

enhancement due to the silver coating, the core-shell hybrid nanorods were detectable at a temporal resolution as fast as 0.5 ms, which is approximately an order of magnitude faster than the previously reported fastest temporal resolution of 2 - 5 ms.[5,19]

A 360° rotation study of the Au/Ag/SiO_2-NRs was carried out by rotating the sample stage with 10° increments to position the nanorods in different orientations while exciting at the longitudinal LSPR wavelength of 563 nm. The orientation angle φ was defined as the angle between the long axis of the nanorod and the "bright" polarization direction of the DIC microscope (**Figure S5A** in the Supporting Information). The "bright" polarization direction is named after the fact that a completely bright DIC image is obtained when the nanorod's long axis aligns with this polarization direction (φ = 0), while the "dark" polarization direction corresponds to a completely dark DIC image. **Figure S5B** in the Supporting Information shows the complete rotation set of disproportionate bright and dark DIC image patterns. The DIC images change periodically as the nanorod's long axis rotates against the polarization directions. This is in good agreement with the polarization-dependent rotation behaviors of plasmonic nanoparticles that have been extensively investigated in gold nanorods and nanowires.[18,39] In view of the periodic changes, a correlation between the bright and dark intensity traces is observed: the bright and dark intensities increase and decrease in the same direction. This orientation/polarization dependence is the foundation for the use of Au/Ag/SiO_2-NRs as SPORT probes.

Dynamic tracking of the Au/Ag/SiO_2-NRs was first performed on synthetic lipid bilayers. The nanorods were introduced onto the synthetic lipid bilayers in a chamber and bound to the membrane through non-specific interactions. Movies were recorded at a temporal resolution of 1 ms under 588 ± 29 nm illumination. **Figure S6** in the Supporting

Information shows the DIC intensity traces extracted from a representative 4-s (4000 frames) movie. The autocorrelation analysis of the DIC bright and dark traces[19] reveals that the nanorod's rotation speed fluctuates constantly. Representative examples of slow and fast rotation are given in Figure 2. The mean relaxation times of these two cases are 0.59 s (slow) and 0.024 s (fast).

To demonstrate the suitability of the new rotational probes for live-cell imaging, A549 human lung cancer cells were used as a model system, which provided a dynamic surface for rotational studies. Despite the much more complex cellular environments, the wavelength dependent properties of these SPORT probes are easily distinguishable from other cellular features by using different band pass filters. Three band pass filters (480 ± 40 nm, 588 ± 29 nm, and 700 ± 13 nm) were used to identify the nanorods. As shown in Figure 3, the 588 ± 29 nm filter, which covers the longitudinal LSPR band, results in a high-contrast DIC image of Au/Ag/SiO_2-NRs that is distinct from the background. With either 480 ± 40 nm or 700 ± 13 nm band pass filters, the Au/Ag/SiO_2-NRs disappear into the background due to the low contrast achieved at these wavelengths, which are far away from the LSPR bands.

In the live-cell imaging experiments, the Au/Ag/SiO_2-NRs were added into a chamber with A549 cells attached on the coverslip. Movies of the dynamic rotation of these nanorods were recorded at different exposure times of 1 ms, 5 ms, and 50 ms. The DIC intensity traces and the corresponding sets of consecutive DIC images were plotted in **Figure S7** in the Supporting Information. The autocorrelation analysis of the DIC bright and dark traces gives mean relaxation times of 11 ms at the temporal resolution of 1 ms, 23 ms at 5 ms, and 115 ms at 50 ms. Higher temporal resolution helps to unveil fast rotational dynamics, even though the overall intensity inevitably decreases as the single-frame exposure time decreases.

Conclusions

In summary, we have successfully synthesized Au/Ag/SiO_2-NRs with well-controlled size and shape for SPORT. These optically anisotropic hybrid plasmonic nanorods exhibit orientation/polarization and wavelength dependent behavior in DIC microscopy. With the enhancement of the longitudinal dipolar LSPR after silver coating, these nanorods provide sufficient sensitivity for detection at millisecond temporal resolution on both synthetic lipid bilayers and live cell membranes. Surface modification of the silica layer of the hybrid nanorods will enable versatile applications in SPORT.

Author Information

Corresponding author

*E-mail: vela@iastate.edu; nfang@iastate.edu

Notes

The authors declare no competing financial interest.

†These authors contributed equally to this work.

Acknowledgments

This research is supported by the U.S. Department of Energy, Office of Basic Energy Sciences, Division of Chemical Sciences, Geosciences, and Biosciences through the Ames Laboratory. The Ames Laboratory is operated for the U.S. Department of Energy by Iowa State University under Contract No. DE-AC02-07CH11358. The authors thank Michelle Thompson for assistance.

Associated Content

Supporting Information Available: Experimental details and additional figures and movies as mentioned in the main text. This material is available free of charge via the Internet at http://pubs.acs.org.

FIGURES

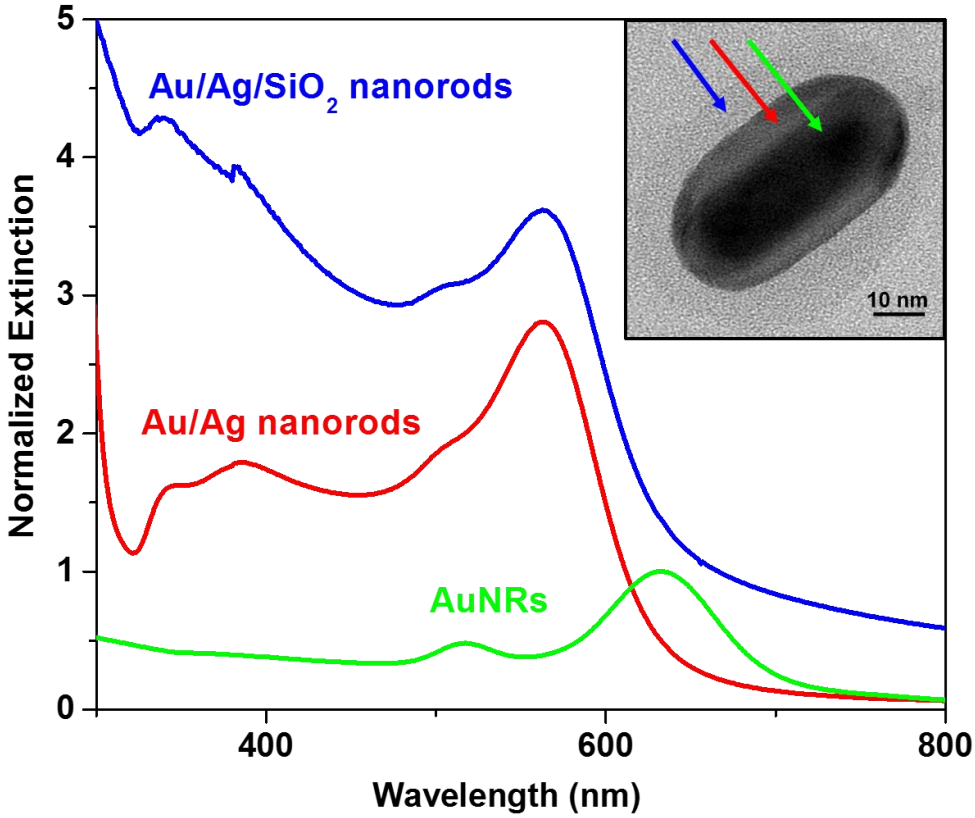

Figure 1. Normalized UV-Vis extinction spectra of AuNRs, Au/AgNRs and Au/Ag/SiO_2-NRs in water. All the spectra are normalized to the longitudinal dipolar plasmonic peak at 632 nm. The inset is a representative TEM image of Au/Ag/SiO_2-NR and the colored arrows indicate gold-only (green), silver-coated (red), and silica-coated (blue) samples.

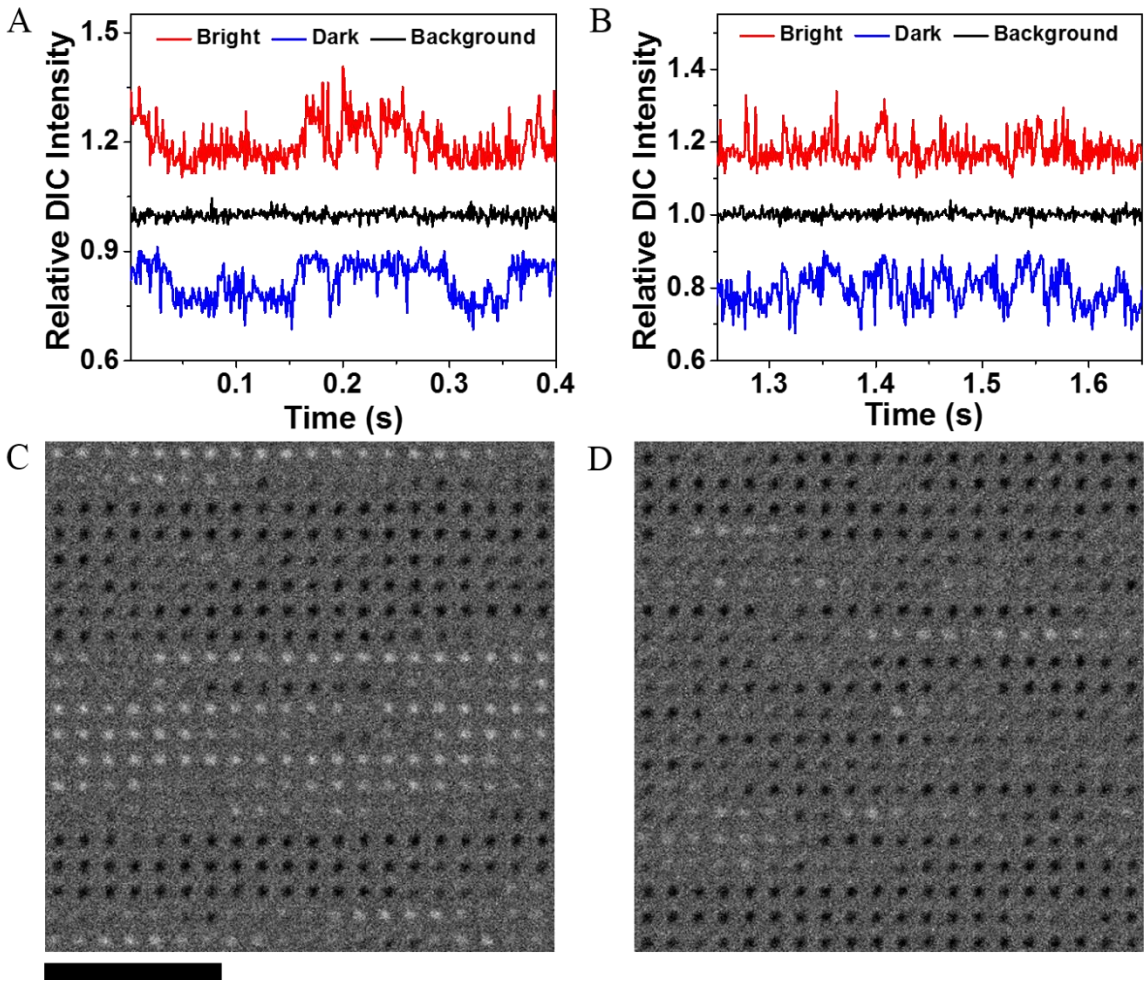

Figure 2. Relative DIC intensity traces of (A) slow rotation and (B) fast rotation, corresponding to the shaded gray and green areas in **Figure S5** of the Supporting Information. Four hundred (400) consecutive recorded DIC images for (A) and (B) are stitched together (from left to right and from top to bottom) and shown as (C) and (D), respectively. Scale bar is 5 μm.

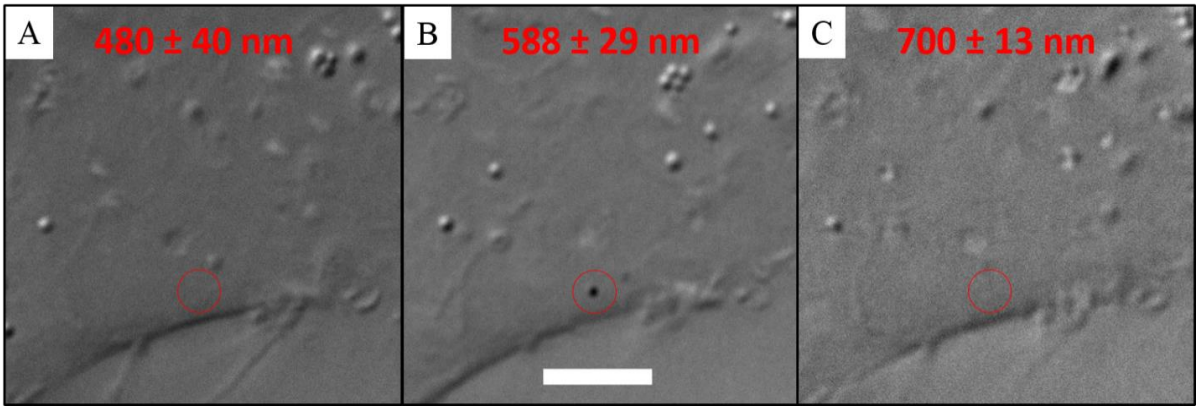

Figure 3. Differentiation of the Au/Ag/SiO_2-NRs (highlighted in the red circles) from other cellular features using three filters, (A) 480 ± 40 nm, (B) 588 ± 29 nm, and (C) 700 ± 13 nm. Scale bar is 4 µm. These images were taken sequentially. The nanorod and many cellular features changed their location and/or morphology during the imaging time.

References

(1) Saxton, M. J.; Jacobson, K. *Annu. Rev. Biophys. Biomol. Struct.* **1997**, *26*, 373-399.

(2) Fujiwara, T.; Ritchie, K.; Murakoshi, H.; Jacobson, K.; Kusumi, A. *J. Cell Biol.* **2002**, *157*, 1071-1081.

(3) Lakadamyali, M.; Rust, M. J.; Babcock, H. P.; Zhuang, X. *Proc. Natl. Acad. Sci. USA* **2003**, *100*, 9280-9285.

(4) Yezhelyev, M. V.; Qi, L.; O'Regan, R. M.; Nie, S.; Gao, X. *J. Am. Chem. Soc.* **2008**, *130*, 9006-9012.

(5) Gu, Y.; Sun, W.; Wang, G.; Jeftinija, K.; Jeftinija, S.; Fang, N. *Nat. Commun.* **2012**, *3*, 1030.

(6) Greeson, J. N.; Raphael, R. M. *J. Biomed. Opt.* **2007**, *12*, 021002-021002-021009.

(7) Beausang, J. F.; Sun, Y.; Quinlan, M. E.; Forkey, J. N.; Goldman, Y. E. *Cold Spring Harb. Protoc.* **2012**, *2012*, 535-545.

(8) Chung, I.; Shimizu, K. T.; Bawendi, M. G. *Proc. Natl. Acad. Sci. USA* **2003**, *100*, 405-408.

(9) Toprak, E.; Enderlein, J.; Syed, S.; McKinney, S. A.; Petschek, R. G.; Ha, T.; Goldman, Y. E.; Selvin, P. R. *Proc. Natl. Acad. Sci. USA* **2006**, *103*, 6495-6499.

(10) Sönnichsen, C.; Alivisatos, A. P. *Nano Lett.* **2004**, *5*, 301-304.

(11) Chang, W.-S.; Ha, J. W.; Slaughter, L. S.; Link, S. *Proc. Natl. Acad. Sci. USA* **2010**, *107*, 2781-2786.

(12) Tcherniak, A.; Dominguez-Medina, S.; Chang, W.-S.; Swanglap, P.; Slaughter, L. S.; Landes, C. F.; Link, S. *J. Phys. Chem. C* **2011**, *115*, 15938-15949.

(13) Li, T.; Li, Q.; Xu, Y.; Chen, X. J.; Dai, Q. F.; Liu, H.; Lan, S.; Tie, S.; Wu, L. J. *ACS Nano* **2012**, *6*, 1268-1277.

(14) Zhang, B.; Lan, T.; Huang, X.; Dong, C.; Ren, J. *Anal. Chem.* **2013**, *85*, 9433-9438.

(15) Marchuk, K.; Ha, J. W.; Fang, N. *Nano Lett.* **2013**, *13*, 1245-1250.

(16) Stender, A. S.; Marchuk, K.; Liu, C.; Sander, S.; Meyer, M. W.; Smith, E. A.; Neupane, B.; Wang, G.; Li, J.; Cheng, J.-X.; Huang, B.; Fang, N. *Chem. Rev.* **2013**, *113*, 2469-2527.
(17) Ha, J. W.; Marchuk, K.; Fang, N. *Nano Lett.* **2012**, *12*, 4282-4288.

(18) Wang, G.; Sun, W.; Luo, Y.; Fang, N. *J. Am. Chem. Soc.* **2010**, *132*, 16417-16422.

(19) Gu, Y.; Sun, W.; Wang, G.; Fang, N. *J. Am. Chem. Soc.* **2011**, *133*, 5720-5723.

(20) Gu, Y.; Ha, J. W.; Augspurger, A. E.; Chen, K.; Zhu, S.; Fang, N. *Nanoscale* **2013**, *5*, 10753-10764.

(21) Nikoobakht, B.; El-Sayed, M. A. *Chem. Mater.* **2003**, *15*, 1957-1962.

(22) Gole, A.; Murphy, C. J. *Chem. Mater.* **2004**, *16*, 3633-3640.

(23) Jana, N. R.; Gearheart, L.; Murphy, C. J. *Chem. Commun.* **2001**, 617-618.

(24) Pietrobon, B.; McEachran, M.; Kitaev, V. *ACS Nano* **2008**, *3*, 21-26.

(25) Liu, M.; Guyot-Sionnest, P. *J. Phys. Chem. B* **2004**, *108*, 5882-5888.

(26) Xiang, Y.; Wu, X.; Liu, D.; Li, Z.; Chu, W.; Feng, L.; Zhang, K.; Zhou, W.; Xie, S. *Langmuir* **2008**, *24*, 3465-3470.

(27) Park, K.; Drummy, L. F.; Vaia, R. A. *J. Mater. Chem.* **2011**, *21*, 15608-15618.

(28) Jiang, R.; Chen, H.; Shao, L.; Li, Q.; Wang, J. *Adv. Mater.* **2012**, *24*, OP200-OP207.

(29) Hou, S.; Hu, X.; Wen, T.; Liu, W.; Wu, X. *Adv. Mater.* **2013**, *25*, 3857-3862.

(30) Zhu, J.; Zhang, F.; Li, J.-J.; Zhao, J.-W. *Gold Bull.* **2014**, *47*, 47-55.

(31) Damm, C.; Segets, D.; Yang, G.; Vieweg, B. F.; Spiecker, E.; Peukert, W. *Small* **2011**, *7*, 147-156.

(32) Cheng, X.; Zhang, W.; Ji, Y.; Meng, J.; Guo, H.; Liu, J.; Wu, X.; Xu, H. *RSC Adv.* **2013**, *3*, 2296-2305.

(33) Kobayashi, Y.; Katakami, H.; Mine, E.; Nagao, D.; Konno, M.; Liz-Marzán, L. M. *J. Colloid Interface Sci.* **2005**, *283*, 392-396.

(34) Sendroiu, I. E.; Warner, M. E.; Corn, R. M. *Langmuir* **2009**, *25*, 11282-11284.

(35) Mahanti, M.; Basak, D. *RSC Adv.* **2014**, *4*, 15466-15473.

(36) Aryal, S.; B.K.C, R.; Dharmaraj, N.; Bhattarai, N.; Kim, C. H.; Kim, H. Y. *Spectrochim. Acta A Mol. Biomol. Spectrosc.* **2006**, *63*, 160-163.

(37) Khalavka, Y.; Becker, J.; Sonnichsen, C. *J. Am. Chem. Soc.* **2009**, *131*, 1871-1875.

(38) Ha, J. W.; Sun, W.; Stender, A. S.; Fang, N. *J. Phys. Chem. C.* **2012**, *116*, 2766-2771.

(39) Ha, J. W.; Chen, K.; Fang, N. *Chem. Commun.* **2013**, *49*, 11038-11040.

Supporting Information

for

MULTISHELL Au/Ag/SiO_2 NANORODS WITH TUNABLE OPTICAL PROPERTIES AS SINGLE PARTICLE ORIENTATION AND ROTATIONAL TRACKING PROBES

Kuangcai Chen, Chia-Cheng Lin, Javier Vela, Ning Fang**

* To whom correspondence should be addressed.

Email: vela@iastate.edu; nfang@iastate.edu

Contents

Experimental Section

Nanorod synthesis and characterization

AuNRs were prepared according to a literature procedure with slight modification.[S1] The gold nanoparticle seeds were prepared first. Typically, 5 mL of 0.20 M CTAB (aq) (Sigma-Aldrich) was mixed with 50 μL of 0.02 M $HAuCl_4$ (aq) ($HAuCl_4 \cdot xH_2O$, 49 % Au, Strem Chemicals) followed by the addition of 0.3 mL of ice-cold 0.01 M $NaBH_4$ (aq) (Acros Organics). The seed solution was kept stirring for 2 h prior to injection into the growth solution. The growth solution was prepared by mixing 50 mL of 0.10 M CTAB (aq), 1.25 mL of 0.02 M of $HAuCl_4$ (aq), 0.32 mL of 0.01 M $AgNO_3$ (aq) (Strem Chemicals) and 0.36 mL of 0.10 M ascorbic acid (ACS grade, Alfa Aesar) aqueous solution in a sequential order. After the growth solution turned colorless, 60 μL of the seed solution was injected into the growth solution and kept static for 24 h at 30 °C. The Au/AgNRs (1.1×10^{11} nanoparticle/mL) were prepared according to a reported method.[S2-3] 4 mL of the gold nanorod solution was centrifuged and re-dispersed in 0.8 mL of 0.10 M CTAB followed by dilution to 4 mL with 1 wt % polyvinylpyrrolidone (PVP, M.W. 3,500, Acros Organics) aqueous solution. 24 μL of 0.01 M $AgNO_3$ (aq), 0.30 mL of 0.10 M ascorbic acid (aq) and 0.45 mL of 0.1 M NaOH (aq) (Fisher Scientific) were added in order and reacted for 2 h. For the thin silica coating, a reported two-step silica coating method was employed.[S4] To a 2 mL of the Au/AgNRs solution, 20 μL of 2 v/v % ethanolic 3-mercaptopropyl trimethoxysilane (MPTMS) (Gelest) solution was added, and the mixture was kept stirring for 45 min. 40 μL of 0.54 % sodium silicate ($Na_2O(SiO_2)x \cdot xH_2O$, 27 %, Sigma-Aldrich) solution was then added, and the solution was kept stirring for 4 days. Excess reactants were separated by centrifugation, and the

Au/Ag/SiO_2-NRs were re-dispersed in deionized water to a final concentration of 2.2×10^{11} nanoparticle/mL for further use.

Transmission Electron Microscopy (TEM) was measured on an FEI Tecnai G2 F20 field emission scanning transmission electron microscope at 200 kV (point-to-point resolution < 0.25 nm, line-to-line resolution < 0.10 nm). UV-Vis extinction spectra were collected with a photodiode-array Agilent 8453 UV−Vis spectrophotometer.

Synthetic lipid bilayer preparation and cell cultures

The phospholipid 1-palmitoyl-2-oleoyl-sn-glycero-3-phosphocholine (POPC, Avanti Polar Lipids) solution (20 μL, 25 mg/mL) in chloroform was gently dried by nitrogen and then vacuum dried at least 3 h at room temperature to remove the residual chloroform. The final POPC concentration was brought to 0.5 mg/mL by adding 1 mL phosphate buffered saline (1x PBS, pH 7.4). After rehydrating in PBS for 30 min with vortexing, cloudy multilamellar vesicles suspension solution was obtained. The suspension solution was extruded through a polycarbonate membrane (100 nm pore size, WHA110405, Sigma-Aldrich) at least 21 times to form the large unilamellar vesicles solution by a mini-extruder (Avanti Polar Lipids, Alabaster, AL). The resulting solution was kept at 4°C. After incubating the unilamellar vesicle solution in a chamber, made by a cleaned glass slide, two double-sided tapes and a cleaned 22 mm × 22 mm No. 1 glass coverslip (Corning, NY), for 10 min, the planar bilayer was formed. Then the excess lipids were washed by PBS. 5 μL of the original Au/Ag/SiO_2-NRs solution was added on one side while a piece of filter paper was applied on the other side of the chamber to help the nanoparticles to diffuse and disperse onto lipid bilayers.

A549 human lung cancer cells (ATCC, CCL-185) were cultured on glass coverslips in Petri dishes with F-12K Medium (Kaighn's Modification of Ham's F-12 Medium, ATCC, 30-2004) supplemented with 10 % fetal bovine serum. The cell culture was incubated at 37°C under 5 % CO_2 to an appropriate confluence. Before imaging, the coverslip with cells was rinsed with PBS and formed a chamber with two pieces of double-sided tape and glass slide. Au/Ag/SiO_2-NRs solution was centrifuged and resuspended in PBS to the same concentration before adding into chamber. The same procedure was used as for lipid bilayer study and filter paper was used to facilitate the dispersion of nanoparticles onto cell membranes.

Imaging system

An upright Nikon Eclipse 80i microscope was used in this study. The DIC mode used a pair of 100×II-R Nomarski prisms, a 100× Plan Apo/1.40 oil-immersion objective, a NA 1.40 oil condenser and a halogen lamp as light source with maximum output power of 100 Watts. Appropriate filters were inserted in the light path. In order to facilitate single particle characterization and to minimize inter-particle SPR coupling, the original Au/Ag/SiO_2-NRs solution (2.2×10^{11} nanoparticle/mL) was diluted 3 times in deionized water, and then 6 μL of the diluted solution was added onto a glass slide to control the nanoparticle concentration to 1 μm^{-2}. The images and movies were taken by a Hamamatsu ORCA-Flash 2.8 CMOS camera and analyzed using MATLAB and NIH ImageJ.

Supporting Figures

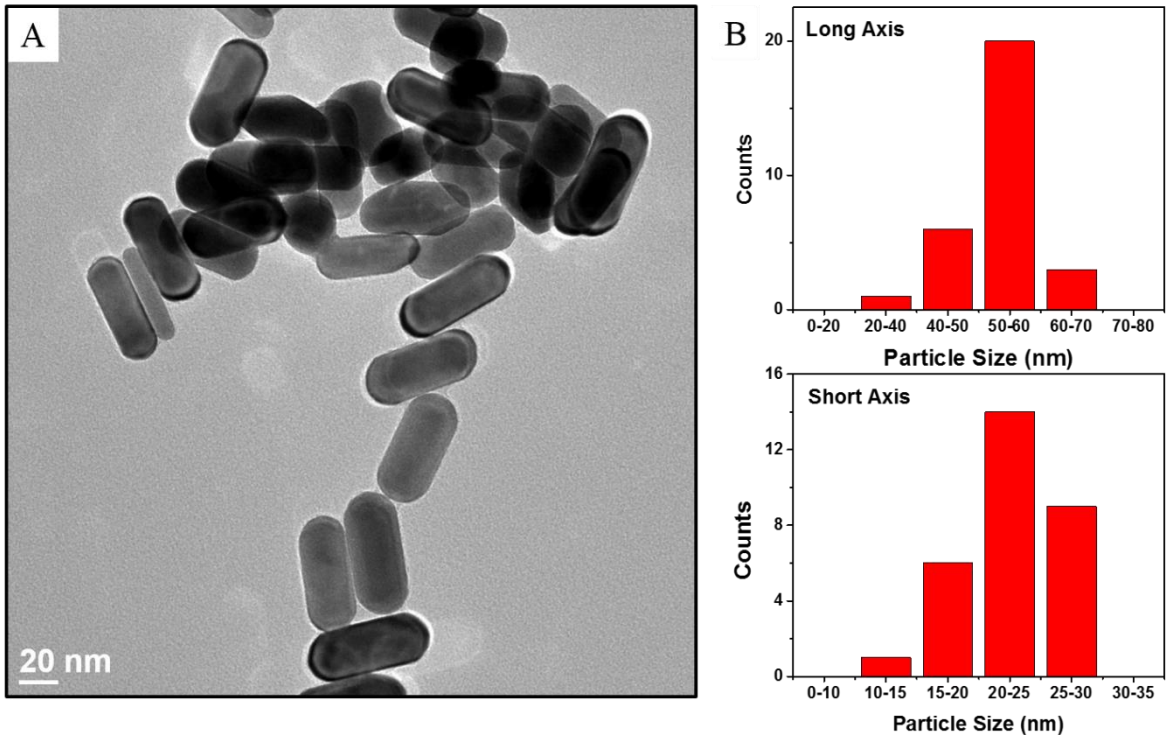

Figure S1. TEM image of (A) AuNRs and (B) the size distributions based on TEM images.

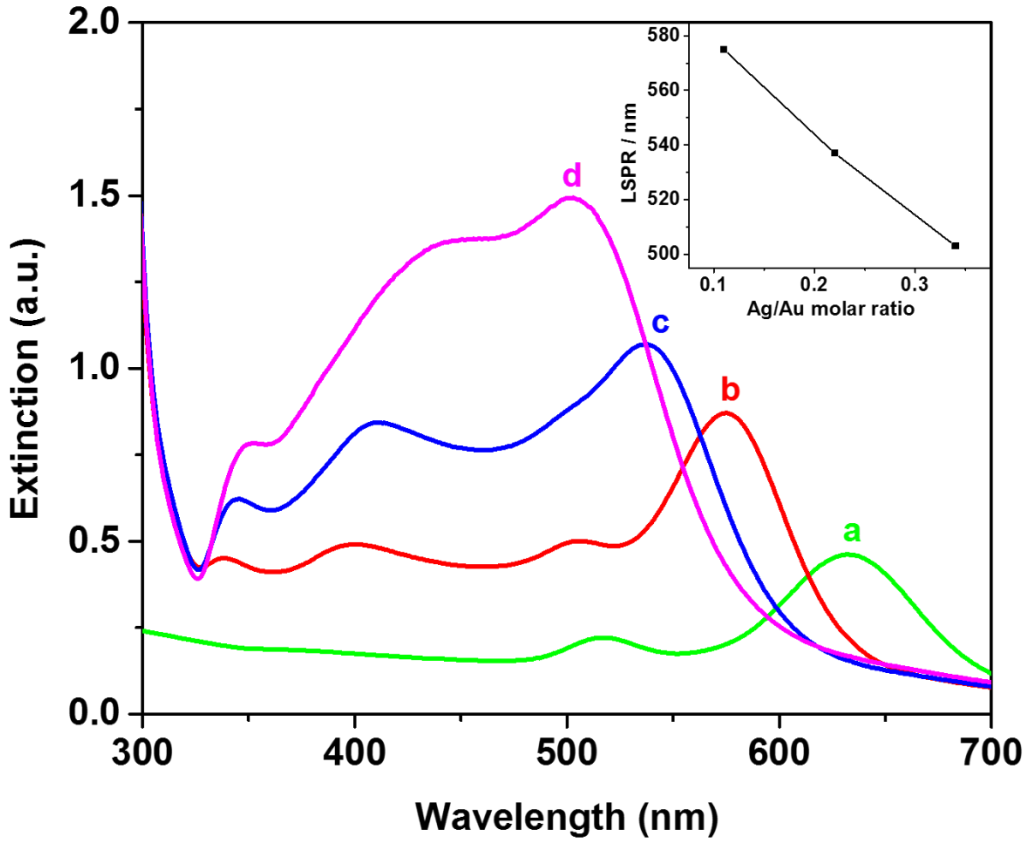

Figure S2. UV-Vis extinction spectra of synthesized nanoparticles. (a) AuNRs and the Au/Ag core-shell nanoparticles with Ag/Au molar ratios of (b) 0.11, (c) 0.22, (d) 0.34. As shown in the inserted figure, the longitudinal LSPR of AuNRs shifted from 632 nm to 563 nm, 537 nm and 503 nm after the addition of silver layer.

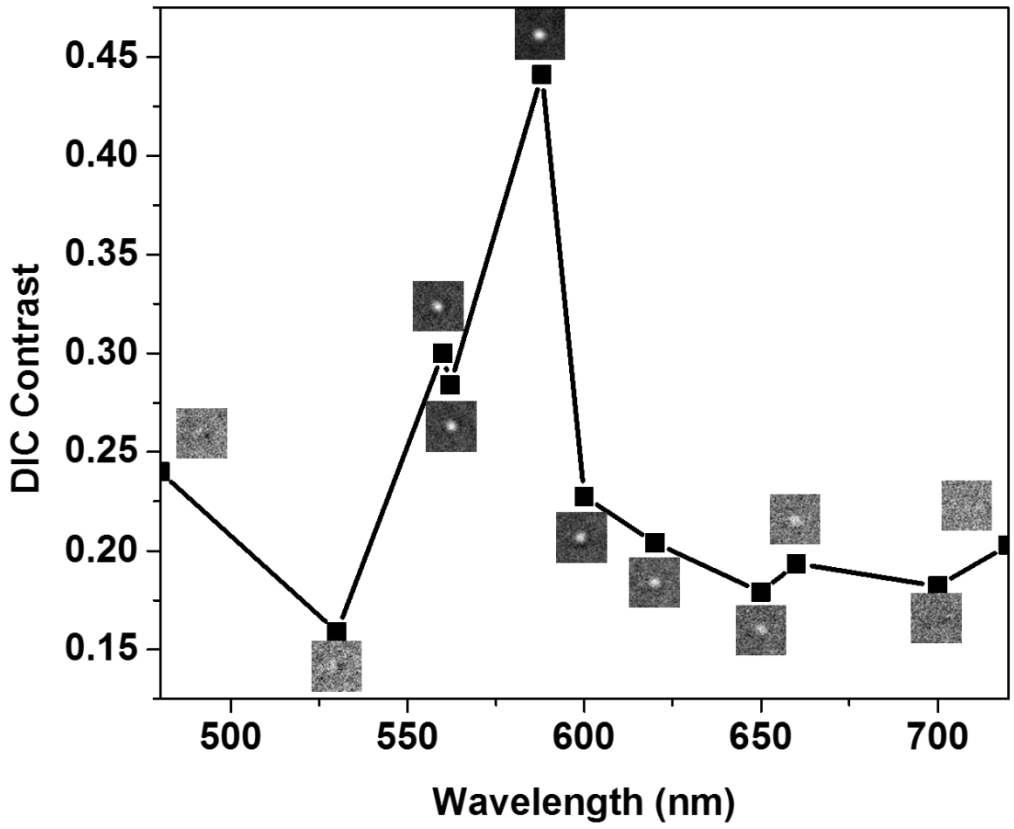

Figure S3. DIC contrast spectrum of an immobilized, randomly oriented Au/Ag/SiO_2-NR on a glass slide. Data points were determined by the availability of band pass filters. Each DIC image corresponding to the closest data point in the plot and the image contrast are normalized to their local maximum and minimum intensities. The edge length of each square is 1.45 µm.

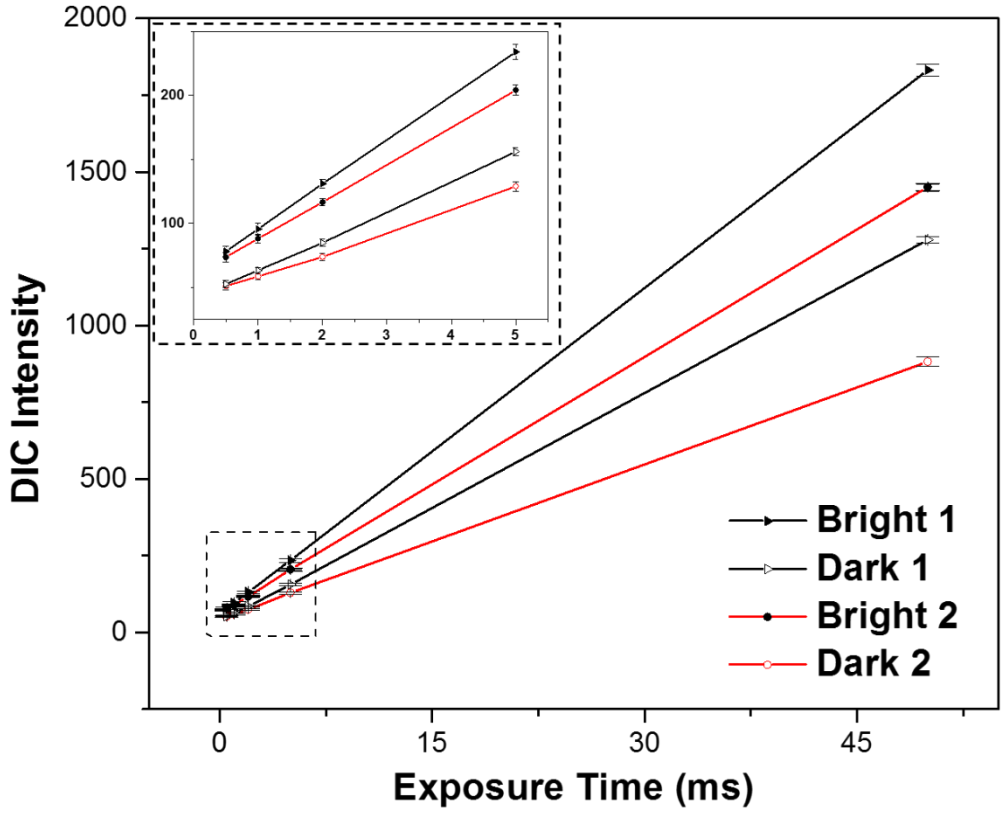

Figure S4. DIC intensity changes upon changing the exposure time. Bright 1 and Dark 1 correspond to the nanoparticle on the left in movie S1 and Bright 2 and Dark 2 are for the nanoparticle on the right. The inset is a zoom in of the squared area on the low exposure part of the main plot, magnified for better clarity.

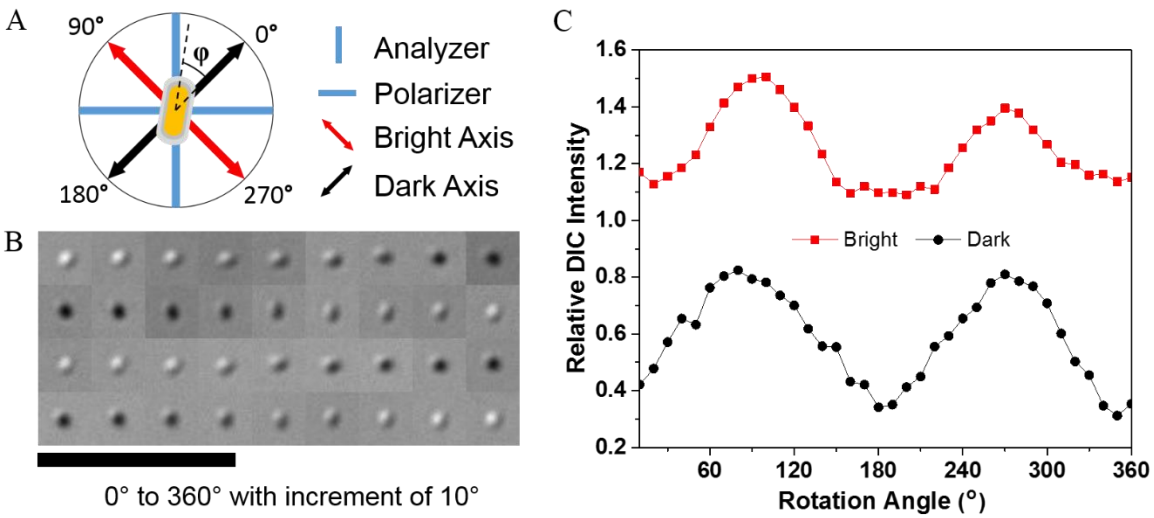

Figure S5. 360° rotation of Au/Ag/SiO_2-NR immobilized on a glass slide. (A) Definition of orientation angle φ with respect to the polarizer and analyzer positions in Nikon Eclipse 80i microscope setup. (B) 36 DIC images of Au/Ag/SiO_2-NR during 360° rotation from 0° to 360° with an interval of 10°. Scale bar is 5 μm. (C) Relative DIC intensity traces of the bright and dark signals in (B).

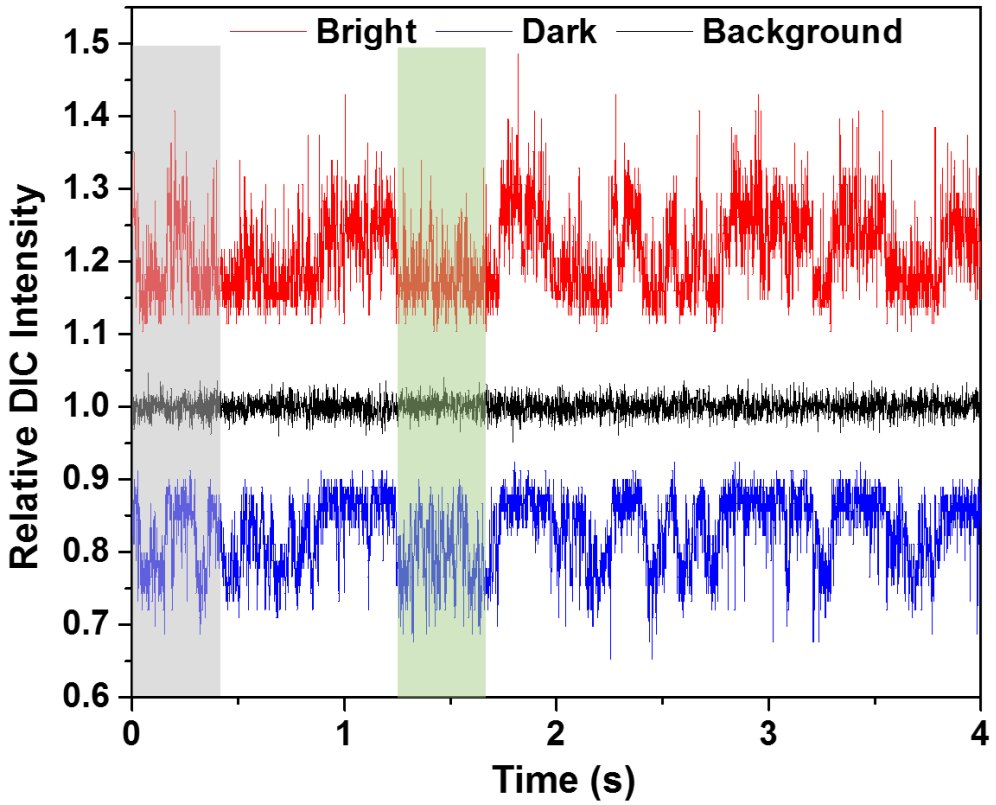

Figure S6. Relative DIC intensity traces of Au/Ag/SiO_2-NR rotating on synthetic lipid bilayer surface and recorded at 1 ms temporal resolution for 4000 frames.

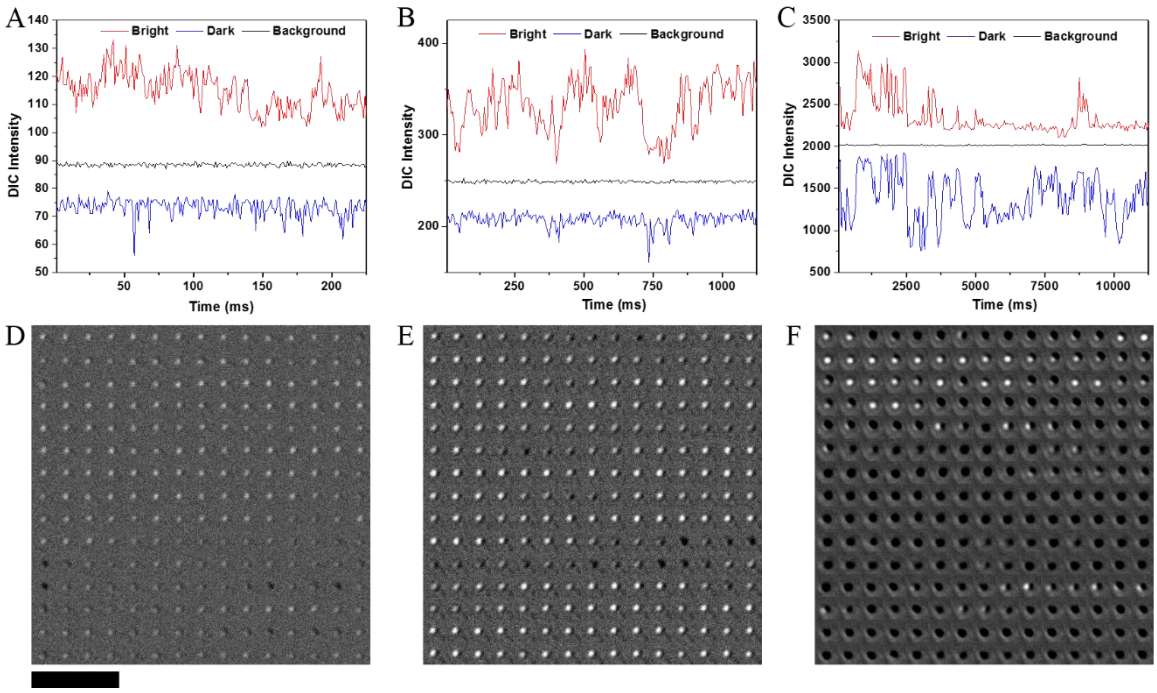

Figure S7. DIC intensity traces of Au/Ag/SiO_2-NRs rotating on cell membrane and recorded at (A) 1 ms, (B) 5 ms, and (C) 50 ms and their corresponding consecutive DIC images (D), (E) and (F). Scale bar is 5 μm.

Movie S1. Recorded DIC images of two Au/Ag/SiO_2-NRs immobilized on glass slides at different exposure times, and played at 30 fps. Scale bar is 2 μm.

Downloading Link:

http://pubs.acs.org/doi/suppl/10.1021/acs.analchem.5b00604/suppl_file/ac5b00604_si_002.avi

Table S1. Relative bright and dark intensity measurement errors of the both Au/Ag/SiO_2-NRs in movie S1. Bright 1 and Dark 1 corresponding to the nanoparticle on the left in movie S1 and Bright 2 and Dark 2 are for the particle on the right.

Relative Errors	Exposure Time (ms)				
	0.5	1	2	5	50
Bright 1	5.20%	4.72%	2.73%	2.51%	1.10%
Dark 1	5.44%	3.43%	3.32%	1.97%	0.89%
Bright 2	5.12%	3.75%	2.30%	2.02%	0.79%
Dark 2	5.51%	3.92%	3.73%	2.84%	1.74%

Supporting References

(S1) Nikoobakht, B.; El-Sayed, M. A. *Chem. Mater.* **2003,** *15*, 1957-1962.

(S2) Liu, M.; Guyot-Sionnest, P. *J. Phys. Chem. B* **2004,** *108*, 5882-5888.

(S3) Khalavka, Y.; Becker, J.; Sonnichsen, C. *J. Am. Chem. Soc.* **2009,** *131*, 1871-1875.

(S4) Sendroiu, I. E.; Warner, M. E.; Corn, R. M. *Langmuir* **2009,** *25*, 11282-11284.

CHAPTER 3

FIVE-DIMENSIONAL TRACKING OF CARGO IN LIVE CELLS

Abstract

A novel single particle tracking (SPT) technique has been developed to visualize the intracellular transport of cargos in five dimensions (5D): the three spatial coordinates (x, y, z) and two orientation angles (azimuthal angle φ and elevation angle θ) of a probe's transition dipole over a series of time steps. Tracking rotational probes, such as gold nanorods, in the *z*-axis is challenging because translational motions in the *z*-axis can be easily confused with rotational motions as both types of motion result in similar changes in signal intensity. The 5D-SPT method overcomes this long-standing challenge by utilizing the concept of parallax to sense the axial movement of the target object and employs an automatic feedback loop algorithm to control the objective's focal plane and bring the target object back to focus repetitively. In such an implementation, the target object is kept in focus to provide the highest possible S/N for 2D localization and orientation determination, while the *z* positions are recorded from the vertical movement of a high-precision objective scanner. Through the live-cell SPT experiments, we demonstrate that the 5D-SPT technique has potential to significantly improve the capacity to study the intracellular transport of cargos in a cellular environment.

Introduction

Single particle tracking (SPT) has become an indispensable approach in our attempts to understand the detailed working mechanisms of biomolecules in complex cellular environments.[1] Motions of single imaging probes recorded in SPT experiments contain rich

information in multiple dimensions, including the x, y, z coordinates and the two orientation angles (azimuthal angle φ and elevation angle θ , as defined in **Figure 1**) of the probe's transition dipole over a series of time steps. It has been highly challenging to acquire accurate measurements in all of these five dimensions (5D: x, y, z, φ, θ) simultaneously.

The challenges are mainly three-fold: (i) It is difficult to resolve the dipole orientation of single fluorescent probes in a cellular environment at reasonably fast temporal resolution due to the well-known limitations, such as high background and fast photobleaching; (ii) Even though lateral super-localization of single fluorescent molecules with nanometer accuracy[2-4] in the (x, y) plane has become routine, high-accuracy tracking in the axial (z) direction is still considerably more difficult. Many strategies have been developed in the past decade to improve the z-tracking ability, including multifocal plane microscopy,[5-7] defocused imaging,[8-10] double-helix point spread function microscopy,[11,12] scanning-angle total internal reflection fluorescence microscopy,[13-15] astigmatism imaging,[16,17] and parallax-based imaging.[18,19] However, an improvement in axial localization often accompanies a reduced accuracy in lateral localization because the movement in the z axis leads to out-of-focus images with much reduced signal to noise ratios (S/N). (iii) Translational motions in the z axis can be easily confused with rotational motions as both types of motion result in similar changes in signal intensity.

The first challenge can be circumvented by using anisotropic plasmonic gold nanorods as alternative rotational probes. The exceptionally high absorption and scattering cross-sections of gold nanorods result in strong and stable signals at the localized surface plasmon resonance (LSPR) wavelengths. We have previously developed the single particle orientation and rotational tracking (SPORT) technique for direct visualization of rotational

dynamics of gold nanorods in differential interference contrast (DIC) microscopy at millisecond temporal resolution, while still obtaining high-contrast images of cellular features.[20-23] Relatively low illumination light intensity from a typical halogen lamp, instead of a stronger laser light source,[24] brings minimal disruptions to cell functions, making it particularly suitable for long-term SPT experiments in live cells. Several modifications of the DIC microscope have also been reported to adapt the SPORT technique for dual-modality (fluorescence and DIC) imaging[25] and simultaneous 2D localization and rotational tracking.[26]

The current report introduces the first high-speed 5D-SPT method to overcome both the second and third challenges. The core idea is to combine the DIC microscopy-based SPORT technique with the principle of parallax microscopy[18,19] for simultaneous spatial and rotational tracking. In parallax microscopy, either a prism[18] or a set of mirrors[19] is inserted into the emission light path to split the light evenly into two paths of slightly different angles (similar to two eyes of a human being with slight different viewing angles to generate the depth perception), and therefore, two spots are produced on the camera for a single imaging probe. This strategy converts a probe's movement in the z direction into lateral movement of the two spots.

The new 5D-SPT method uses parallax to sense the axial movement of the target object and employs an automatic feedback loop algorithm to control the objective's focal plane and bring the target object back to focus repetitively. In such an implementation, the target object is kept in focus to provide the highest possible S/N for high-accuracy 2D localization and orientation determination, while the z positions are recorded as the vertical positions of the high-precision objective scanner.

To demonstrate the power of the 5D-SPT method, we study the intracellular transport of cargos in live cells. The cytoskeleton is a complex organization composed of interweaving microtubules and actin filaments. Motor proteins including kinesins, dyneins and myosins carry cargos along the cytoskeleton tracks. After several decades of intensive studies dominated by *in vitro* assays,[27-30] direct visualization of cargo transport in live cells has become a much more important approach to understand the transport mechanisms in a cellular environment.[22,25,31-33] The importance of live-cell experiments was further demonstrated recently in a finding that the crowded cellular environment significantly impacts the motor-driven motility of early endosomes.[34] Live-cell intracellular transport studies can be greatly benefited from this and other recently developed optical imaging techniques. The original SPORT techniques have been employed to visualize the transport of nanorod-containing vesicles,[22,25] however, the vertical information was missing in those studies. Lakadamyali *et al.* reported the track-switching of lysosomes on the microtubules whose 3D structures were resolved in 3D stochastic optical reconstruction microscopy (3D STORM);[35] however, the lysosomes were only tracked in 2D while no rotational information could be obtained. Using the 5D-SPT technique reported here, it becomes possible to reveal much more detailed motions of cargos and their transport trajectories.

Results and Discussion

Design of parallax-DIC microscopy

Parallax is realized on an upright DIC microscope by inserting a wedge prism at the objective's back focal plane (**Figure 2A**). Half of the light that has passed through the sample maintains the original path, while the other half of the light is deviated slightly by the wedge

prism. Two images of the same sample are formed in the upper and lower halves of the sensor area. These images will be referred to as "half-plane" images in the rest of the discussion because each image utilizes half of the numerical aperture of the objective, while conventional microscopy images utilizing the full numerical aperture will be referred to as "full-plane" images.

The movement of a target object, e.g., a lipid vesicle or a gold nanorod, in the axial (z) direction is resolved by monitoring the distance *d* between the pair of half-plane images of the same object. For any object in the focal plane, the distance between its two half-plane images (d_0) is a fixed value determined by the angle between the wedge prism's surfaces. When the target object moves upwards ($\Delta z > 0$) towards the objective, the two half-plane images move away from one another to increase *d*. When the target object moves downwards ($\Delta z < 0$) away from the objective, the two images move toward one another to shorten *d*.

Movie 1 shows parallax-DIC images of a stationary gold nanorod at three orientations traveling smoothly from -0.4 μm below the focal plane to +0.4 μm above the focal plane at a speed of 100 nm per second with a single frame exposure time of 200 ms. The nanorod shows orientation-dependent DIC images (**Figure 2B**).

The parallax-DIC microscope inherits the advantages of conventional DIC microscopes for single cell studies, including the ability of visualizing the cell morphology and detailed intracellular structures while tracking the plasmonic nanoprobes. **Figure S1** shows the two half-plane cell images change from partial overlap to complete separation during a vertical scan. The overlapped region should be avoided in picking target objects to ensure high reliability and sensitivity in the 5D-SPT experiments.

Localization in parallax-DIC microscopy

In parallax-DIC microscopy, a target object's movement in the axial direction will cause its two half-plane images to move an identical distance in the opposite directions. However, the middle point of the line connecting the centers of the pair of images will remain unchanged unless the target object undergoes lateral movement. Therefore, localization in the (x, y) plane can be translated into a problem of finding this middle point through high-accuracy localization of the pair of half-plane images.

Gaussian fitting, the most widely used localization method, is not suitable for superlocalization in DIC microscopy because the anti-symmetric DIC point spread function (PSF), which consists of apposed bright and dark portions over a gray background, cannot be fitted with a simple mathematical function. Therefore, the more complicated model-based correlation mapping procedures are required for localizing particle probes in DIC microscopy.[27,36] Localization in parallax-DIC microscopy is even more challenging as the half-plane PSF appears to be stretched in the direction perpendicular to the split plane (**Figure S2**).

To overcome the complications in the parallax-DIC PSF, we have implemented a redesigned correlation mapping procedure, in which one of the half-plane images is used as the model to map the other image in order to find the centers of these two images and then the middle point. With the wedge prism splitting the light in half, the two resulting half-plane PSFs are distorted in the way that one appears to be the mirror image of the other. The correlation maps of the two half-plane images with correlation scores above a set threshold (typically 0.4 - 0.6) are weighed to find their relative coordinates. The distance between the two images and the position of the middle point are thus determined.

The axial position of a target object is determined from the distance between the two half-plane images. The axial localization is calibrated by scanning the focal plane of the objective vertically in 20 nm steps through the stationary gold nanorods and correlating the distance between the two images with the axial position of the sample. Each data point on the calibration curve (**Figure 2C**) is the average distance between the two half-plane images as the nanorod is rotated 180° in 5° intervals. The distance between the two images falls in a linear relationship with the axial position of the gold nanorod when the vertical displacement is within the displayed range of -0.5 μm to +0.5 μm relative to the focal plane. For the current setup, the calibration curve returns a slope of +0.626 ($d/\Delta z$). The precision measurements of the 3D localization yield standard deviations of 11 nm, 14 nm and 17 nm in the x, y, and z axes, respectively (**Figure 2D-F**).

It should be noted that the two half-plane images are not identical. The image formed through the wedge prism is slightly longer along the direction perpendicular to the split plane than the other image formed in the original light path of the microscope. Furthermore, it is challenging to place the wedge prism at the perfect position to split the light exactly in half, which results in small variances in the relative intensities between the two half-plane images. Nonetheless, the subtle differences in image intensity and shape do not significantly affect the accuracy of the correlation mapping procedure, as shown in **Figure 2C** that the distances between the two half-plane images are remarkably consistent for the entire angle range of 0-180°. Using a set of mirrors instead of a wedge prism has been demonstrated to be more flexible and precise to achieve parallax in fluorescence microscopy;[19] however, the presence of two Nomarski prisms makes the mirror-based design much more difficult to realize on a commercial DIC microscope.

A common concern of the high-accuracy localization of a transition dipole is associated with the asymmetric emission/scattering intensity distribution when the dipole is titled relative to the horizontal plane.[37,38] As a result, the Gaussian fitted image center may not overlap with the actual geometric center of the probe. It is important to note that this type of localization error (on the order of a few tens of nanometers) is critical for the localization of stationary imaging probes where nanometer precision is often required.[39] However, for the dynamic SPT experiments where nearly everything is moving constantly, these small localization errors can be neglected without noticeably affecting the recorded 3D trajectories.

Auto-focusing system for simultaneous 3D localization and rotational tracking

The azimuthal angle φ is defined with respect to the dark polarization direction in the DIC microscope, which implies the brightest image at 90° and the darkest image at 0°. When a gold nanorod is rotated from 0-180°, the in-focus half-plane DIC images display periodic pattern and intensity changes (**Figure S3**) similar to those in conventional DIC microscopy,[20] even though the half-plane DIC images are elongated compared with the full-plane DIC images. Therefore, the relative DIC intensities of the bright part and the dark part can still be used to calculate the orientation angles (φ, θ) of the gold nanorod as reported in our previous work.[20]

Defocusing not only results in lower signal intensities but also causes wavefront phase disturbances that lead to changes in the DIC image patterns, and therefore, it can negatively impact the accuracy in both localization and orientation determination. Our solution to this problem is to keep the target gold nanorod in focus throughout the entire trajectory. An automatic feedback focusing system has therefore been developed as a plugin

for μManager[40,41] for the parallax-DIC microscope so that the high-precision objective scanner can move the focal plane of the objective to compensate for the vertical movement of the target object detected from the distance between the two half-plane images. At the same time, the tracking program outputs the distance the objective scanner travels in each feedback loop, allowing the relative vertical positions from the initial position of the nanorod to be recorded in real time.

The performance of auto-focusing was first evaluated by the auto-focusing feedback capacity with respect to the stage movements. The microscope sample stage was coupled to a motorized rotation stage through the microscope fine adjustment knob. With the auto-focusing tracking program on, the objective scanner moved accordingly depend on the stage movement. The z axial position of the objective scanner increased to compensate the z axial displacement to keep the target nanoparticle in focus when the stage was moved down by motorized rotation stage. In contrast, the z axial position of the objective scanner decreased when the stage moved up. In this situation, objective position was also automatically adjusted by the tracking program to make up the z axial change and the nanoparticle of interest stayed in focus. **Figure S4** shows the response of objective scanner when the stage was moved toward different directions with different speed. The immobilized gold nanorod sample was first found by manual adjusting to a relatively clear image, and then the auto-focusing tracking was initiated to target a specific nanoparticle. When the sample stages was moved at 500 and 1000 steps per second (0.35 and 0.70 μm/s) toward both directions, the auto-focusing feedback was fast enough to adjust the objective scanner accordingly as indicated from the perfect linear fitting in the figure. The slopes were 0.078 and 0.1489 when the sample stage was moved down with respect to objective. And the slopes were -0.074 and -

0.1462 when it was moved upward. The coefficient of determination (R^2) of these fittings were all larger than 0.99. The response of the auto-focusing tracking speed toward 0.70 μm/s z axial movement speed is far than enough to track most of the cellular processes. Also, the z axial tracking range is not restricted by the depth of field of the objective (several μm) but rather is limited by the travel distance of the objective scanner (100 μm). This enables z tracking throughout the entire thickness of any kinds of mammalian cells.

The robustness of the auto-focusing scheme was further demonstrated by tracking lipid vesicles in live cells. These vesicles are generally spherical and exhibit nearly constant DIC intensities and image patterns when they are in focus. **Figure S5** and **Movie 2** show such an example in a live A549 human lung cancer cell. The total vertical movement range is up to ~200 nm as shown in the 3D trajectory. The relative bright and dark DIC intensities and the contrast of the vesicle remained nearly constant regardless of the vertical movement. The response delay of the objective scanner used in the current setup has limited the temporal resolution to 50 ms. On average, the position of the objective scanner is adjusted every 100 ms (or 2 frames). The objective scanner keeps dragging the target object back to focus as long as it does not move too fast vertically.

5D tracking of gold nanorod-containing vesicles in live cells

The 5D-SPT technique enables us to reveal much detailed motions of early endosomes in live cells. We have demonstrated previously that gold nanorods are excellent reporters of translational and rotational motions of early endosomes.[22] A similar strategy was applied in the present study.

Gold nanorods with average dimensions of 40 nm width by 80 nm length were surface-modified with transferrin, an iron-binding blood plasma glycoprotein with specific receptors in the cell membrane,[42] which can promote the clathrin-mediated endocytosis pathway.[43] Within the first 45 min following the cellular uptake, the endocytosed substances mostly reside in early endosomes that are about 50-100 nm in diameter.[44,45] As discussed extensively in our previous publication,[22] the transferrin-modified gold nanorods are bound to the membrane receptors and tightly wrapped by the vesicle membranes. These nanorods generally lose the independent rotational freedoms relative to the vesicles; therefore, they can be used as rotational reporters of early endosomes being transported by kinesin and dynein motors.

In the present study, we recorded the motions of nanorod-containing vesicles in living A549 human lung cancer cells under the parallax-DIC microscope. An example of the lateral and vertical displacements along with the DIC intensities of a gold nanorod is shown in **Figure 3 and Movie 3**. The random but confined rotational motions of the cargo within the first second likely reflect the process of the cargo searching for a cytoskeleton track. Starting at ~1.0 s, the cargo moves nearly straight along the *z*-axis and returns at 2.1 s, suggesting a possible back-and-forth movement along a track that is perpendicular to the image plane. Then the cargo makes a big turn during a pause lasting from 2.1-2.9 s, followed by lateral movement of more than 5 μm in the last 2 s of the recording. The big turn is likely due to the cargo switching from the perpendicular track to a horizontal one. The cargo also undergoes a fast reversal (going back and forth) at 3.0 s, while the rotational behaviors of the nanorod can be observed, possibly because of the rearrangement of motors during which the tension on the cargo is weakened.[22] These observations combine to render a complete process of cargo

transport inside a living cell with great details: cargo searching for a track, directional transport, track-switching, and pauses. Two additional examples are shown in **Figure S6 and S7 (Movies 4 and 5)**.

An interesting sequence of movement is observed at 3.6-5.0 s in **Figure 3**, when the cargo changes its moving direction laterally and vertically, accompanied by changes in its orientation. The vertical displacements are in the range of 100-160 nm, in good agreement with the span of the 80 nm long gold nanorod when it tumbles around a microtubule track of ~25 nm in diameter. Combined with the moving trajectory shown in **Figure 3B**, it suggests that the cargo moves along the microtubule track with a twisted up-and-down motion. This phenomenon may be ascribed to microtubule bending (a curved conformation of the tubulin dimers).[46,47] Another possible cause is the steric hindrance induced by the crowded cellular environment: the cargo may navigate around a big obstacle or the microtubule may be forced to change its shape.

Conclusions

In summary, a parallax-DIC microscope and accompanying tracking program have been developed to realize automatic 5D-SPT in live cells. The axial movement of gold nanorod probe is detected by monitoring the distance between two half-plane images generated with a wedge prism. A vertical precision of 17 nm has been achieved.

As demonstrated through the live-cell SPT experiments, the 3D trajectories and DIC intensities incorporating rotational information of gold nanorod-containing vesicles can be correlated to elucidate the intracellular transport events in unprecedented detail, which makes the 5D-SPT technique a promising tool to shed new light on the working mechanisms of molecular motors in live cells.

A unique trait of the 5D-SPT technique is that the recorded moving traces reflect the 3D organization of the cytoskeleton tracks inside the cell. Although the current setup does not allow the visualization of the 3D structures of the cytoskeleton, it is promising that the 5D tracking of intracellular transport can be combined with super-resolution imaging of cytoskeleton structures[35] so that the transport mechanism of cargos can be better elucidated. Another critical step in the future is to combine the 5D-SPT of plasmonic nanoparticle probes with the fluorescence imaging of associated proteins, such as tau[48-50] and dynactin[51], to understand the regulated intracellular transport at the molecular level.

Experimental Section

Parallax DIC microscopy

The Nikon Eclipse 80i upright microscope used in the present study was equipped with a set of Nomarski optics (including two Nomarski prisms, two polarizers, and a quarter-wave plate), an oil immersion condenser with a numerical aperture (NA) of 1.40, a 100× Plan Apo/1.40 oil immersion objective, and a Hamamatsu Scientific CMOS ORCA-Flash 2.8 camera. A 650 nm (± 13 nm) bandpass filter (Semrock, Rochester, NY) was inserted into the light path. A wedge prism (0.5° wedge angle deviation, Edmund, Barrington, NJ) was placed at the objective's back focal plane, which is at the filter insert position right above the objective and the second Nomarski prism of the DIC microscope. The position of the wedge prism was carefully adjusted to split the light in half. The two resulting half-plane images should be of similar intensities and share the same *x* coordinates.

Correlation mapping and calibration of z-localization

Gold nanorods with average dimensions of 40 nm width by 80 nm length were purchased from Nanopartz (Loveland, CO). They were washed twice with 18.2 mΩ Milli-Q water and diluted to ~5×10^8 particles/mL. The diluted solution was sonicated for 15 min at room temperature and then added onto a pre-cleaned glass coverslip. The particles were adsorbed onto the coverslip via electrostatic interactions. The coverslip was then sealed with clear nail polish to prevent evaporation.

An objective scanner was installed on the microscope, mounted with the 100× Plan Apo/1.40 oil immersion objective, and connected with a Piezo position servo controller (Physik Instrumente, Model E-710). Movies of the vertical scans of the fixed gold nanorods were taken while the camera and the objective scanner were synchronized at 200 ms per frame and per step of movement. The step size of the vertical scan was 20 nm.

The z-position of the gold nanorods was calibrated against the distance between the two half-plane DIC images of a single gold nanorod. The distance between the two DIC images was measured using the correlation mapping method. At each z-position, one of the half-plane images was used as the model to map both of the two images. The model image was cropped and overlaid with the region of interest (ROI) that includes both images, and moved pixel by pixel and line by line to cover the entire ROI. At each position, a correlation score in the form of Pearson's correlation coefficient was calculated as

$$p(\text{model},\text{sub-ROI}) = \frac{1}{m-1}\sum_{i=1}^{m}\frac{\left[I_{\text{model}}(i)-I_{\text{model}}(avg)\right]}{\sigma_{\text{model}}}\frac{\left[I_{\text{sub-ROI}}(i)-I_{\text{sub-ROI}}(avg)\right]}{\sigma_{\text{sub-ROI}}},$$

where the summation covers all the pixels in the model or the sub-ROI, m is the total number of pixels in the model, I is intensity, avg and σ denote the average and standard deviation of the intensity in the model or the sub-ROI, respectively. By weighing the p values above a

threshold of the region that the image of the particle covers, the center of the particle can be determined as

$$X_{\text{center}} = \frac{\sum_{i=1}^{m} X_i \left(p_i - threshold \right)}{\sum_{i=1}^{m} \left(p_i - threshold \right)},$$

where X denotes either x or y in the calculation, and the threshold is applied to cut off the background noise. The center coordinates of the two nanorod images, (x_1, y_1) and (x_2, y_2) are thus determined. For the highest possible accuracy, the prism inserted into the light path of the microscope should be well aligned so that the two images were not shifted horizontally. The distance between the two images is:

$$d = |y_2 - y_1|.$$

The calibration curve of the distance *d* as a function of *z* is thus obtained from the vertical scans where each data point is the average value obtained from the gold nanorod placed at 36 orientations (0-180° with 5° intervals). The calibration data (Fig. 2) results in a good linear fitting going through (0, 0), which refers to the vertical position of the nanorod in focus.

Both correlation mapping and calibration of z-localization were compiled as μmanager plugin in the auto-focusing tracking program. So movies (in TIFF) of the tracking, (x, y, z) relative spatial localization, and DIC bright and dark intensity traces were generated by the tracking program.

Computer simulation of full-plane and half-plane DIC images

Computer simulation of the full-plane and half-plane PSFs of a gold nanorod was adapted from the simulation of the Parallax images of a point source.[19] The simulation is based on the

simplified model that assumes the incident light from a point emitter produces a band-limited version of Fourier transform of a delta function in the back aperture of the objective. In this model, the amplitude and phase of the function keeps constant inside the circular sub-region, while jump to zero outside. The wavefront phase disturbance due to the defocusing of the gold nanorod ΔZ is in the form of

$$2\pi r^2 \Delta Z / [\lambda f (f + \Delta Z)],$$

where λ is the wavelength, f is the focal length, and r is the radial distance from the optical axis. The wavefront phase disturbance is then added to the Fourier transform. The sum, which represents the phase component, is combined with a constant amplitude component to generate an approximation to the defocus-aberrated pupil function at the back aperture of the objective for the full-plane image. For the half-plane image, the transform was set to zero in the negative y half-plane. The square of the modulus of the Fourier transforms of these distributions yields the model PSF distributions of the simulated scattering image pattern.

The lateral scale for the simulated PSFs is defined by assigning the radius at the first minimum of the in-focus PSF a value of

$$\frac{r}{\lambda} = 0.61 / \left(\text{effective NA}\right).$$

The axial scale is defined by assigning the magnitude of defocus at the first axial minimum of the PSF a value of

$$\frac{\Delta Z}{\lambda} = 2 / (n \sin^2 \alpha).$$

where n is the refractive index of the medium surrounding the point object, and α is the objective lens acceptance half-angle.

The DIC images are then generated by integrating the scattering amplitude PSF into the DIC PSF[52]:

$$h(x,y) = (1-R)\exp(-j\Delta\theta)k(x-\Delta x, y-\Delta y) - R\exp(j\Delta\theta)k(x+\Delta x, y+\Delta y),$$

where $2\Delta x$ and $2\Delta y$ are the shear introduced by the Nomarski prism along the x and y axes respectively, $2\Delta\theta$ is the bias retardation, where R determines the relative amplitude of the two wavefronts, and k(x, y) is the amplitude PSF for the optics under coherent illumination. All the simulation figures were generated by using MATLAB.

Surface modification of gold naonrods

The purchased gold nanorods (40 nm × 80 nm) were stabilized in cetyltrimethylammonium bromide (CTAB) solution. Before used in our experiments, the gold nanorods were centrifuged and resuspended in Millli-Q water twice to remove most of the CTAB. The gold nanorods were then surface modified with transferrin through a PEG linker by following the procedure described below: 1 mL of the gold nanorod solution reacted with 20-mM N-hydroxylsuccinimide (NHS)-polyethylene glycol (PEG)-thiol (Sigma-Aldrich, St. Louis, MO) for 1.5 hrs. After that, the gold nanorod colloidal solution was centrifuged and resuspended in 18.2 Ω Millli-Q water again to remove excess NHS-PEG-thiol. 20 µL of 2 $mg \cdot ml^{-1}$ transferrin in phosphate buffer saline (pH 7.4) was added to the gold nanorod solution and let react for 3 hrs. The gold nanorods were then centrifuged and resuspended in Millli-Q water before use. The concentration of the gold nanorod solution was 9×10^{10} nanoparticles/mL.

Cell culture

A549 human lung cancer cells (ATCC, CCL-185) were cultured on 22 mm × 22 mm poly-lysine coated glass coverslips in 35-mm petri dishes. Minimum essential cell culture medium (ATCC) supplemented with 10% fetal bovine serum supplement was added to the plates. The cell culture was incubated at 37°C under 5% CO_2. After the cell culture covered 70% of a coverslip, 40 μL of the transferrin modified gold nanorod solution (2.62×10^{10} particles/mL) was added to the cell culture and incubated for 45 min at 37°C under 5% CO_2 for the gold nanorods to be taken up by the cells. The coverslip was then rinsed with fresh cell culture medium and placed on a clean glass slide. Two pieces of double-sided tape served as spacers between the glass slide and the coverslip to form a chamber. 30-50 μL of the cell culture medium was added into the chamber to keep the cells from drying out and to provide the cells with nutrition.

3D localization of gold nanorods

The lateral position (x, y) of the gold nanorod is determined as the midpoint of the line connecting the centers of the two images. The z coordinate is obtained by fitting the measured distance between the two images of the gold nanorod into the calibration curve.

To measure the 3D localization precision of gold nanorods with random orientation, gold nanorods were dispersed in agarose gel. The gel matrix was made by dissolving agarose powder (Sigma) in 18.2 mΩ milli-Q water (2% w/w) and heating the mixture for 5 min in a water bath. 50 μL of the 40 nm × 80 nm gold nanorods (Nanopartz) was added to 1 mL of the gel when hot and the mixture was vortexed vigorously and spin-casted onto a pre-cleaned glass slide and covered by a glass coverslip. The sample slide was then cooled down and

brought under the Parallax-DIC microscope and particles at different depths were imaged. A cluster of localization was obtained for each particle by determining the position of the particle in 10 frames of images. The overall 3D localization distribution was then generated by overlapping the center of mass of the localization clusters of 155 gold nanorods. Standard deviations in the x, y, and z directions are thus obtained by fitting the distribution histogram of localization with Gaussian functions. These results are shown in Figures 2E-G.

5D-SPT with auto-focusing

The objective scanner is set to "idle" before the camera starts to record the movies. The objective is adjusted by the user to bring the nanoparticle in focus. The initial coordinates of the target particle are defined by the user by clicking at the center of the upper half-plane image. Because the target object keeps moving in live cells, this procedure needs to be done quickly in time before the nanorod moves out of focus. The click on the screen initiates both the tracking algorithm and the recording function of the camera. Using the initial coordinates as the center, the tracking program defines a 7 × 7 pixel square. A hollow region is formed by framing a smaller square (4 × 4 pixel) inside the big square. The small frame is moved pixel by pixel inside the big square until the biggest difference between the mean intensity of the small square inside of the frame and the hollow region is found, where the small square covers the pixels of the highest contrast constituting the half-plane image of the gold nanorod. The sizes of these squares are chosen to achieve the accurate localization within a time duration that is much shorter than the moving speed of the objective scanner.

The distance between the two half-plane images when the nanoparticle is in focus is measured as d_0. At a distance of d_0 from the first half-plane image, the estimated position of

the second half-plane image is defined. The 4 × 4 pixel small square that covers the first half-plane image is then moved pixel by pixel to cover both itself and the second half-plane image of the nanorod, and two correlation maps are generated. The distance between the centroids of the two correlation maps is then compared with d_0 and the difference is converted to the vertical distance from the focal plane.

The auto-focusing algorithm is realized via the objective scanner controlled by the PI Controller E710. The command is delivered through RS232 interface to the PI Controller and the stage is moved when the status of the objective scanner is detected to be idle. In the same way, the distance between the two half plane images in the next frame after the objective finishes moving is calculated and the distance which the objective should move is determined, and so on until the camera stops recording. The frame number and the distance the objective scanner travels at the corresponding frames are recorded and output in a text file. The *x* and *y* positions of the gold nanorod are determined as the middle point between the two half-plane images of each frames by the correlation mapping and weighing method. To reduce the error caused by the time delay of the adjustment of the objective scanner, the actual vertical position is retrieved as the distance the objective scanner moved from the last frame plus the relative vertical position of the nanorod converted from the distance between the two half-plane images of the current frame. The bright part and dark part intensities of the top half-plane image are recorded. All the data analyses were carried out by running programs written in MATLAB.

Evaluation of the performance of the auto-focusing

The fine adjustment knob of the Nikon i80 microscope was connected to a motorized rotation stage (Sigma Koki, SGSP-60YAM). An Intelligent Driver (Sigma Koki, CSG-602R) was used to control the motion of the motor, thus control the up and down motion of the microscope sample stage. In this part, an immobilized gold nanorod sample was prepared by adding about 5 μL of the above-mentioned 40 × 80 nm gold nanorod solution between a cleaned glass slide and a coverslipe and sealed all the edges by nail polish. Manual adjustment was first performed to find a clear image before starting the tracking program. After the tracking program was switched on, the auto-focusing function will adjust the objective scanner to the optimal position to keep the nanoparticle of interest in focus. When the motorized rotation stage was initiated to move the sample stage up or down, the objective scanner adjusted its position, thus the position of the objective, accordingly to maintain the nanoparticle of interest in focus. Different rotation speeds were used to test the performance of the auto-focusing capability. Both movies and objective scanner positions were recorded simultaneously and exported by tracking program in μmanager. This step was also used every time at the beginning of live cell experiments to cross-check the position of the wedge.

References

(1) Stender, A. S.; Marchuk, K.; Liu, C.; Sander, S.; Meyer, M. W.; Smith, E. A.; Neupane, B.; Wang, G.; Li, J.; Cheng, J.-X.; Huang, B.; Fang, N. *Chem. Rev.* **2013**, *113*, 2469.

(2) Yildiz, A.; Forkey, J. N.; McKinney, S. A.; Ha, T.; Goldman, Y. E.; Selvin, P. R. *Science* **2003**, *300*, 2061.

(3) Pertsinidis, A.; Zhang, Y.; Chu, S. *Nature* **2010**, *466*, 647.

(4) Yildiz, A.; Selvin, P. R. *Acc. Chem. Res.* **2005**, *38*, 574.

(5) Ram, S.; Prabhat, P.; Chao, J.; Ward, E. S.; Ober, R. *Biophys. J.* **2008**, *95*, 6025.

(6) Prabhat, P.; Ram, S.; Ward, E. S.; Ober, R. J. *IEEE Tran. NanoBiosci.* **2004**, *3*, 237.

(7) Prabhat, P.; Gan, Z.; Chao, J.; Ram, S.; Vaccaro, C.; Gibbons, S.; Ober, R. J.; Ward, E. S. *Proc. Natl. Acad. Sci. U. S. A.* **2007**, *104*, 5889.

(8) Speidel, M.; Jonas, A.; Florin, E. L. *Opt. Letters* **2003**, *28*, 69.

(9) Toprak, E.; Balci, H.; Blehm, B. H.; Selvin, P. R. *Nano Lett.* **2007**, *7*, 2043.

(10) Juette, M. F.; Gould, T. J.; Lessard, M. D.; Mlodzianoski, M. J.; Nagpure, B. S.; Bennett, B. T.; Hess, S. T.; Bewersdorf, J. *Nat. Methods* **2008**, *5*, 527.

(11) Pavani, S. R. P.; DeLuca, J. G.; Piestun, R. *Opt. Express* **2009**, *17*, 19644.

(12) Pavani, S. R. P.; Piestun, R. *Opt. Express* **2008**, *16*, 22048.

(13) Ajo-Franklin, C. M.; Ganesan, P. V.; Boxer, S. G. *Biophys. J.* **2005**, *89*, 2759.

(14) Sun, W.; Marchuk, K.; Wang, G. F.; Fang, N. *Anal. Chem.* **2010**, *82*, 2441.

(15) Marchuk, K.; Guo, Y.; Sun, W.; Vela, J.; Fang, N. *J. Am. Chem. Soc.* **2012**, *134*, 6108.

(16) Jones, S. A.; Shim, S.-H.; He, J.; Zhuang, X. *Nat. Methods* **2011**, *8*, 499.

(17) Huang, B.; Wang, W.; Bates, M.; Zhuang, X. *Science* **2008**, *319*, 810.

(18) Yajima, J.; Mizutani, K.; Nishizaka, T. *Nat. Struct. Mol. Biol.* **2008**, *15*, 1119.

(19) Sun, Y.; McKenna, J. D.; Murray, J. M.; Ostap, E. M.; Goldman, Y. E. *Nano Lett.* **2009**, *9*, 2676.

(20) Wang, G.; Sun, W.; Luo, Y.; Fang, N. *J. Am. Chem. Soc.* **2010**, *132*, 16417.

(21) Gu, Y.; Sun, W.; Wang, G.; Fang, N. *J. Am. Chem. Soc.* **2011**, *133*, 5720.

(22) Gu, Y.; Sun, W.; Wang, G.; Jeftinija, K.; Jeftinija, S.; Fang, N. *Nat. Commun.* **2012**, *3*, 1030.

(23) Gu, Y.; Sun, W.; Wang, G.; Zimmermann, M. T.; Jernigan, R. L.; Fang, N. *Small* **2012**, *10*, 785.

(24) van den Broek, B.; Ashcroft, B.; Oosterkamp, T. H.; van Noort, J. *Nano Lett.* **2013**, *13*, 980.

(25) Sun, W.; Gu, Y.; Wang, G.; Fang, N. *Anal. Chem.* **2012**, *84*, 1134.

(26) Gu, Y.; Wang, G.; Fang, N. *ACS Nano* **2013**, *7*, 1658.

(27) Gelles, J.; Schnapp, B. J.; Sheetz, M. P. *Nature* **1988**, *331*, 450.

(28) Ross, J. L.; Ali, M. Y.; Warshaw, D. M. *Curr. Opin. Cell Biol.* **2008**, *20*, 41.

(29) Sheetz, M. P.; Chasan, R.; Spudich, J. A. *J. Cell Biol.* **1984**, *99*, 1867.

(30) Ross, J. L.; Wallace, K.; Shuman, H.; Goldman, Y. E.; Holzbaur, E. L. *Nat. Cell Biol.* **2006**, *8*, 562.

(31) Vale, R. D. *Cell* **2003**, *112*, 467.

(32) Hirokawa, N.; Noda, Y.; Tanaka, Y.; Niwa, S. *Nat. Rev. Mol. Cell Biol.* **2009**, *10*, 682.

(33) Hendricks, A. G.; Holzbaur, E. L. F.; Goldman, Y. E. *Proc. Natl. Acad. Sci. U. S. A.* **2012**, *109*, 18447.

(34) Zajac, A. L.; Goldman, Y. E.; Holzbaur, E. L. F.; Ostap, E. M. *Curr. Biol.* **2013**, *23*, 1173.

(35) Bálint, Š.; Vilanova, I. V.; Álvarez, Á. S.; Lakadamyali, M. *Proc. Natl. Acad. Sci. U. S. A.* **2013**, *110*, 3375.

(36) Gu, Y.; Di, X.; Sun, W.; Wang, G.; Fang, N. *Anal. Chem.* **2012**, *84*, 4111.

(37) Enderlein, J.; Toprak, E.; Selvin, P. R. *Opt. Express* **2006**, *14*, 8111.

(38) Mortensen, K. I.; Churchman, L. S.; Spudich, J. A.; Flyvbjerg, H. *Nat. Methods* **2010**, *7*, 377.

(39) Backlund, M. P.; Lew, M. D.; Backer, A. S.; Sahl, S. J.; Grover, G.; Agrawal, A.; Piestun, R.; Moerner, W. E. *Proc. Natl. Acad. Sci. U. S. A.* **2012**, *109*, 19087.

(40) Schneider, C. A.; Rasband, W. S.; Eliceiri, K. W. *Nat. Methods* **2012**, *9*, 671.

(41) Edelstein, A.; Amodaj, N.; Hoover, K.; Vale, R.; Stuurman, N. *Curr. Protoc. Mol. Biol.* **2010**, *92*, 14.20.1.

(42) Qian, Z. M.; Li, H. Y.; Sun, H. Z.; Ho, K. *Pharmacol. Rev.* **2002**, *54*, 561.

(43) Chithrani, B. D.; Chan, W. C. W. *Nano Lett.* **2007**, *7*, 1542.

(44) Gruenberg, J.; Griffiths, G.; Howell, K. E. *J. Cell Biol.* **1989**, *108*, 1301.

(45) Murk, J.; Humbel, B. M.; Ziese, U.; Griffith, J. M.; Posthuma, G.; Slot, J. W.; Koster, A. J.; Verkleij, A. J.; Geuze, H. J.; Kleijmeer, M. J. *Proc. Natl. Acad. Sci. U. S. A.* **2003**, *100*, 13332.

(46) Brangwynne, C. P.; MacKintosh, F. C.; Weitz, D. A. *Proc. Natl. Acad. Sci. U. S. A.* **2007**, *104*, 16128.

(47) Grafmüller, A.; Voth, Gregory A. *Structure* **2011**, *19*, 409.

(48) Stamer, K.; Vogel, R.; Thies, E.; Mandelkow, E.; Mandelkow, E. M. *J. Cell Biol.* **2002**, *156*, 1051.

(49) Mandelkow, E. M.; Stamer, K.; Vogel, R.; Thies, E.; Mandelkow, E. *Neurobiol. Aging* **2003**, *24*, 1079.

(50) Dixit, R.; Ross, J. L.; Goldman, Y. E.; Holzbaur, E. L. F. *Science* **2008**, *319*, 1086.

(51) Schroer, T. A. *Annu. Rev. Cell Dev. Biol.* **2004**, *20*, 759.

(52) Preza, C.; Snyder, D. L.; Conchello, J.-A. *J. Opt. Soc. Am. A* **1999**, *16*, 2185.

Figures

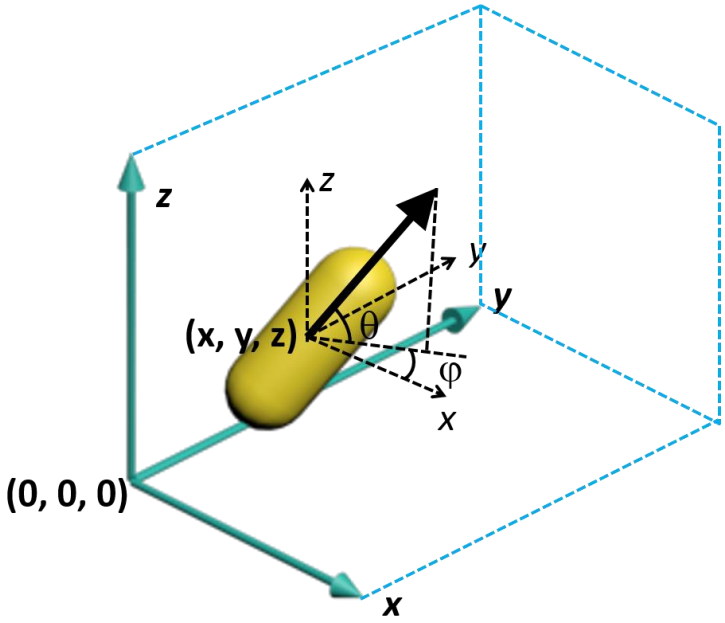

Figure 1. 3D orientation angles of a dipole (bold black arrow): azimuthal angle φ and elevation angle θ. The *x*- and *y*-axes are set according to the polarization directions of the illumination light. The dipole shown here corresponds to the long axis of a gold nanorod, whose centroid locates at (*x*, *y*, *z*).

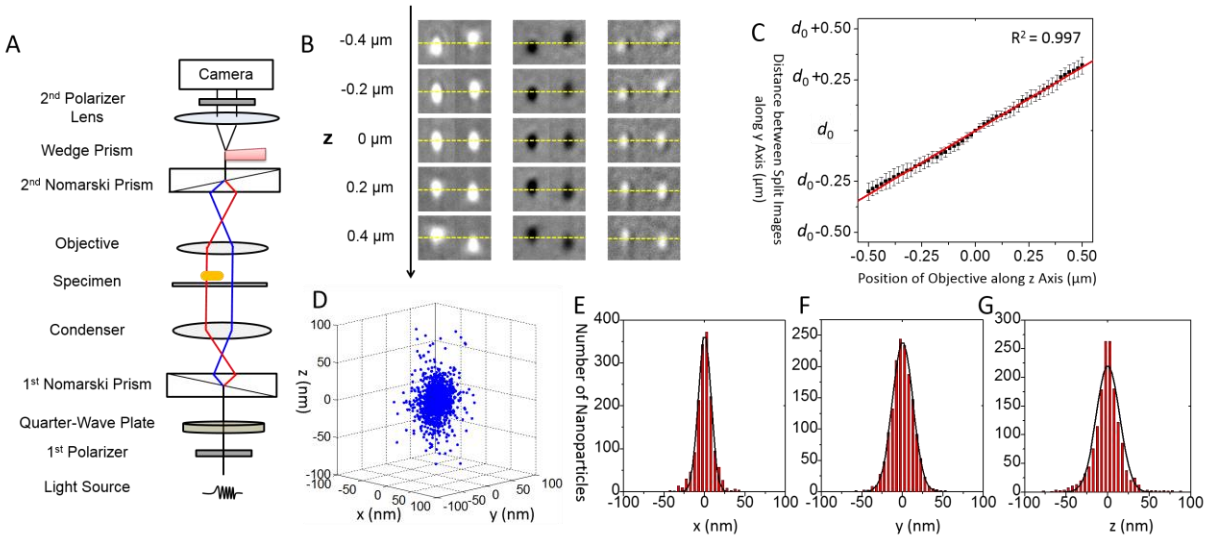

Figure 2. Principle and localization precision of the parallax-DIC microscope. (A) Schematic illustration of the instrumental setup. (B) Bright (left), dark (middle), and half-bright-half-dark (right) images of a gold nanorod (40 nm × 80 nm) at different orientations and vertical positions. The half-plane images are aligned by the center of mass of the nanorod at the focal plane (z = 0 μm). The yellow dashed lines indicate the z position of the center of the gold nanorod in focus. (C) Calibration of the 5D-SPT. The distance between the two half-plane images changes linearly with the z position of the gold nanorod within ±0.5 μm of the focal plane. The distance for an in-focus gold nanorod is defined as d_0. The error bars reflect the standard deviations of the distances measured when the nanorod's azimuthal angle φ changes in the range of 0-180° with 5° steps. (D) 3D localization distribution of the gold nanorod. (E-G) Histograms of the localization distribution along x (E), y (F) and z (G) directions are fitted with Gaussian functions that yield standard deviations of 11 nm in x, 14 nm in y, and 17 nm in z.

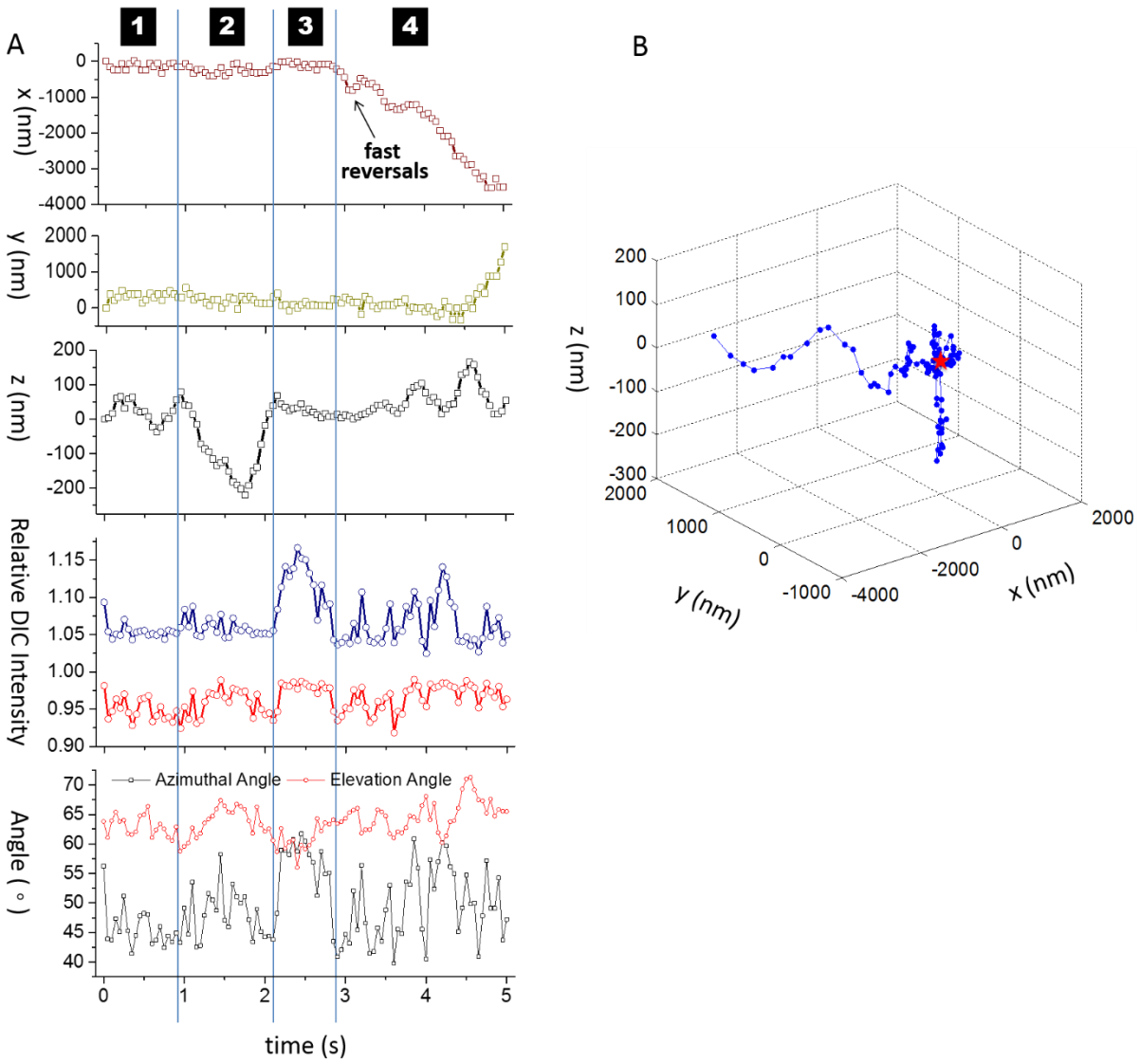

Figure 3. Intracellular transport of a nanorod-containing vesicle in a living A549 cell. (A) The *x*, *y*, and *z* displacement, the relative DIC intensities and orientation angles of the gold nanorod over time. The entire recording can be divided into 4 segments as labelled: (1) searching for a track; (2) vertical transport; (3) a big turn; (4) lateral transport with twisted up-and-down motions. (B) The 3D trajectory of the cargo. The starting position (0, 0, 0) is highlighted by the red star.

Supporting Information

for

Five-dimensional Tracking of Cargos in Live Cells

Supporting movies*

Movie S1. The parallax-DIC images of a gold nanorod at three orientations. From left to right: the nanorod is placed with its long axis at 0°, 45° and 90° relative to the bright optical axis.

Movie S2. The movement of a spherical vesicle inside an A549 human lung cancer cell captured under the parallax-DIC microscope at 20 frames per second.

Movie S3. The transport of a gold nanorod-containing vesicle that performed vertical movement. The corresponding figure is **Figure 3**.

Movie S4. The second example of the transport of a gold nanorod-containing vesicle. The corresponding figure is **Figure S5**.

Movie S5. The third example of the transport of a gold nanorod-containing vesicle. The corresponding figure is **Figure S6**.

*: *Movies are available upon request.*

Supporting Figures

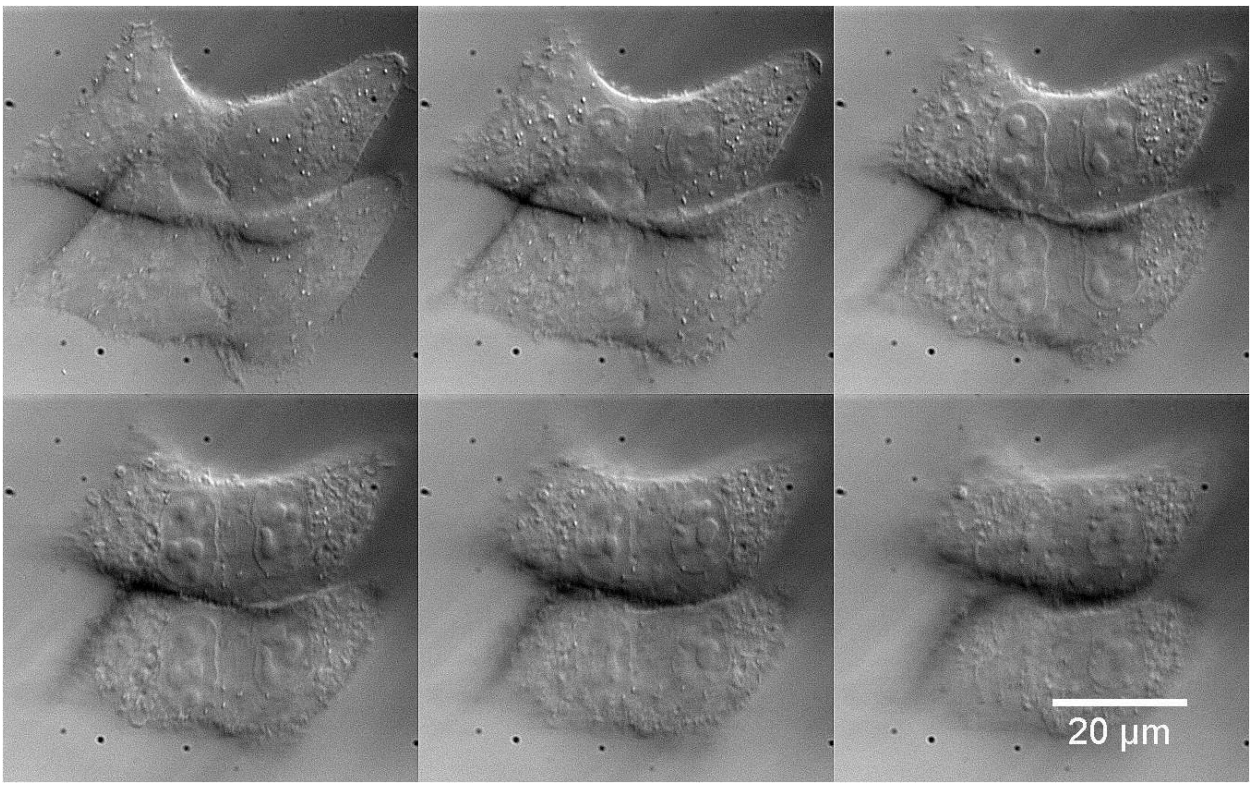

Figure S1. Parallax-DIC images of A549 cells from a vertical scan. The cells are scanned from bottom (the coverslip side) to top in 0.5 µm steps at 20 frames per second.

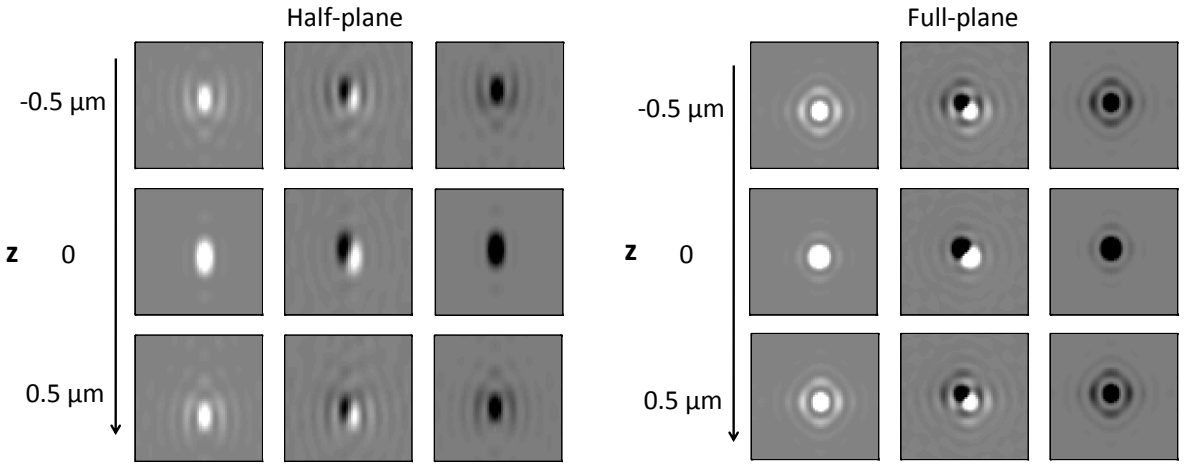

Figure S2. Computer simulated half-plane and full-plane images of gold nanorod showing bright (left), half-bright-half-dark (middle) and dark (right) images at different *z* positions.

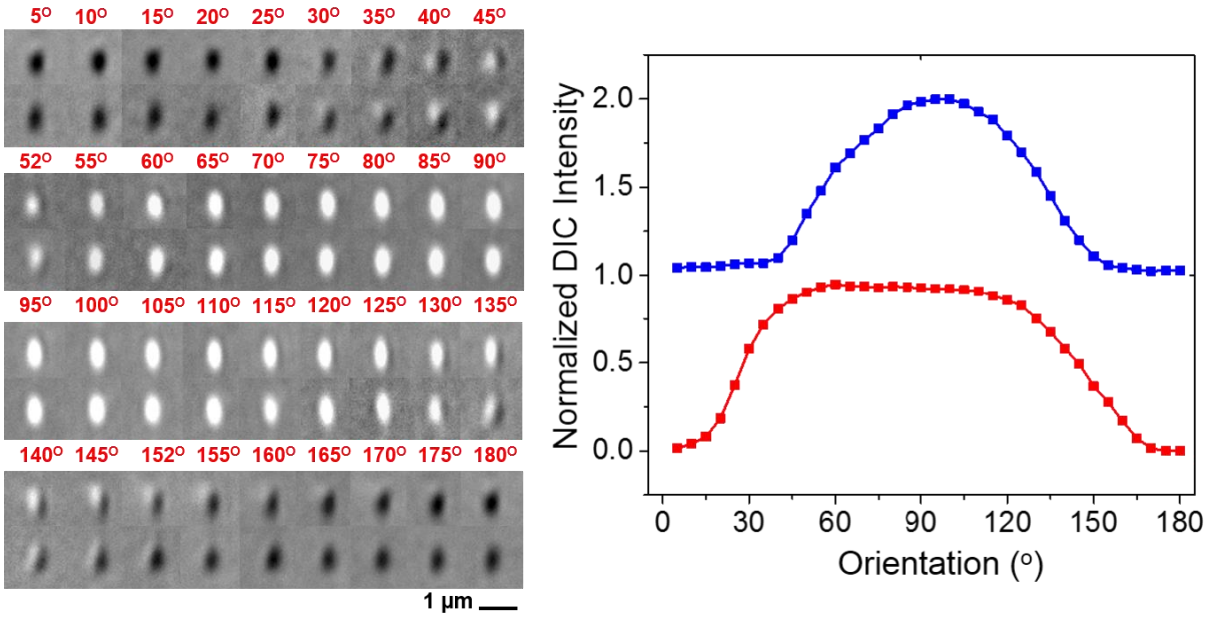

Figure S3. Parallax-DIC images of a gold nanorod at different orientations. **(**A) The in-focus half-plane image patterns of the gold nanorod at different orientations relative to the optical axes. The sample slide is rotated from 5° to 180° in 5° steps. The scale bar represents 1 μm. (B) The normalized bright part (blue) and dark part (red) intensities of the half-plane images on the top in each pair.

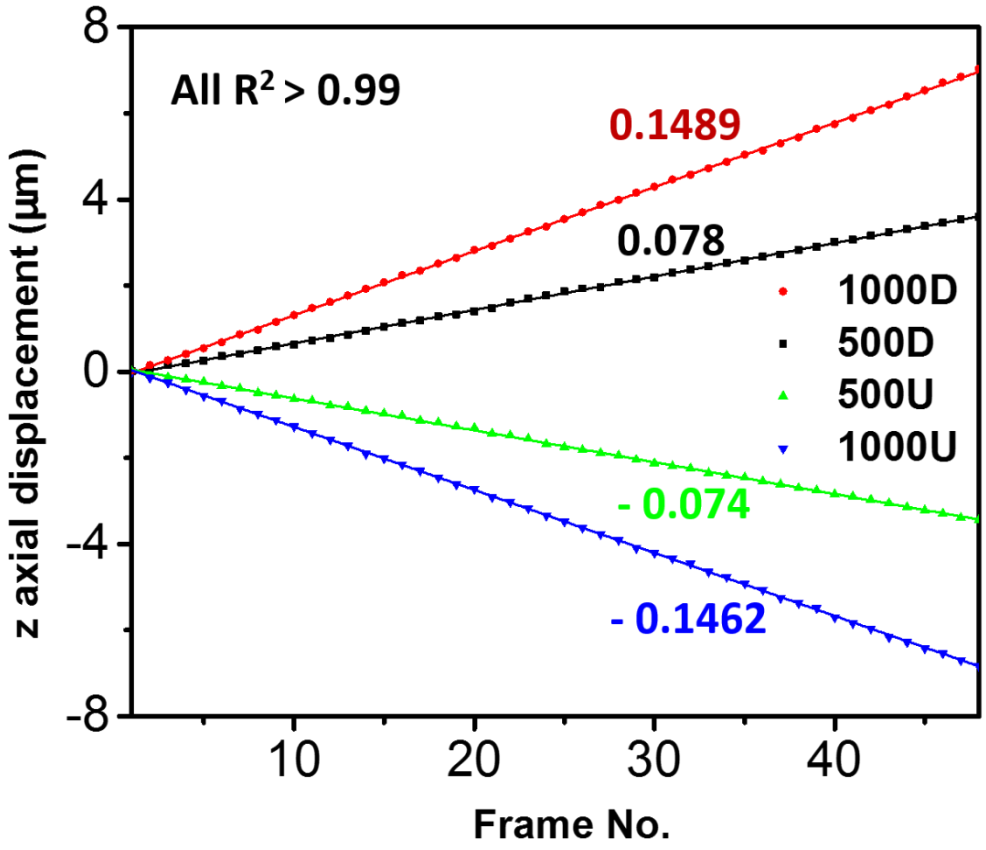

Figure S4. Evaluation of the Performance of the auto-focusing. Solid red circles (1000D) and solid black squares (500D) corresponding to the z axial of objective scanner increase when microscope sample stage was moved down at 1000 and 500 steps per second (0.70 µm/s and 0.35 µm/s) while solid green ascending triangle (500U) and solid blue descending triangle (1000U) refer to z axial of objective scanner decrease when sample stage was moved up at 500 and 1000 steps per second. These data points were all well fitted with linear lines and the coefficient of determination (R^2) were all greater than 0.99. The slopes were labelled with same color in the figure.

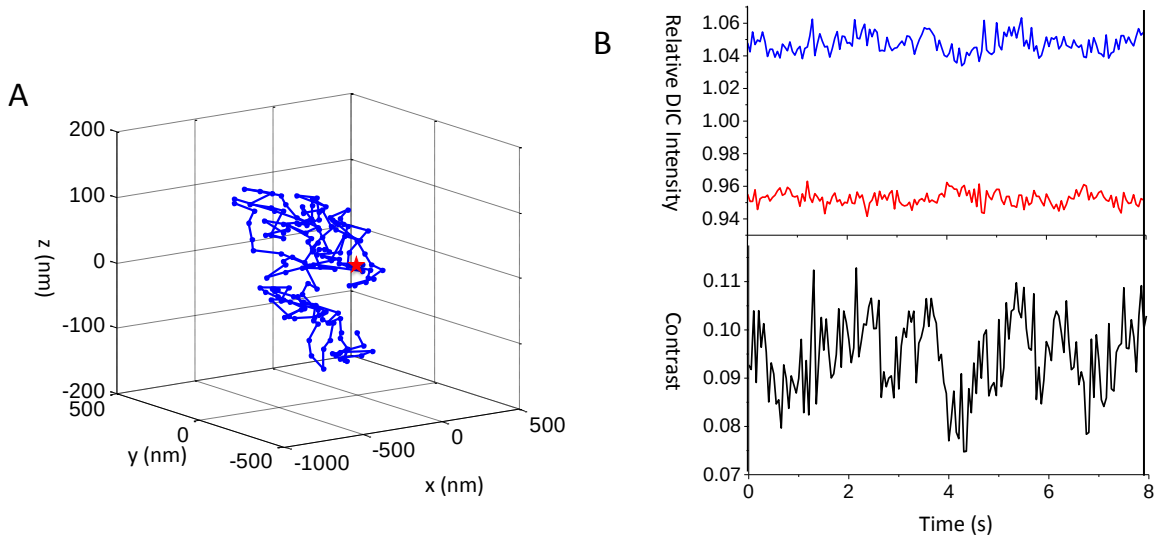

Figure S5. The 3D trajectory (A) and the relative DIC intensities and contrast (B) of a vesicle moving in a live A549 cell. The relative DIC intensities of the bright part and dark part are shown in blue and red, respectively. The contrast is shown in black. The starting position (0, 0, 0) is highlighted by the red star. The standard deviations of the intensity and contrast changes are all smaller than 0.02 unit, showing consistent signals for the vesicle remained in focus.

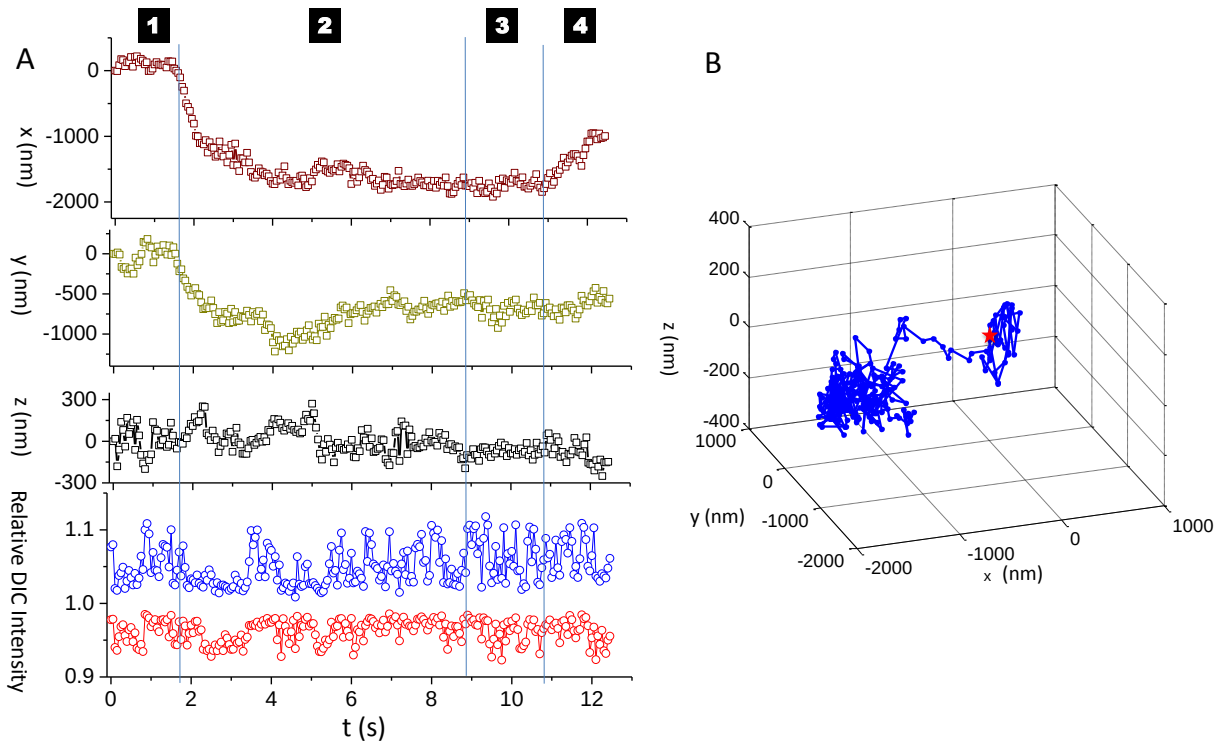

Figure S6. Intracellular transport of a gold nanorod-containing vesicle. (A) The x, y and z displacement (shown in wine, dark yellow, and black respectively) and the relative DIC intensities of the nanorod moving inside of a live A549 cell. The bright part and dark part intensities are shown in blue and red respectively. The blue lines divide the movement into two segments: The particle (1) performed regional random diffusion; (2) transported along the microtubule track with twisted up-and-down motions; (3) resumed regional random diffusion; (4) underwent directional transport. (B) The three dimensional trajectory of the nanorod. The starting position (0, 0, 0) is highlighted by the red star.

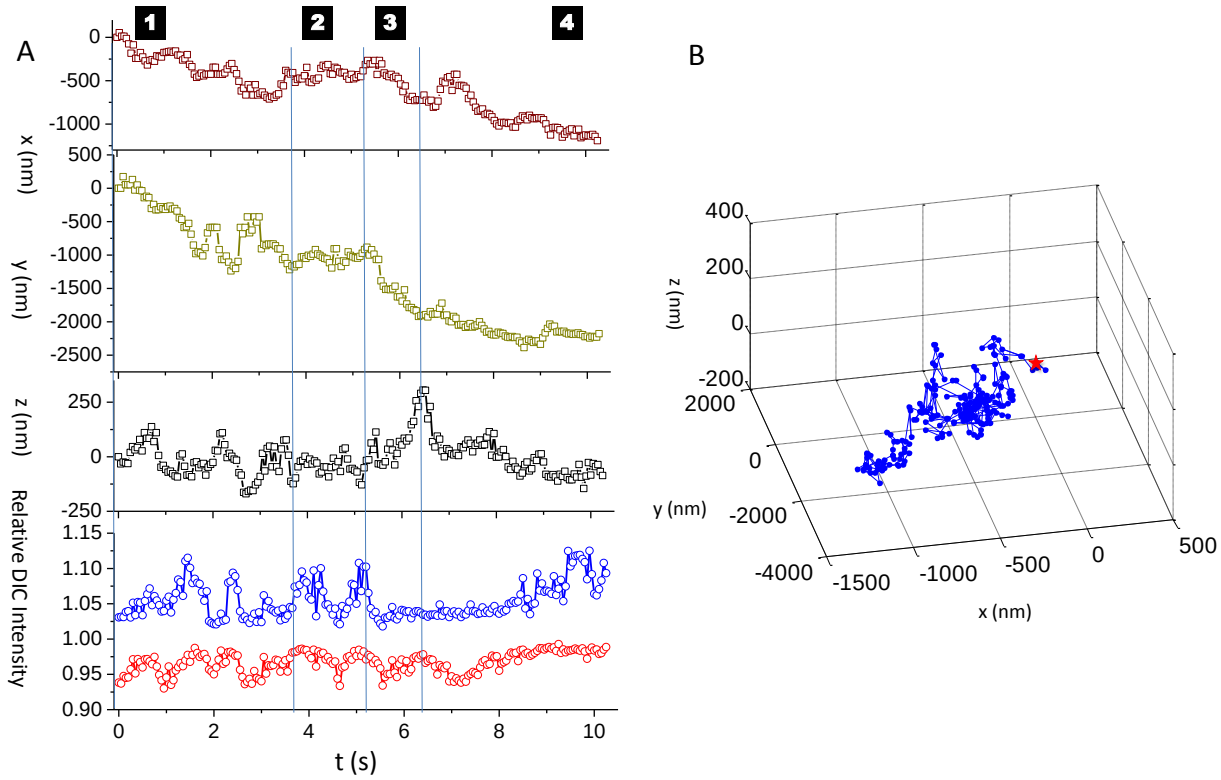

Figure S7. Another example of intracellular transport of a gold nanorod-containing vesicle. (A) The *x*, *y*, and *z* displacement (shown in wine, dark yellow, and black respectively) and the relative DIC intensities of the nanorod moving inside of a live A549 cell. The bright part and dark part intensities are shown in blue and red respectively. The cargo (1) transported with twisted up-and-down motions; (2) paused with rotation; (3) underwent directional transport; (4) transported with twisted up-and-down motions again. (B) The three dimensional trajectory of the nanorod. The starting position (0, 0, 0) is highlighted by the red star.

CHAPTER 4

AUTOCORRELATION FUNCTION ANALYSIS OF ROTATIONAL DYNAMICS OF GOLD NANOROD

Abstract

Single particle tracking (SPT) is proven to be powerful in investigating the rotational dynamics of complex systems. With the development of light microscope and sensitive camera, vast time-lapse imaging data can be recorded in single particle orientation and rotational tracking (SPORT) experiments. It is of importance to use the appropriate data analysis method to extract accurate and precise information from these recorded movies. Autocorrelation function (ACF) analysis was reported to be an effective tool to study the correlation of the fluctuation of intensities in a time series. In this study, the rotational dynamics of polyethylene glycol (PEG) modified gold nanorods (AuNRs) on synthetic lipid bilayers were recorded with high temporal resolution in differential interference contrast (DIC) microscopy without suffering photobleaching. Binning was used to study the influence of the exposure time on AuNR rotation. ACF analysis coupled with computer simulations was used to investigate rotational dynamics based on the correlation of the fluctuations between the DIC bright and dark intensity. The comprehensive study on the data treatment and the effect of experimental parameters on rotational dynamics will be beneficial to data interpretation and experiment design in DIC-based SPORT experiment.

Introduction

Single particle tracking (SPT) has been proven to be a useful tool in dynamic studies of in material science and in biological systems as it provides the possibility to observe the heterogeneous behaviors of individual probes, which may be cancelled out in ensemble measurements, to reveal the real distributions of molecular activities.[1-8] SPT experiments record the motions of individual particles (tracking probes) over time and generate time-lapse intensity data.[1,9] Data analysis is as important as the experiment itself because the SPT data contain not only the intensity at each given time in the time series but also the position and/or orientation of particles that are being tracked. Moreover, the information usually correlated to the dynamic behavior of the particles in complex systems, such as live cells. The derived information can then be linked to underlying processes.[10]

Autocorrelation function (ACF) analysis is a powerful mathematic tool. It has been used in numerous areas such as statistics, signal processing, and music recording. It has been widely used in scientific data analysis including but not limited to fluorescence correlation spectroscopy (FCS),[11-14] the determination of the particle size distributions in dynamic light scattering (also known as photon correlation spectroscopy), the SEQUEST algorithm for mass spectrum analysis,[15] and single particle/molecule rotational tracking.[16-20]

ACF analysis has been demonstrated to be an effective tool to extract rotational time scale and fluctuation of intensity, even from low signal-to-noise (S/N) data.[16-18,21] The nanoscale behavior of individual probes and their rotational dynamics, which usually relate to the molecular mechanisms, can be obtained by analyzing the intensity fluctuations over time. In spite of significant advances in synthesis of brighter and more photostable fluorescent probe and the availability of more sensitive detectors, the observation time of the

fluorescent probes in single molecule fluorescence spectroscopy/microscopy is relatively short because of the use of laser as light source and the irreversible photochemical bleaching of fluorescent probes. Previous studies demonstrated that the length of the recorded trajectory can greatly affect the rotational determination in ACF analysis.[16-18] Moreover, the effective sample size (the number of independent observations) in a time series of ACF analysis is smaller than the recorded trajectory length. The measurement time should be more than an order of magnitude longer than the rotational correlation time to capture the rotational dynamics.[16] Shorter observation time and lower S/N may lead to greater statistical uncertainty. [22-24] One way to improve the quality of ACF analysis is to obtain the trajectories as long as possible, for example, by lowing the probing laser power, reducing exposure time, using oxygen scavenging systems to remove quenchers in solution, *etc*.

Nonfluorescent probes possess excellent photostability and unique optical properties, are becoming a popular alternative choice to traditional fluorescent probes in SPT applications. [25-27] Gold nanorods (AuNRs) as one of the outstanding examples, have been widely used in single particle orientation and rotational tracking (SPORT) experiments due to its high photostability, versatile surface functionality and foremost, the anisotropic localized surface plasmon resonance (LSPR).[13,14,19,20,28-31] ACF analysis was used in several of these studies in several reports for determining the rotational dynamics of AuNRs.[13,14,19,20,28,31] Surface modification of the AuNRs controls the biological behavior.[32-34] PEG is one of the most commonly used surface modifiers to reduce the unspecific interactions and to maintain the stability in physiological conditions.

DIC microscope uses halogen lamp rather than laser as light source. The considerably low illumination light intensity causes minimal disruptions to cell functions. Combined with

photostable AuNRs as tracking probes, it is possible to track the motion of AuNRs for theoretically unrestricted observation time without suffering photobleaching in live cells. Experimentally, the observation duration of SPT in DIC microscopy is limited by the cell viability, image data storage, sample drifting, and apparatus instability. Typically, each cell sample can be used for up to several hours.

In this study, the rotational dynamics of PEG-modified gold nanorods on synthetic lipid bilayers were recorded under a DIC microscope using a Hamamatsu ORCA-Flash 2.8 complementary metal-oxide semiconductor (CMOS) camera. Only those AuNRs without lateral motions were used as targets of interest. High temporal resolution movie recordings were achieved by limiting the region of interest to a small area to maximize the frame rate in sub-array readout mode. Different "temporal resolution" image stacks were generated using the bin function in NIH ImageJ software. These image stacks were then subjected to ACF analysis through fitting stretched exponential function to extract the mean relaxation time and correlation coefficient. The influence of the experiment parameters such as the recorded trajectory length and temporal resolution were studies with the help of computer simulations. Hopefully, this study can set up a model system to help with the data analysis and experiment designs of future rotational dynamics studies.

Experimental Section

Preparation of PEG-modified gold nanorods

Modification of AuNRs with PEG was carried out by following a published method with modifications.[35] The cetyltrimethylammonium bromide (CTAB) stabilized AuNRs (40 nm × 118 nm, longitudinal SPR 700 nm, 2.4×10^{10} nps/mL) were purchased from Nanopartz

(Salt Lake City, UT). Before modification, the solution was first centrifuged at 3000 g for 6 min and resuspended in 18.2 MΩ deionized water twice to get rid of the excessive CTAB in the solution. PEG-thiol (MW 5000) obtained from Sigma Aldrich was diluted in dimethyl sulfoxide (DMSO) to a final concentration of 20 mM. 4 μL of the 20 mM PEG-thiol solution was allowed to react with 200 μL pre-cleaned gold nanorods solution at room temperature for 3 h. The resultant PEG-modified AuNRs solution was cleaned up by centrifugation and resuspended in 18.2 MΩ deionized water before using. Zeta potential of the PEG-modified AuNRs solution was measured to be $\zeta = +2.1$ mV on a Nano-ZS90 Zetasizer manufactured by Malvern Instruments, United Kingdom.

Preparation of synthetic lipid bilayer

Reported methods were used for the synthetic lipid bilayer preparation with slightly changes.[36,37] The neutral phospholipid 1-palmitoyl-2-oleoyl-sn-glycero-3-phosphocholine (POPC) solution (25 mg/mL in chloroform) was purchased from Avanti Polar Lipids. 20 μL of the POPC solution was dried by a gentle nitrogen stream. In order to prevent the disruption of the lipid self-assembly by chloroform, the dried POPC was placed in vacuum for more than 3 h at room temperature to eliminate the residual chloroform. 1 mL phosphate buffered saline (1× PBS, pH 7.4) was added to the dried POPC and the final POPC concentration became 0.5 mg/mL. A cloudy multilamellar vesicles suspension solution was produced in PBS after 30 min rehydration and vortexing. The large unilamellar vesicles solution was produced by extruding the suspension solution through a 100 nm pore size polycarbonate membrane (WHA110405) from Sigma-Aldrich for no less than 21 times using a mini-extruder manufactured by Avanti Polar Lipids. The planar synthetic lipid bilayer self-

assembled in the sandwiched structured microscopic chamber made by glass slide, double-sided tapes, and cover slipe in about 10 min when the unilamellar vesicle solution was injected. 1× PBS was used to wash away the excess free lipids three times. PEG-modified AuNR solution was added onto the synthetic lipid bilayer in the sandwiched chamber before imaging.

DIC microscopy

The Nikon Eclipse 80i upright microscope operated in DIC mode was used for this work. The light source, a halogen lamp has a maximum output power of 100 Watts. The maximum output power of the lamp was used for all experiments for fair comparison. The microscope utilized two polarizers, two Nomarski prisms, a high numerical aperture (NA 1.4) oil-immersion objective and a NA 1.4 oil condenser for DIC image formation. A semrock 700/13 nm BrightLine single-band bandpass filter was inserted in the illumination light path. Movies and images were collected by a Hamamatsu ORCA-Flash 2.8 CMOS camera. HCImage Live software from Hamamatsu was used to control the camera. Sub-array readout function of the CMOS camera was used to confine the region of interest into 24 × 24 pixels when 1 ms temporal resolution was used for capturing movies and 40 × 24 pixels for 2 ms temporal resolution recording. The recorded movies were directly saved into memory as TIFF images with the option of streaming data to memory. This can maximize the read out speed (frame rate) of the recordings. NIH ImageJ and MATLAB were used for image processing and the following data analysis and computer simulations.

Data analysis and computer simulations

After the movies were collected, the bin function (under the main menu, Image, Transform, Bin) in imageJ was used to generate desired artificial "temporal resolution" image stacks. X, Y shrink factors were always set to 1 while Z shrink factor was set to different value to get artificial image stack with different "temporal resolution". Meanwhile, summation was used as default bin method for all binning operations. Different image stacks with desired "temporal resolution" can be generated in similar manner. ImageJ Macros codes were compiled for batch binning processing.

The time dependent DIC bright (I_B) and dark intensity (I_D) traces were extracted from the recorded image stacks and the substacks that produced by binning. Analogues to the s polarized and p polarized scattering or fluorescence in polarization anisotropy studies, the reduced linear dichroism (LD) in DIC was defined as:[17,31,38] $\mathrm{LD}(t) = \frac{I_B(t)-I_D(t)}{I_B(t)+I_D(t)}$. The rotational dynamics of PEG-modified AuNRs were analyzed from the correlation of the fluctuating bright and dark intensities. This reduced LD represents the measurement of the transition dipole orientation when the effect of high N.A. optics is taken into account. It can also reduce the noise caused by experimental artifacts such light intensity fluctuations. The autocorrelation of the reduced LD was then fitted by a stretched exponential function $f_0 e^{-(t/\tau)^{\beta}}$ through non-linear least squares fittings.[18,19,38-40] Here, f_0 is the pre-exponential factor, τ is the characteristic time constant, and β is the stretching exponent. The mean relaxation time ($<\tau>$) can be calculated as: $\langle \tau \rangle = \frac{\tau}{\beta}\Gamma(\frac{1}{\beta})$. Here Γ is Gamma function. $<\tau>$ of the decay represents the in-plane rotating speed of the AuNRs, with a smaller $<\tau>$ value corresponding to a faster rotation.[19]

The computer simulations was adopted from a previous report with modifications to describe the rotational Brownian motion of AuNRs with randomized rotation direction and step size for ACF analsis.[20] The normalized DIC intensities were calculated based on the simplified mathematical equations with the elevation angle θ and the azimuthal angle φ: $I_{bright} \approx 1 + \cos^2\theta\sin^4\varphi$ and $I_{dark} \approx 1 - \cos^2\theta\cos^4\varphi$.[30] Different simulation data were generated to study the influence of rotation speed and trajectory length on the ACF analysis as mentioned in the results and discussion.

Results and Discussion

The average size of the CTAB-capped AuNRs is 40 nm in diameter and 118 nm in length. The longitudinal SPR peak is located at 700 nm. Because PEG modification does not alter the longitudinal SPR of the AuNRs, so a 700/13 nm single-band bandpass filter was used to selectively excited the longitudinal SPR of the PEG-modified AuNRs to produce the highest DIC contrast of the AuNRs since the wavelength dependent properties of noble metal nanoparticle in DIC microscopy. The size of the CTAB-capped AuNRs used in this study is much larger than the ones that were used in other studies which also utilized ACF analysis for rotation dynamics.[13,14,19,28,29] Positively charged CTAB-capped AuNRs (zeta potential ζ = + 40 mV) changed to nearly neutral PEG-modified AuNRs (zeta potential ζ = + 2.1 mV). The hydrodynamic size of the AuNRs will increase a little after PEGylation. Thiol groups in the PEG molecules formed covalent bond with the surface of AuNRs by replacing the surface CTAB. The slightly positive charge of the PEG-modified AuNRs solution might attribute to the CTAB residues that was not able to be removed completely by centrifugation. This also indicated the successful surface modification of the PEG on AuNRs.

A dense layer of PEG on AuNRs rendered the hydrophilicity to AuNRs, thereby increased the water solubility of the PEG-modified AuNRs. Based on the experiment observations (**Movie S1**), the lateral diffusions of most of the PEG-modified AuNRs were restricted after they landed on the synthetic lipid bilayer surface. This might because of the relatively large size of the PEG-moidfied AuNRs and possible interpenetration of the PEG molecules inside the lipid bilayer.[31] The insertion of PEG molecules inside the synthetic lipid bilayer caused the lateral 'frozen' of the PEG-modified AuNRs, however, the particles were still rotating since the PEG chains are not rigid. If large amount of the PEG chains from a same particle anchored into the synthetic lipid bilayer, the stop of AuNR rotation may occur. Yet, these speculations will require further experimental evidences.

The S/N ratios of the bright and dark intensity of DIC measurements increase with the increase of particle size. The AuNRs used in this study are large enough to generate sufficiently high signal intensity at millisecond temporal resolution. Thus most of the movies were recorded at 1 or 2 ms although signal strength was sacrificed with the increasing of temporal resolution. The recorded movies are time dependent image stacks. The sub-array readout function of the Hamamatsu ORCA-Flash 2.8 CMOS camera allowed the selection of small area of CMOS image sensor for detecting only the AuNRs of interest. Theoretically, the readout speed increases with the decrease of the vertical line width of the section. However, the horizontal line width of the recorded movies were also restricted in the experiments to reduce the size of the recorded movies, and thus the software processing time was reduced to maximize the readout. Meanwhile, the recorded images were first streamed into memory and then saved into hard drive, this also speeded up the data processing. It is

possible to achieve maximum 1273 frames/second (fps) when the pixel size of the vertical line of 8 is used.

In the context of image data processing, binning usually achieved by combining the signal of the adjacent pixels in image sensor to increase the sensitivity as tradeoff for resolution since the overall number of pixels is reduced. However, the binning used in the studies is slightly different. For any given image stack, X, Y shrink factors were always set to 1 and Z shrink factors was specified to certain value to produce a new substack with different artificial "temporal resolution". The substack is a sequence of images made by bins that is calculated from the summation of all the image clusters of each bin. For example, if 2 is used as Z shrink factor for a 15000 frame movie recorded at 2 ms, the binning process will generate a 7500 frame image stack with artificial "temporal resolution" of 4 ms. The same method was used to generate different "temporal resolution" image stacks. ImageJ Macros codes were compiled for batch binning processing. It is worth noting that this binning method only works for those PEG-modified AuNRs that are laterally 'frozen'. If the AuNRs are moving, the Z shrink of the binning will result in distorted images in the substacks.

Theoretically, the AuNRs can be tracked for unlimited time in DIC microscopy. Experimentally, especially in live cell studies, the observation duration is restricted by many experimental factors such as the instrument stability, cell viability, and data storage limit. Practically, we recorded 15000 frame (30 s) movies for the PEG-modified AuNRs rotating on the synthetic lipid bilayer. Initially, 2 ms temporal resolution was used for capturing these 15000 frame movies unless stated otherwise. The time-lapse DIC bright and dark intensities were extracted from these image stacks to calculate the reduced linear dichroism. The azimuthal angle and elevation angle of the PEG-modified AuNRs can also be obtained from

the relative intensities. Through non-linear least squares fittings of the correlation of the reduced linear dichroism, the mean relaxation time and correlation coefficient were extracted. Same data processing procedures were followed to extract the mean relaxation time and correlation coefficient of all the binned substacks.

When a PEG-modified AuNR is lying flat and fixed on a microscope coverslip, the elevation angle θ equals to 0, which will further simplify the two DIC intensity equations to: $I_{bright} \approx 1 + \sin^4\varphi$ and $I_{dark} \approx 1 - \cos^4\varphi$. When the sample is rotated on the stage continuously with the same step size (same azimuthal angle change in each step) and direction for a full 360 degree rotation, the DIC bright and dark intensities increase or decrease together. This provided an excellent correlated in-plane rotation example, and the correlation coefficient of the intensities was calculated to be 0.88. This deviated from the perfect correlated correlation value of 1 because of the term of $\sin^4\varphi$ and $\cos^4\varphi$ in the intensities affect the perfect linear dependency. As shown in **Figure S1** (**Supporting information**), a representative example of a 40 × 118 nm PEG-modified AuNRs rotating with 10 degree increment for a 360 rotation. The experimental data (solid blue squares and solid purple dots) were in good agreement with the calculated intensity changes (solid red line and solid black line). Due to the presence of noise in the imaging experiments, a typical 10 – 15% relative errors exist in the DIC intensity measurements.[30] An AuNR rotates out of the horizontal plane with a fixed azimuthal angle is denoted as basic out-of-plane rotation. All the other more complex rotational modes can be considered as the combination of the in-plane and out-of-plane rotation with different proportions.[20]

Figure 1 and **Figure 2** showed the DIC bright and dark intensity traces for a same AuNR that were recorded at (A) 2 ms for 15000 frames and the binned traces at (B) 6 ms, (C)

10 ms and (D) 30 ms at two different time t_1 and t_2. The total observation durations were all 30 s. With higher temporal resolution, the imaging frame rate is higher, thus more image frames were captured. The binned substacks of 6 ms, 10 ms, and 30 ms movies contained 5000, 3000, 1000 frames, respectively. Also binning reduced the noise in DIC measurements and provided noticeable increments on the bright and dark intensity. However, the background intensity also increased in the same amplitude, which means there's no improvement on the DIC contrast though binning.

ACF analysis were applied to these movies, and correlation coefficients were calculated for each of them, Figure 1 (A) 0.71, (B) 0.79, (C) 0.80, (D) 0.82 and Figure 2 (A) 0.71, (B) 0.77, (C) 0.78, (D) 0.80.The correlation coefficients calculated from all these movies were all larger than 0.7, which indicated the mostly in-plane rotation of the PEG-modified AuNR on the synthetic lipid bilayer. For the rotaion recorded in **Figure 1** (time t_1), the mean relaxation times decreases from 0.088 to 0.062,and 0.048 s when the exposure time increased from 2 to 6, 10 ms and then increased to 0.120 s at 30 ms. Similar trend was observed for the rotaion recorded in **Figure 2** (time t_2), as the mean relaxation times changed from 1.33 to 1.18, 1.19, 1.82 s for exposure time 2 to 6,10, 30 ms. The changes on the apparent mean relaxation times from the ACF analysis might related to the true rotation of the AuNRs. If the exposure time is shorter than real rotation time, then more than one frame of the DIC image of the AuNR in same orientation may be recorded. However, in the ACF analysis, every frame of the image is counted to calculate the mean relaxation time. Rotations with more extra frames will yield a larger mean relaxation time. It should be emphasized that the rotational mean relaxation times were calculated only for those rotating PEG-modified AuNRs without lateral movement and hence cannot reflect the dynamics of the whole

population. The rotational mean relaxation times calculated for different particles or the same particle observed at different time were different. The heterogeneity of the rotational dynamic is confirmed and this is one of the causes that lead to nonexponential decays. The semi-quantified rotational mean relaxation time is in the range of 0.085 to 1.33 s, which is consistent with the results observed on live cell membranes.[19]

The influence of the exposure time on the correlation coefficient have also been investigated. Both the original data collected with different exposure time and the data binned from shorter exposure time display the same increase of correlation coefficient as the exposure time increases (**Figure 3**). Relative measurement errors of the DIC bright and dark intensities decrease with the increase of the exposure time. The correlation coefficients are all smaller than 0.88, which indicates a small portion of the out-of-plane rotation is involved in the rotational dynamics of the PEG-modified AuNRs. As demonstrated in the previous study, out-of-plane rotation will only contribute to the intensity but won't affect the image patterns.[20] This is also predictable from the mathematical equations for orientation calculations.

When the particles are not rotating, the DIC bright and dark intensities are supposed to be constant. DIC images of PEG-modified AuNRs show different proportions of black and white depending on the particle's orientation. AuNRs orientated to be a totally white, a half white half black, and a totally black were recorded at 1 ms for 30,000 frames. These movies were used to generate the DIC bright and dark intensity traces with different exposure times. **Figure S2** in **Supporting Information** shows the complete 1000-frame DIC bright and dark intensity traces of the binned substack at 30 ms. Instead of having constant bright and dark intensities, the traces displayed frequent intensity fluctuations which may lead people to

believe that these intensity changes are arose from rotation. **Figure 4** (A, D, and G) are extracted from the first 100 frames of the DIC intensity traces of the **Supporting Information Figure S2** (A, B, and C). There are two ways to distinguish the DIC bright and dark intensity traces of rotating and not rotating AuNRs. One way is through direct visualization of the DIC image stacks. **Figure 4** (B, E, and H) illustrates the 100-frame DIC image stack in the stitched way. The DIC images did not change over time. The other way is through ACF analysis as shown in **Figure 4** (C, F, and I). The 1 ms movie were binned into different exposure times. The correlation coefficients fluctuates around zero for different exposure times for all of these three cases. It is known that for a time series that is completely random, as in this case, the correlation coefficient is normally distributed with a mean of zero. This demonstrates that the ACF analysis is fairly insensitive to noise.

Consider that PEG-modified AuNRs were performing predominantly in-plane rotational motions on synthetic lipid bilayer, the computer simulations were carried out for in-plane rotations. **Figure 5** shown the simulated DIC bright and dark intensity traces of (A) fast and (B) slow in-plane rotations at 2 ms. The step size of the fast rotation was to be 2.5 times larger than that of the slow rotation. With the larger step size, the AuNR has higher probability to rotate a larger angle in two consecutive frames. The rotational mean relaxation times extracted from these two traces were calculated to be 0.093 and 0.52 s. The correlation coefficients were as expected to be around 0.88 for the perfect in-plane rotations.

Conclusions

In summary, PEG-modified AuNRs rotating on synthetic lipid bilayer was used as model system for rotational dynamics study. The rotational motions of the laterally frozen

AuNRs were recorded with high temporal resolution under a DIC microscope. The faster temporal resolution image stacks were binned on the time axis in ImageJ to generate substacks with different temporal resolutions and these image substacks were subjected to ACF analysis and used for comparison with simulation results. These recorded rotations of AuNRs showed predominately in-plane motions. The correlation coefficient increases with the increase of exposure time. The ACF analysis is insensitive to noise. Further development of this approach can help on the data analysis and experimental designs of rotational studies using DIC-based SPORT technique.

Figures

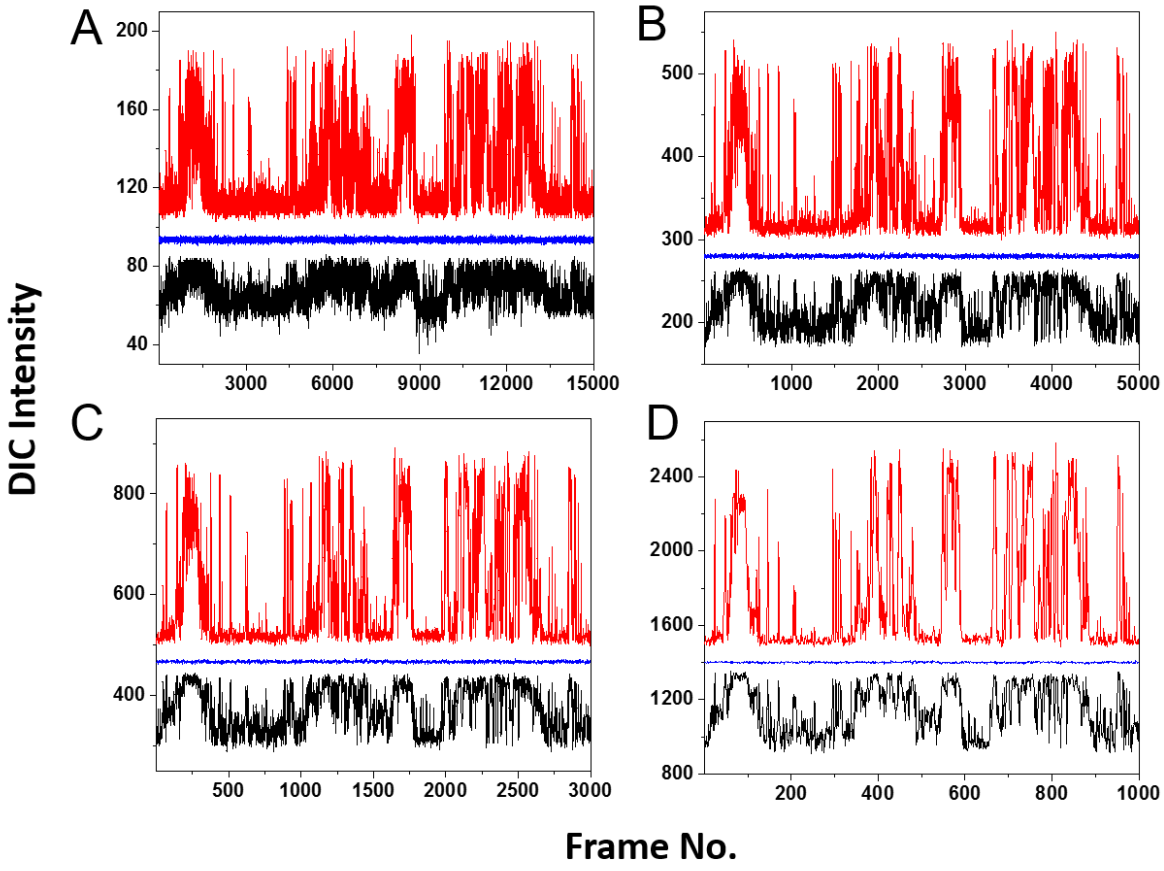

Figure 1. A rotation case of the PEG-modified AuNR on synthetic lipid bilayer at time t_1. (A) is the DIC bright and dark intensity traces for the originally recorded movie at 2 ms. (B, C, and D) are the DIC bright and dark intensity traces for the substacks obtained from binning for 6 ms, 10 ms and 30 ms.

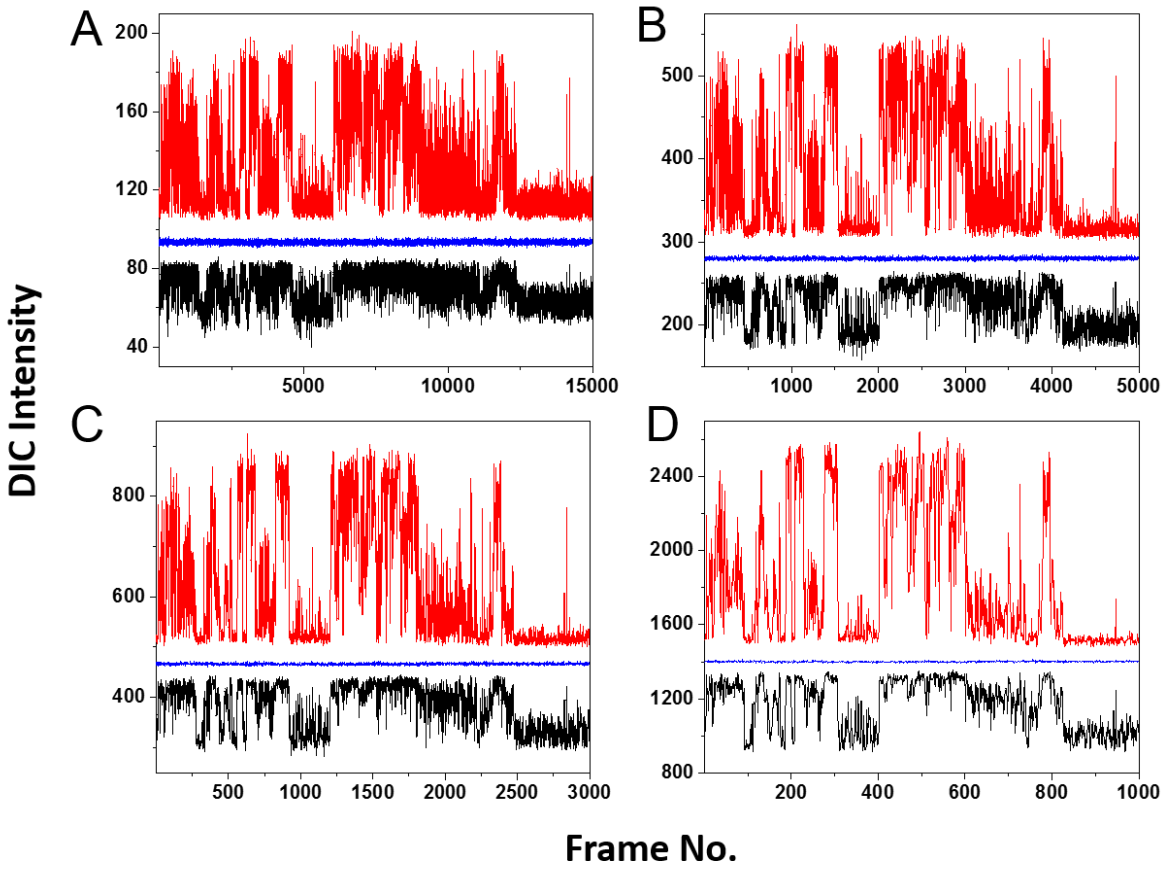

Figure 2. A rotation case of the same PEG-modified AuNR as in **Figure 1** on synthetic lipid bilayer at a different time t_2. (A) is the DIC bright and dark intensity traces for the originally recorded movie at 2 ms. (B, C, and D) are the DIC bright and dark intensity traces for the substacks obtained from binning for 6 ms, 10 ms and 30 ms.

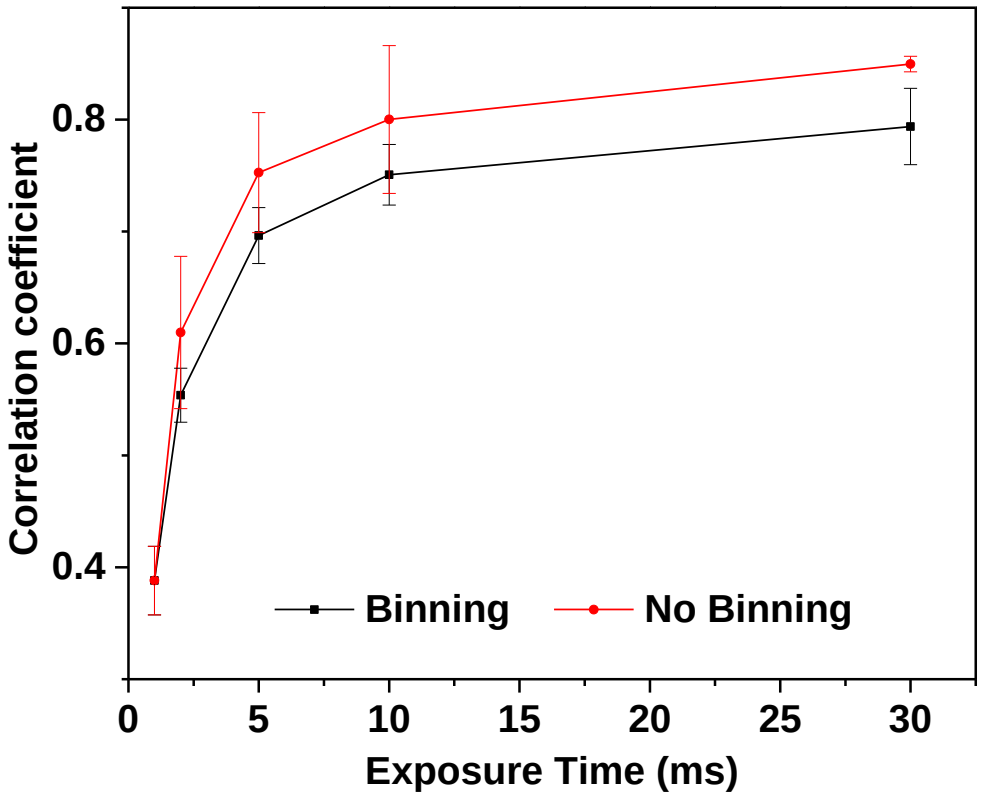

Figure 3. Influence of the exposure time on correlation coefficient of PEG-modified AuNRs rotation. Black solid square data points are the correlation coefficients obtained from the ACF analysis of the binned substacks of 2ms, 5ms, 10ms, and 30 ms from the originally recorded 1 ms movie (first data point from the left). Red solid dots data points were extracted from the ACF analysis of movies that were experimentally recorded at 1 ms, 2ms, 5ms, 10ms, and 30 ms, respectively. All the data points were the average of 5 measurements. Error bars represented the standard deviations. Same movie was used to produce the first data point.

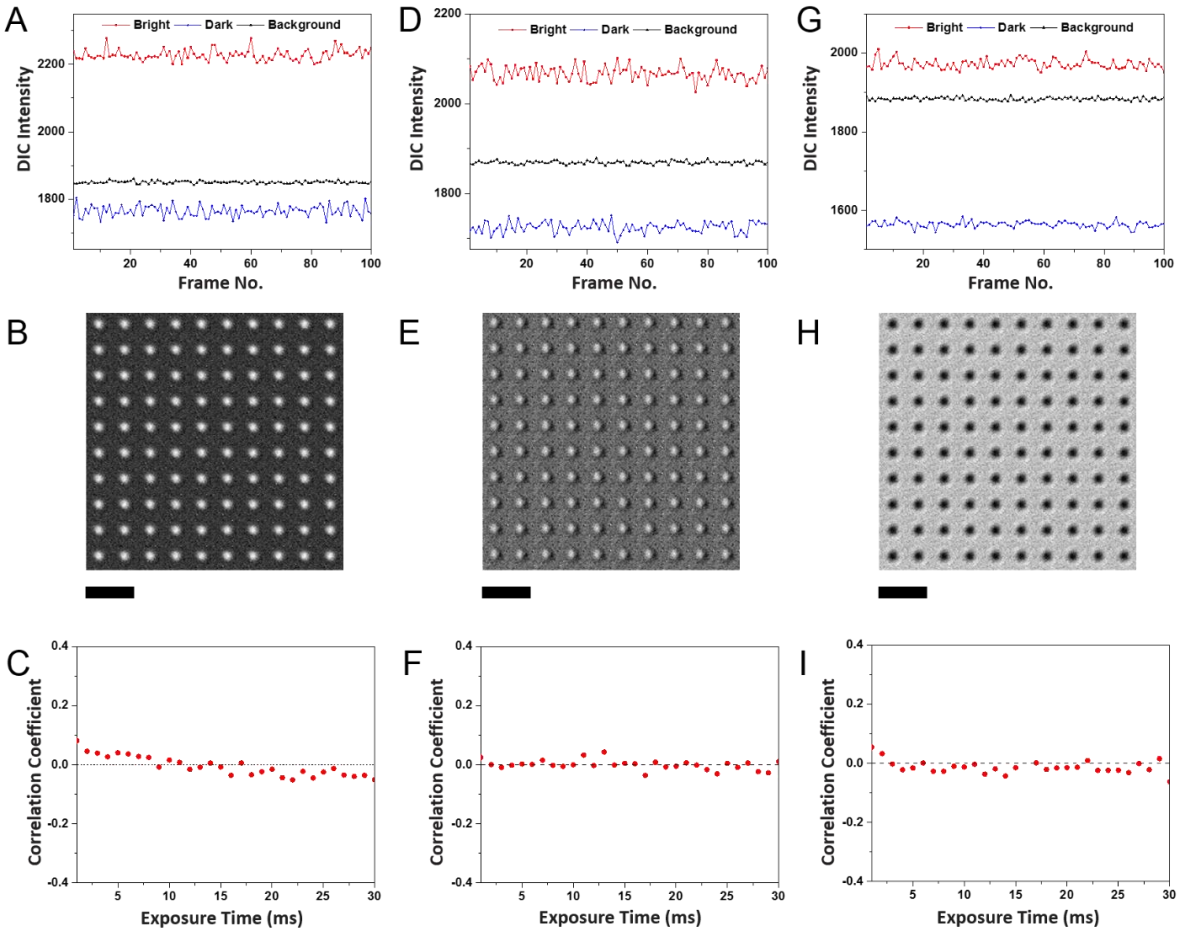

Figure 4. PEG-modified AuNRs that were not rotating on synthetic lipid bilayer. (A, D, and G) are the first 100 frames of the total 1000-frame DIC bright and dark intensity traces (**supporting information Figure S2**) of a totally white, a half white half black, a totally black when the AuNRs orientated differently on the surface. These were extracted from the substacks that were binned to 30 ms from 1 ms movies. (B, E, and H) are the corresponding stitched DIC images to (A, D, and G). The time order was from left to right and top to bottom. The scale bar is 2 μm for (B, E, and H). (C, F, and I) are the correlation coefficient changes with respect to the exposure time for (A, D, and G). Correlation coefficients were obtained from the ACF analysis of the original 1 ms 30000 frame movie, and substacks generated by binning from 2 ms to 30 ms.

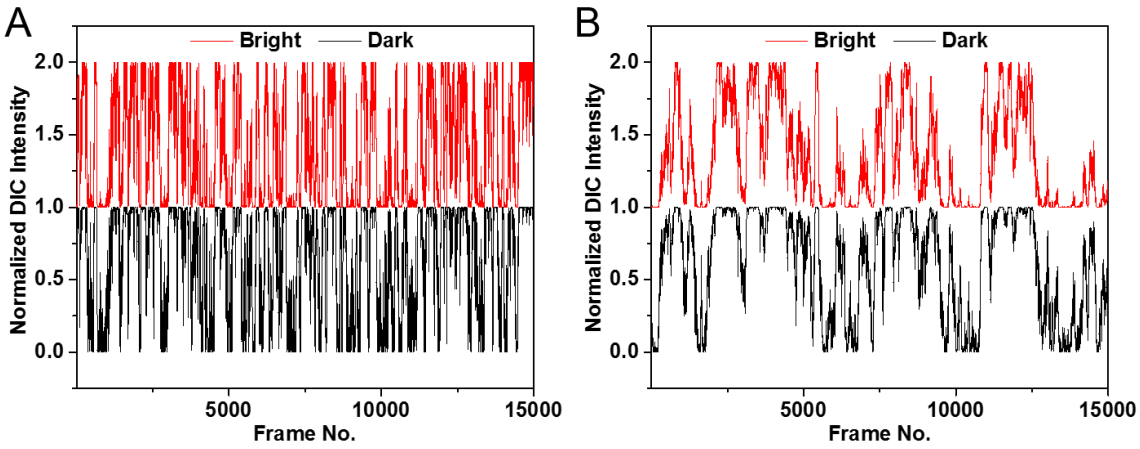

Figure 5. Simulated DIC bright and dark intensity traces of (A) fast and (B) slow in-plane rotations at 2 ms. The step size of the fast rotation was to be 2.5 times larger than that of the slow rotation.

References

(1) Jaqaman, K.; Loerke, D.; Mettlen, M.; Kuwata, H.; Grinstein, S.; Schmid, S. L.; Danuser, G. *Nat. Methods* **2008**, *5*, 695.

(2) Michaelis, J.; Brauchle, C. *Chem. Soc. Rev.* **2010**, *39*, 4731.

(3) Kulzer, F.; Xia, T.; Orrit, M. *Angew. Chem. Int. Ed.* **2010**, *49*, 854.

(4) Joo, C.; Balci, H.; Ishitsuka, Y.; Buranachai, C.; Ha, T. *Annu. Rev. Biochem.* **2008**, *77*, 51.

(5) Woll, D.; Braeken, E.; Deres, A.; De Schryver, F. C.; Uji-i, H.; Hofkens, J. *Chem. Soc. Rev.* **2009**, *38*, 313.

(6) Saxton, M. J.; Jacobson, K. *Annu. Rev. Biophys. Biomol. Struct.* **1997**, *26*, 373.

(7) Empedocles, S. A.; Neuhauser, R.; Bawendi, M. G. *Nature* **1999**, *399*, 126.

(8) Quinlan, M. E.; Forkey, J. N.; Goldman, Y. E. *Biophys. J.* **2005**, *89*, 1132.

(9) Saxton, M. J. *Nat. Methods* **2008**, *5*, 671.

(10) Verena, R.; Markus, A.; Stefan, W.; Gerhard, J. S. *Curr. Protein Pept. Sci.* **2011**, 714.

(11) Craenenbroeck, E. V.; Engelborghs, Y. *J. Mol. Recognit.* **2000**, *13*, 93.

(12) Klaus, W. *Rev. Laser Eng.* **2006**, *31*, 388.

(13) Tcherniak, A.; Dominguez-Medina, S.; Chang, W.-S.; Swanglap, P.; Slaughter, L. S.; Landes, C. F.; Link, S. *J. Phys. Chem. C* **2011**, *115*, 15938.

(14) Zhang, B.; Lan, T.; Huang, X.; Dong, C.; Ren, J. *Anal. Chem.* **2013**, *85*, 9433.

(15) Eng, J. K.; McCormack, A. L.; Yates, J. R. *J. Am. Soc. Mass Spectrom.* **1994**, *5*, 976.

(16) Lu, C. Y.; Vanden Bout, D. A. *J. Chem. Phys.* **2006**, *125*, 124701.

(17)Wei, C.-Y.; Lu, C.-Y.; Kim, Y.; Vanden Bout, D. *J. Fluoresc.* **2007**, *17*, 797.

(18) Hoang, D. T.; Paeng, K.; Park, H.; Leone, L. M.; Kaufman, L. J. *Anal. Chem.* **2014**, *86*, 9322.

(19) Gu, Y.; Sun, W.; Wang, G.; Fang, N. *J. Am. Chem. Soc.* **2011**, *133*, 5720.

(20) Gu, Y.; Sun, W.; Wang, G.; Zimmermann, M. T.; Jernigan, R. L.; Fang, N. *Small* **2013**, *9*, 785.

(21) Hinze, G.; Diezemann, G.; Th, B. *Phys. Rev. Lett.* **2004**.

(22) Qian, H.; Sheetz, M. P.; Elson, E. L. *Biophys. J.* **1991**, *60*, 910.

(23) Saxton, M. J. *Biophys. J.* **1994**, *67*, 2110.

(24) Saxton, M. J. *Biophys. J.* **1997**, *72*, 1744.

(25) Wang, G.; Stender, A. S.; Sun, W.; Fang, N. *Analyst* **2010**, *135*, 215.

(26) Sun, W.; Xiao, L.; Fang, N. In *Cell Imaging Techniques*; Taatjes, D. J., Roth, J., Eds.; *Humana Press*, **2013**, *931*, 169.

(27) Stender, A. S.; Marchuk, K.; Liu, C.; Sander, S.; Meyer, M. W.; Smith, E. A.; Neupane, B.; Wang, G.; Li, J.; Cheng, J.-X.; Huang, B.; Fang, N. *Chem. Rev.* **2013**, *113*, 2469.

(28) Sonnichsen, C.; Alivisatos, A. P. *Nano Lett.* **2005**, *5*, 301.

(29) Chang, W.-S.; Ha, J. W.; Slaughter, L. S.; Link, S. *Proc. Natl. Acad. Sci. U. S. A.* **2010**, *107*, 2781.

(30) Wang, G.; Sun, W.; Luo, Y.; Fang, N. *J. Am. Chem. Soc.* **2010**, *132*, 16417.

(31) Pierrat, S.; Hartinger, E.; Faiss, S.; Janshoff, A.; Sönnichsen, C. *J. Phys. Chem. C* **2009**, *113*, 11179.

(32) Gert, S.; Sheila, O. B.; Toos, D.; Danilo, D. L. *Adv. Drug Deliv. Rev.* **1995**, *17*, 31.

(33) Murphy, C. J.; Gole, A. M.; Stone, J. W.; Sisco, P. N.; Alkilany, A. M.; Goldsmith, E. C.; Baxter, S. C. *Acc. Chem. Res.* **2008**, *41*, 1721.

(34) Grabinski, C.; Schaeublin, N.; Wijaya, A.; D'Couto, H.; Baxamusa, S. H.; Hamad-Schifferli, K.; Hussain, S. M. *ACS Nano* **2011**, *5*, 2870.

(35) Niidome, T.; Yamagata, M.; Okamoto, Y.; Akiyama, Y.; Takahashi, H.; Kawano, T.; Katayama, Y.; Niidome, Y. *J. Control. Release* **2006**, *114*, 343.

(36) MacDonald, R. C.; MacDonald, R. I.; Menco, B. P.; Takeshita, K.; Subbarao, N. K.; Hu, L. R. *Biochim. Biophys. Acta.* **1991**, *1061*, 297.

(37) Janshoff, A.; Kunneke, S. *Eur. Biophys. J.* **2000**, *29*, 549.

(38) Chia-Yin, J. W.; Yeon Ho, K.; Richard, K. D.; Peter, J. R.; David, A. V. B. *Phys. Rev. Lett.* **2005**, *95*, 173001.

(39) Ediger, M. D.; Angell, C. A.; Sidney, R. N. *J. Phys. Chem.* **1996**, *100*, 13200.

(40) Angell, C. A.; Ngai, K. L.; McKenna, G. B.; McMillan, P. F.; Martin, S. W. *J. Appl. Phys.* **2000**, *88*, 3113.

Supporting Information

for

AUTOCORRELATION FUNCTION ANALYSIS OF ROTATIONAL DYNAMICS OF GOLD NANOROD

* Movies are available upon request.

Supporting Figures

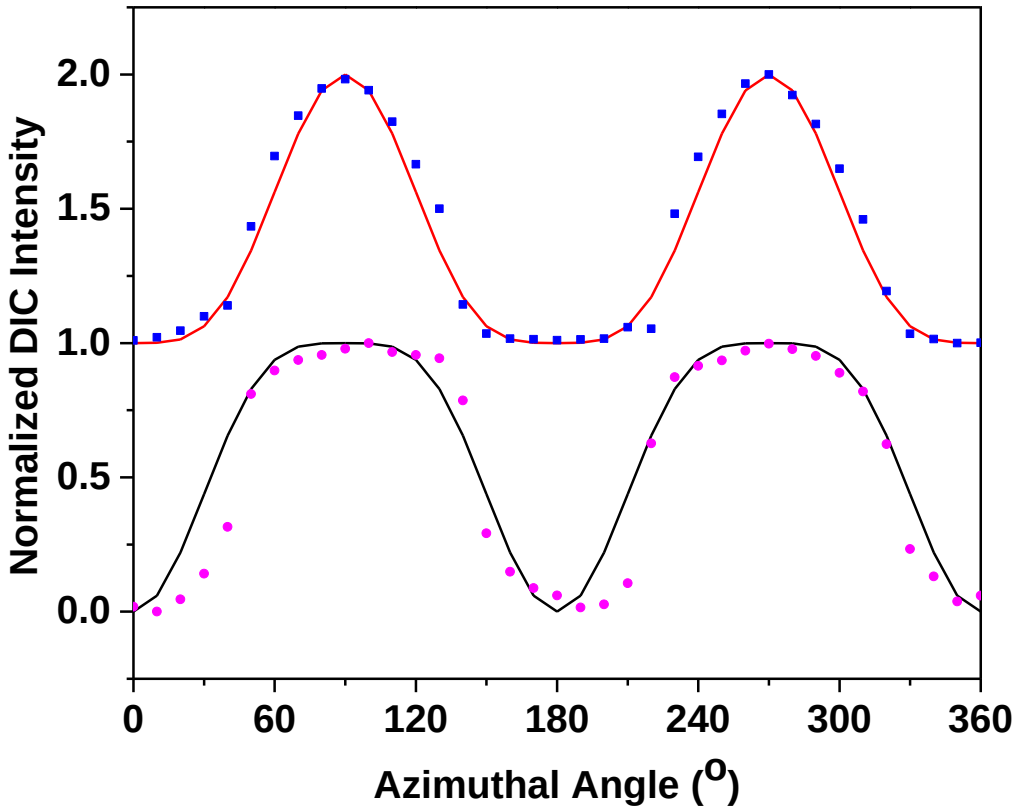

Figure S1. Periodic changes of the normalized DIC intensity of a 40 × 118 nm PEG-modified AuNRs fixed on a glass coverslip and rotated every 10 degree for 360 degree on sample stage. Red and black lines were calculated theoretical DIC bright and dark intensities over 360 degree. Solid blue squares and solid purple dots were obtained from the recorded DIC image of PEG-modified AuNRs at different orientations.

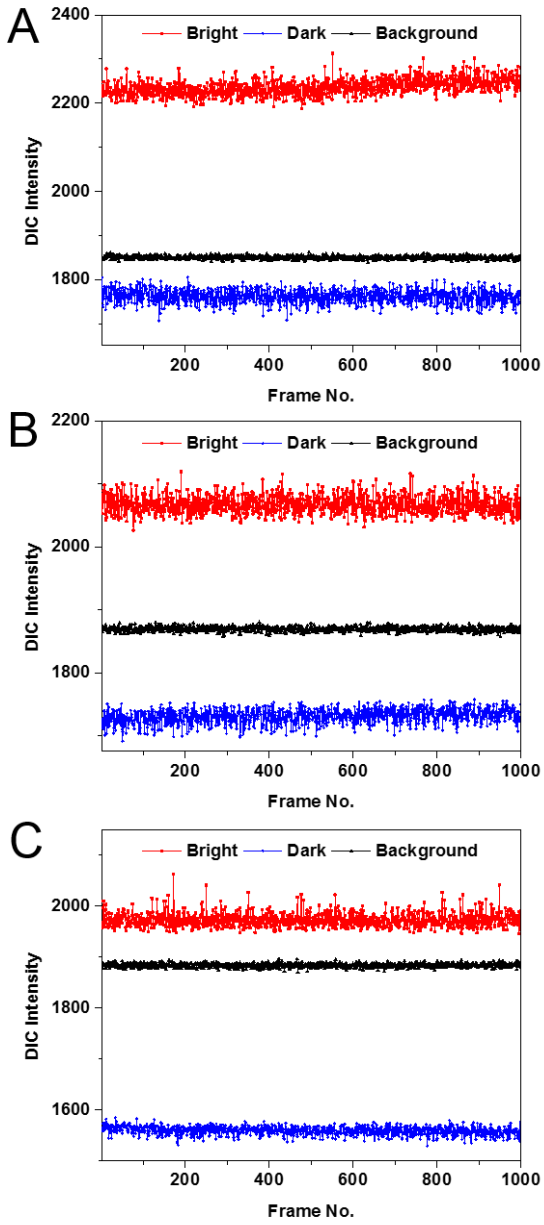

Figure S2. Complete 1000-frame DIC bright and dark intensity traces of a totally white, a half white half black, a totally black when the AuNRs orientated differently on the surface from binned 30 ms movies. The first 100 frames of (A, B, and C) were zoomed in to produce the intensity traces in Figure 4 (A, D, and G).

CHAPTER 5

OVERALL CONCLUSIONS

Single particle tracking (SPT) has been proven to be a very powerful tool in dynamic studies of chemical and biological systems. Single particle orientation and rotational tracking (SPORT) techniques are able to study the translational and rotational behaviors of the imaging probes to disclose the crucial information in many biological processes. DIC-based SPORT technique is believed to be one of the most unique SPORT techniques for SPT in dynamic systems.

The development of the DIC-based SPORT techniques relies on the innovations in imaging probes, advance in instrumentations and particle tracking algorithm, and progress in data interpretations. With the goal of making contributions to the development and extending the applications of SPORT in dynamic systems, this dissertation presents the use of multishell Au/Ag/SiO_2 core-shell hybrid nanorods with tunable optical properties as the new SPORT probes. These optically anisotropic hybrid plasmonic probes have well-defined size and shape and exhibit polarization and wavelength dependent behavior in DIC microscopy. It provides enhanced detection sensitivity with addition of the silver layer, improved stability and additional surface modification possibility. The design of Parallax-DIC microscopy and the implementation of auto-focusing algorithm in 5D-SPT method demonstrates the technical advance in DIC-based SPORT technique. It enables the simultaneous 3D spatial tracking and orientation determination in the visualization of intracellular transport of cargos in live cells. With certain modifications, this auto-focusing algorithm can be incorporated into other light microscopic techniques. Taking the advantage of the nonphotobleaching nature of

nonfluorescent probes (AuNRs in this case) and ability of autocorrelation function analysis to extract information from noisy data, considerable long DIC intensity traces are subjected to autocorrelation function analysis with certain data interpretations. Experimental parameters for rotational study in DIC-based SPORT are examined with the help of computer simulations. The goal of this study is to help with future data analysis and experiment designs in rotational dynamics research using DIC-based SPORT technique.

Most of the current studies using DIC-based SPORT techniques are technical demonstrations. Understanding the mechanisms behind the observed rotational behaviors of the imaging probes should be the focus of the future SPORT studies. More efforts are still needed in the development of new imaging probes, particle tracking methods, instrumentations, and advanced data analysis methods to further extend the potential of DIC-based SPORT technique.